Application of LADAR in the Analysis of Aggregate Characteristics

DETAILS

86 pages | 8.5 x 11 | PAPERBACK
ISBN 978-0-309-25845-6 | DOI 10.17226/22718

AUTHORS

Wang, Linbing; Sun, Wenjuan; Lally, Evan M.; Wang, Anbo; Druta, Cristian; and Tutumluer, Erol

NATIONAL COOPERATIVE HIGHWAY RESEARCH PROGRAM

NCHRP REPORT 724

Application of LADAR in the Analysis of Aggregate Characteristics

Linbing Wang
Wenjuan Sun
Evan M. Lally
Anbo Wang
VIRGINIA POLYTECHNIC INSTITUTE AND STATE UNIVERSITY
Blacksburg, VA

Cristian Druta
VIRGINIA TECH TRANSPORTATION INSTITUTE
Blacksburg, VA

Erol Tutumluer
UNIVERSITY OF ILLINOIS AT URBANA-CHAMPAIGN
Champaign, IL

Subscriber Categories
Highways • Geotechnology • Materials

Research sponsored by the American Association of State Highway and Transportation Officials
in cooperation with the Federal Highway Administration

TRANSPORTATION RESEARCH BOARD

WASHINGTON, D.C.
2012
www.TRB.org

NATIONAL COOPERATIVE HIGHWAY RESEARCH PROGRAM

Systematic, well-designed research provides the most effective approach to the solution of many problems facing highway administrators and engineers. Often, highway problems are of local interest and can best be studied by highway departments individually or in cooperation with their state universities and others. However, the accelerating growth of highway transportation develops increasingly complex problems of wide interest to highway authorities. These problems are best studied through a coordinated program of cooperative research.

In recognition of these needs, the highway administrators of the American Association of State Highway and Transportation Officials initiated in 1962 an objective national highway research program employing modern scientific techniques. This program is supported on a continuing basis by funds from participating member states of the Association and it receives the full cooperation and support of the Federal Highway Administration, United States Department of Transportation.

The Transportation Research Board of the National Academies was requested by the Association to administer the research program because of the Board's recognized objectivity and understanding of modern research practices. The Board is uniquely suited for this purpose as it maintains an extensive committee structure from which authorities on any highway transportation subject may be drawn; it possesses avenues of communications and cooperation with federal, state and local governmental agencies, universities, and industry; its relationship to the National Research Council is an insurance of objectivity; it maintains a full-time research correlation staff of specialists in highway transportation matters to bring the findings of research directly to those who are in a position to use them.

The program is developed on the basis of research needs identified by chief administrators of the highway and transportation departments and by committees of AASHTO. Each year, specific areas of research needs to be included in the program are proposed to the National Research Council and the Board by the American Association of State Highway and Transportation Officials. Research projects to fulfill these needs are defined by the Board, and qualified research agencies are selected from those that have submitted proposals. Administration and surveillance of research contracts are the responsibilities of the National Research Council and the Transportation Research Board.

The needs for highway research are many, and the National Cooperative Highway Research Program can make significant contributions to the solution of highway transportation problems of mutual concern to many responsible groups. The program, however, is intended to complement rather than to substitute for or duplicate other highway research programs.

NCHRP REPORT 724

Project 04-34
ISSN 0077-5614
ISBN 978-0-309-25845-6
Library of Congress Control Number 2012944201

COPYRIGHT INFORMATION

NOTICE

The project that is the subject of this report was a part of the National Cooperative Highway Research Program, conducted by the Transportation Research Board with the approval of the Governing Board of the National Research Council.

The members of the technical panel selected to monitor this project and to review this report were chosen for their special competencies and with regard for appropriate balance. The report was reviewed by the technical panel and accepted for publication according to procedures established and overseen by the Transportation Research Board and approved by the Governing Board of the National Research Council.

The opinions and conclusions expressed or implied in this report are those of the researchers who performed the research and are not necessarily those of the Transportation Research Board, the National Research Council, or the program sponsors.

The Transportation Research Board of the National Academies, the National Research Council, and the sponsors of the National Cooperative Highway Research Program do not endorse products or manufacturers. Trade or manufacturers' names appear herein solely because they are considered essential to the object of the report.

Published reports of the

NATIONAL COOPERATIVE HIGHWAY RESEARCH PROGRAM

are available from:

Transportation Research Board
Business Office
500 Fifth Street, NW
Washington, DC 20001

and can be ordered through the Internet at:

http://www.national-academies.org/trb/bookstore

Printed in the United States of America

THE NATIONAL ACADEMIES

Advisers to the Nation on Science, Engineering, and Medicine

The **National Academy of Sciences** is a private, nonprofit, self-perpetuating society of distinguished scholars engaged in scientific and engineering research, dedicated to the furtherance of science and technology and to their use for the general welfare. On the authority of the charter granted to it by the Congress in 1863, the Academy has a mandate that requires it to advise the federal government on scientific and technical matters. Dr. Ralph J. Cicerone is president of the National Academy of Sciences.

The **National Academy of Engineering** was established in 1964, under the charter of the National Academy of Sciences, as a parallel organization of outstanding engineers. It is autonomous in its administration and in the selection of its members, sharing with the National Academy of Sciences the responsibility for advising the federal government. The National Academy of Engineering also sponsors engineering programs aimed at meeting national needs, encourages education and research, and recognizes the superior achievements of engineers. Dr. Charles M. Vest is president of the National Academy of Engineering.

The **Institute of Medicine** was established in 1970 by the National Academy of Sciences to secure the services of eminent members of appropriate professions in the examination of policy matters pertaining to the health of the public. The Institute acts under the responsibility given to the National Academy of Sciences by its congressional charter to be an adviser to the federal government and, on its own initiative, to identify issues of medical care, research, and education. Dr. Harvey V. Fineberg is president of the Institute of Medicine.

The **National Research Council** was organized by the National Academy of Sciences in 1916 to associate the broad community of science and technology with the Academy's purposes of furthering knowledge and advising the federal government. Functioning in accordance with general policies determined by the Academy, the Council has become the principal operating agency of both the National Academy of Sciences and the National Academy of Engineering in providing services to the government, the public, and the scientific and engineering communities. The Council is administered jointly by both Academies and the Institute of Medicine. Dr. Ralph J. Cicerone and Dr. Charles M. Vest are chair and vice chair, respectively, of the National Research Council.

The **Transportation Research Board** is one of six major divisions of the National Research Council. The mission of the Transportation Research Board is to provide leadership in transportation innovation and progress through research and information exchange, conducted within a setting that is objective, interdisciplinary, and multimodal. The Board's varied activities annually engage about 7,000 engineers, scientists, and other transportation researchers and practitioners from the public and private sectors and academia, all of whom contribute their expertise in the public interest. The program is supported by state transportation departments, federal agencies including the component administrations of the U.S. Department of Transportation, and other organizations and individuals interested in the development of transportation. **www.TRB.org**

www.national-academies.org

COOPERATIVE RESEARCH PROGRAMS

AUTHOR ACKNOWLEDGMENTS

The research reported herein was performed under NCHRP Project 4-34. The authors would like to extend their sincere gratitude to the project panel, including Ervin L. Dukatz, Jr. (Chair), William G. Eager, G. P. Jayaprakash, Julie E. Kliewer, Richard C. Meininger, Alan C. Robords, and William H. Skerritt for their advice, input, and provision of aggregates for this study. We also want to extend our thanks to Cris Harris, Yang Lu, Yu Zhou, Ashley Stanford, Yinning Zhang, and Yue Hou for their efforts. The authors would also like to acknowledge the generous help and strong support from Richard C. Meininger for coordinating the use of the AIMS II at FHWA, and the supplying of aggregates for the project by Alan C. Robords. Sincere thanks are also extended to Yuanjie Xiao for scanning some of the aggregate particles using the UIAIA system, and to Ed Harrigan and Alan Robords for their assistance in collecting relevant information on the aggregates analyzed in this project. Finally, the authors would like to express their appreciation of the panel's invaluable detailed review comments and suggestions for the draft report.

FOREWORD

By Edward T. Harrigan
Staff Officer
Transportation Research Board

This report describes a LADAR-based system for measurement of aggregate characteristics over a wide range of particle size. Thus, the report will be of immediate interest to materials engineers in state departments of transportation and industry.

NCHRP Project 4-34, "Application of LADAR in the Analysis of Aggregate Characteristics," was conducted by Virginia Polytechnic Institute and State University, Blacksburg, Virginia, with participation by the University of Illinois at Urbana-Champaign.

The objective of the project was to develop and evaluate a laser detection and ranging (LADAR) system capable of precise and accurate measurement of the aggregate characteristics of shape, volume, angularity, surface texture, specific surface area, and volumetric gradation. Ideally, the final system would be applicable to aggregate in three size categories—coarse (2 in. to #4), fine (#4 to #200), and microfine (P200)—and suitable for routine use in research, central, and field laboratories for Portland cement concrete and asphalt concrete mixture design and quality assurance.

The project, which developed new equipment and computer algorithms, proved technically challenging. The project team developed a prototype Fourier transform interferometry (FTI) system with fully functional hardware and software. The system can characterize aggregate shape, angularity, texture, surface area, and volume of a wide range of aggregate sizes with high accuracy. Assembly and operation of the FTI system consisting of a charge-coupled device (CCD) camera, a fringe source, a sample platform, and a software package are fully documented in the report.

The accuracy and precision of the prototype FTI system are comparable to or better than those of other systems now available to automatically measure aggregate characteristics, but its current range of aggregate size—¾ in. to #50—is narrower than desired. Extending this size range is possible in the future by using a CCD camera with a larger field of view and increasing the system resolution through appropriate selection of the equipment components.

The report fully documents the research to develop and validate the prototype FTI system and includes three appendixes:

- Appendix B: The FTI System Components
- Appendix C: Initial Efforts for the Particle Mounting System
- Appendix D: Test Protocol in AASHTO Format

In addition, seven appendixes are available for download from the NCHRP Project 4-34 web page at http://apps.trb.org/cmsfeed/TRBNetProjectDisplay.asp?ProjectID=867:

- Appendix A: Literature Review
- Appendix E: Photographs of Coarse Aggregates in Set 1
- Appendix F: FTI Analysis Results
- Appendix G: Histogram and Normal Quantile Plot of Aggregates in Set 1
- Appendix H: Manual Measurements of Aggregates in Set 1
- Appendix I: AIMS II Analysis Results
- Appendix J: UIAIA Analysis Results

CONTENTS

Note: Many of the photographs, figures, and tables in this report have been converted from color to grayscale for printing. The electronic version of the report (posted on the Web at www.trb.org) retains the color versions.

CHAPTER 1

Introduction

1.1 Project Background

Aggregates are an important component in asphalt concrete, cement concrete, granular base, and treated base. Their characteristics, including shape, angularity, surface texture, and surface area, significantly affect the properties of mixtures. Historically, tremendous efforts have been made to quantify these characteristics both directly and indirectly and correlate them to performance at both a state level and national level. Some national efforts in the past few years focused on evaluation of the direct measurement methods using two-dimensional (2-D) image analysis. There are some limitations for the 2-D and semi-3-D methods (i.e., the 2.5-D). The intent of NCHRP Project 4-34 was to develop and evaluate a 3-D aggregate characterization system and analysis method using laser detection and ranging (LADAR) for aggregate shape, angularity, texture, and surface area. Compared to X-ray computerized tomography (XCT), the aggregate imaging system developed in this project costs less and can be made portable for field testing more conveniently.

Morphological characteristics of both coarse and fine aggregates have a significant influence on the performance of paving materials and pavements. Shape, angularity, and texture influence aggregate mutual interactions and strengths of bonds between aggregates and asphalt binders, cement paste, and lime (Al-Rousan et al., 2006). The interactions and bond strengths are vital to the rheological properties related to workability and friction resistance of mixtures. Therefore, characterization of aggregate morphological characteristics is important for better quality control of aggregates and performance of pavements.

There are two fundamental ways to measure the shape, angularity, and texture of aggregates: direct methods and indirect methods. Direct methods are conducted by measuring aggregates with either visual inspection or digital image analysis, or by measuring the three dimensions of aggregates using calipers (AASHTO T 304, AASHTO TP 56, and ASTM D3398). A concern with current direct methods is that some are time consuming and laborious (Rao et al., 2000; Fletcher et al., 2003). On the other hand, indirect methods may measure the shear strength of specimens composed of graded aggregates or the air void contents of uncompacted specimens (ASTM D4791, ASTM D5821). This is usually based on the assumption that uncompacted void content and shear strength are related to the shape, angularity, and texture of aggregates. The indirect methods usually cannot separate the contributions to strength by shape, angularity, texture, and gradation, which affect the strength and deformation via different mechanisms. The indirect methods, however, can directly measure the angularity and texture of aggregates (Al-Rousan et al., 2006).

Motivated by the advancements in digital imaging and availability of low-cost and fast image processing software, various image techniques have recently been developed to provide a cost-effective means for rapid quantification of aggregate morphological characteristics. Some image techniques analyze aggregates by using 2-D shape analysis, which is not accurate enough to represent 3-D morphological characteristics of aggregates. Besides, the current imaging techniques use different image acquisition methods and different definitions of shape, angularity, and texture. The results are sometimes not directly comparable.

This research has developed an aggregate imaging system named the Fourier Transform Interferometry (FTI) system that acquires 3-D surface coordinates and analyzes the morphological characteristics using Fourier transform through a user-friendly matrix laboratory (MATLAB) program developed for this project. This chapter presents the description of the various chapters and appendices in a logically integrated flow. These chapters and appendices present the fundamentals of FTI, the components and integration of the FTI system, the morphological characterization methodology that the FTI system has adopted, the FTI analysis results of both coarse and fine aggregates, a statistical analysis of the results, an assessment of the accuracy of the FTI results by comparison to

manual measurements, and a comparison of the FTI results with those of peer systems including the Aggregate Imaging Measurement System (AIMS) II and University of Illinois Aggregate Image Analyzer (UIAIA). Chapter 7 presents conclusions and recommendations for future research.

1.2 Objectives and Scope

The objective of NCHRP Project 4-34 was to develop and evaluate a prototype FTI system capable of precise and accurate measurement of aggregate characteristics, including shape, volume, angularity, surface texture, specific surface area, and volumetric gradation. The FTI system needed to be applicable to aggregate in each of three size categories: coarse (2 in. to #4), fine (#4 to #200), and microfine (P200), and be suitable for routine use in research, central, and field laboratories for Portland cement concrete (PCC) and hot-mix asphalt (HMA) mixture design, and quality control and acceptance (QC/QA). To develop a system that is capable of imaging such a wide range of particle sizes without using different hardware settings is a paramount challenge. A promising technique is FTI, which can achieve very high resolution with a large view field. Nevertheless, to image particles passing #200 is not a realistic operation. Based on the overall objective of the project, the FTI system provides 3-D images with the highest possible resolution for a wide range of particle sizes (please note that size range and resolution are two conflicting requirements) and quantifies the aggregate morphological characteristics based on the 3-D high-resolution images. The system needs to be able to collect images of a particle from multiple views and then reconstruct a 3-D surface of the object for the characterization of shape, angularity, surface texture, surface area, and volume of the particle. Therefore, the research work focused on the following aspects:

(1) Development of an imaging system to generate 3-D coordinates of the aggregate surfaces.
(2) Development of a computational program for analyzing 3-D coordinates and abstracting morphological characteristics that are consistent with qualitative evaluation with the unaided human eye.
(2) Morphological characterization results that are consistent with manual measurement, and characterization results that are consistent with other available aggregate imaging techniques.

1.3 Report Outline

Figure 1-1 presents the flowchart of the final report. There are seven chapters and ten appendices. Chapter 1 presents the project background, supported with a comprehensive literature review on imaging techniques for aggregate morphological characterization presented in Appendix A (available, with Appendices E through J, at http://apps.trb.org/cmsfeed/TRBNetProjectDisplay.asp?ProjectID=867). The scope and objectives of the project are also outlined in Chapter 1.

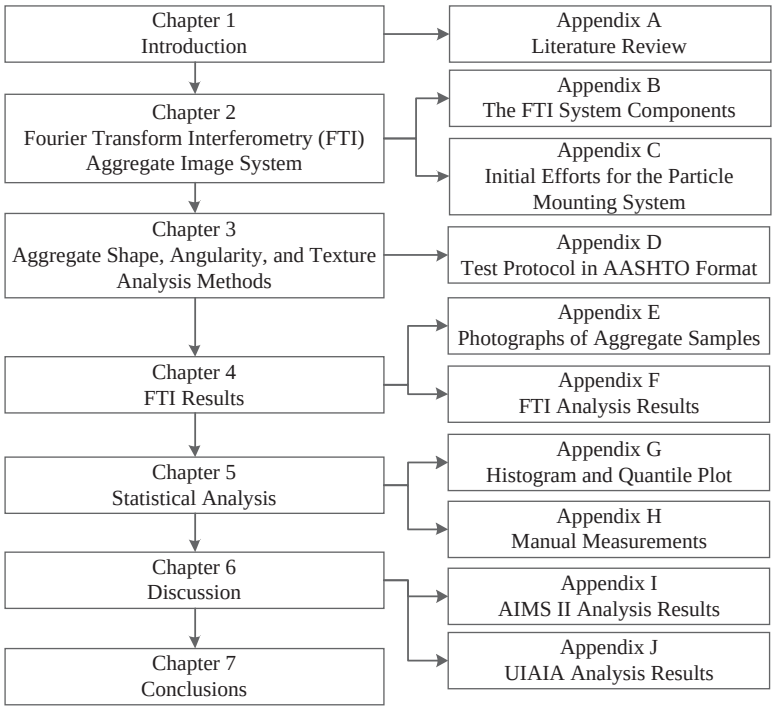

Figure 1-1. Flowchart of the final report.

Chapter 2 introduces the final version of the FTI system, which consists of a charged-coupled device (CCD) camera, a fringe source, an angled mirror, an adjustable-height particle tray, and a MATLAB software package. Some of the various intermediate versions of the systems (or components) are presented in the appendices. The efforts for these intermediate versions were significant and could not be avoided due to the innovative nature of the project. The MATLAB software package is composed of three modules: (1) a main program to process images into 3-D coordinates, (2) an error correction program to remove errors from the data file generated by the main program, and (3) a morphology analysis program to analyze the corrected data for computing shape, angularity, and texture. The specifics of the components of the FTI system are listed in Appendix B. The initial efforts for developing the particle mounting system are presented and discussed in Appendix C.

Chapter 3 presents the analysis method developed for the morphology analysis program. The program uses the 2-D Fourier transform method to analyze the 3-D coordinates and computes morphological characteristics such as angularity and texture. The program can also calculate shape factors such as sphericity, the flatness ratio, and the elongation ratio. A draft test protocol in AASHTO format is presented in Appendix D.

Chapter 4 presents the morphological characterization results by the FTI method for both coarse and fine aggregates, with raw data presented in Appendix F. Images of the coarse aggregate samples in Set 1 are presented in Appendix E. The manual measurements of the coarse aggregate dimensions for Set 1 are presented in Appendix H.

Chapter 5 presents the statistical analysis of FTI results of coarse aggregates. Both analysis of variance (ANOVA) and *t*-tests were performed to compare the mean values of the FTI results and the corresponding parameters of manual measurements and those of the AIMS II and UIAIA systems. The histograms and quantile plots are presented in Appendix G.

Chapter 6 compares the FTI results to those of manual measurement and the AIMS II and UIAIA systems. The polishing and crushing effects due to Micro-Deval testing on the changes of morphological characteristics of aggregates are also discussed in this chapter. The results of AIMS II and UIAIA for aggregates in Set 1 are presented in Appendix I and Appendix J, respectively.

Chapter 7 presents general conclusions, possibilities for future research, and a list of potential applications. Implementation plans and cost assessments are presented at the end of this chapter.

CHAPTER 2

Fourier Transform Interferometry Aggregate Image System

This chapter presents the design configuration of the FTI aggregate imaging and analysis system. The FTI system is actually a noncontact 3-D surface profilometer, using a simple fiber optic coupler to form a Young's double-pinhole interferometer. A fiber optic switch is adopted to control the input of laser signals from two sources with wavelengths of 675 nm and 805 nm, respectively. The Young's fringes are projected onto a 45°-angled mirror for fringe projection on the aggregate surface. The image of the aggregate surface in the mirror is captured by a CCD camera and analyzed using the Fourier transform method, which uses the phases of the fringe pattern on the aggregate surface to reconstruct the surface profile. Figure 2-1 presents a picture of the FTI aggregate imaging system as built.

2.1 System Layout and Geometry

Figure 2-2 shows the basic FTI system geometry. The measured system geometry is summarized in Table 2-1. Figure 2-3 plots the layout of the fringe generator of the FTI system. The fringe generator consists of a pair of fiber couplers. The couplers are pigtailed to the laser source through a fiber cable, which allows the laser to be located remotely. Light from the laser source is evenly split between the two output arms of the fiber coupler. These arms are aligned close together, forming the pinholes in a Young's interferometer. Fringes are projected from the generator to the object and then viewed with the CCD camera. The locations of the fringes are governed by Eq. 2-1.

$$I(x,y) = 2I_0\left[1+\cos\left(\frac{2a}{D}kx_p - \Delta\phi\right)\right] \qquad \text{Eq. 2-1}$$

where $I(x, y)$ is the projected interferogram intensity at location (x, y), I_0 is the Gaussian beam spot pattern, $2a$ is the separation between the fibers (or pinholes), D is the distance from the pinholes to the aggregate, $k = 2\pi/\lambda$, λ is the wavelength, x_p is a spatial coordinate parallel to a line joining the pinhole centers, and $\Delta\phi$ accounts for any phase difference at the end faces of the two fibers. The fringe pattern depends on the distance to the aggregate surface and is a function of the aggregate surface profile (coordinates).

The pair of laser sources is coupled to optical fibers and routed through a 2×1 fiber optic switch. With an included USB interface, the switch allows users to easily control the laser wavelength from the main imaging computer. The output from the switch is routed through an optical fiber to the fringe projection source, which sits in a sealed enclosure. All optical fibers are designed for single-mode operation above 600 nm.

There are three main components within the main enclosure: the fringe source, the CCD camera and lens system, and the adjustable-height particle tray and mirror (shown in Figure 2-4). During aggregate imaging operation, an aggregate is (or several aggregates are) placed on the tray, and the enclosure door is closed to block all stray light from entering the system. The application of the enclosure is to improve fringe visibility by eliminating ambient light that otherwise could make the dark areas of the image slightly brighter. The CCD camera is positioned perpendicular to the adjustable-height particle tray on the optical axis. The fringes are projected at an angle β relative to the imaging axis.

2.2 Image Collection System

Figure 2-5 shows the assembly of the CCD camera, bellows, and lens. The electrostatically cooled CCD camera is a Starlight Xpress SXVF-H9 monochrome camera with 16-bit resolution. Its own noise floor limits the actual resolution of the CCD camera. Besides the CCD camera, a macro lens is adopted to help provide the best possible horizontal resolution (x-, y-axis) over the range of desired particle sizes. It is a Schneider Makro-Symmar 5.6/80 lens with a focal length of 80 mm.

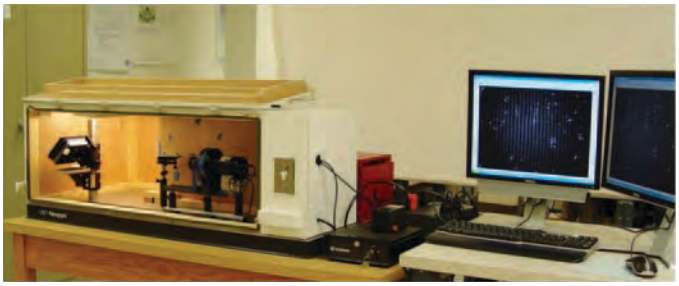

Figure 2-1. FTI aggregate image system.

The aggregate is placed on an adjustable-height tray (shown in Figure 2-6), and users can move the surface into the field of view to maximize the clarity of images. The maximum adjustable height of the tray is 25 mm. The tray is covered with a black matte surface so that high contrast can be achieved between the particle surface and the tray background. Three images are captured to generate the 3-D coordinates for the surface of an aggregate particle (one image taken with visible light and two images captured with lasers of wavelengths of 675 nm and 808 nm).

2.3 FTI Aggregate Image Analysis Program

Figure 2-7 shows the graphical user interface (GUI) of the FTI software developed for the aggregate imaging system and analysis. Figure 2-8 shows the flowchart of the FTI aggregate image program. There are three main subroutines: the main program, the error correction program, and the morphological analysis program.

2.3.1 Main Program

The main program was developed for surface identification and reconstruction from the images acquired by the FTI system. It calculates the unwrapped phase with the FTI algorithm by identifying and tracking a reference fringe on each surface (Figure 2-10); after that, each surface profile is calculated by shifting the phase.

Table 2-1. FTI system geometry.

Parameter	Variable	Measured Value
Pinhole-to-Object Distance	d_P	264.7 mm
Projection Angle	β	16.39 deg.
Pinhole Separation	$2a$	289 μm
Fringe Frequency	f_0	1.552 mm^{-1}
Primary Wavelength	λ_1	675 nm
Reference Wavelength	λ_2	805 nm

After inputting the three images taken using the FTI system, the surface boundary shown in Figure 2-9 is mapped at the beginning of the program to improve efficiency by working only within boundaries in later operations. Prior to boundary mapping, a background adjustment can be made to perform top-hat filtering to achieve better contrast between the background and the aggregate surfaces. Then boundary maps can be generated from the visual images, which are taken under the fluorescent light inside the system enclosure without any fringe present.

With the surface boundaries identified, a reference fringe (Figure 2-10) can be entered to calculate the surface coordinates by tracking fringes. Before the operation of the interferogram data, a pre-filtering step is implemented to improve the quality of the data prior to the FTI filtering. A band-pass digital finite impulse response (FIR) filter is applied in the horizontal direction, and a low-pass FIR filter smoothens the data vertically. After that, a desired reference fringe is manually chosen for each surface. The reference fringe extends to the upper and lower bounds of the particle so that the entire surface can be mapped. The FTI processing algorithm and subsequent fringe referencing steps are performed

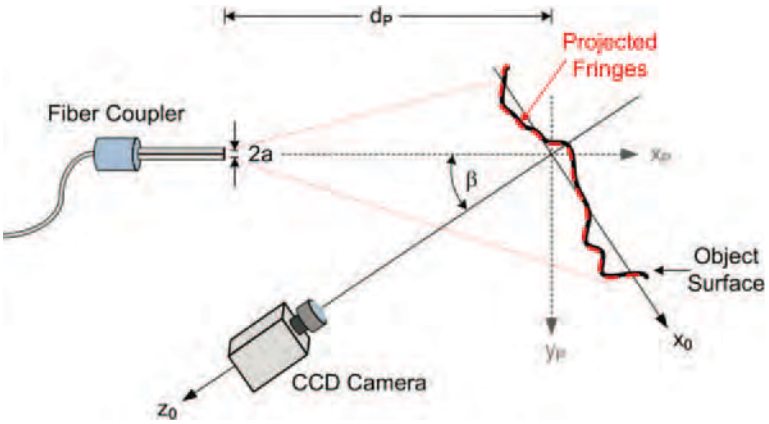

Figure 2-2. Basic FTI system geometry (Lally, 2010).

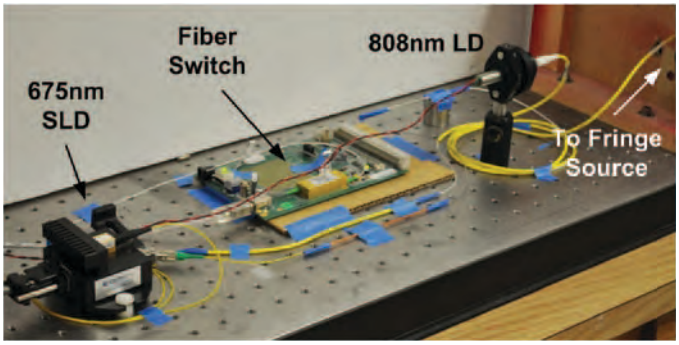

Figure 2-3. Fringe source: fiber-coupled laser sources and 1 × 2 fiber switch.

row by row, and only rows that contain a reference point can be reconstructed.

The fringe-tracking algorithm locates the exact fringe peak in each row of the surface fringe projection by starting at a reference row and then looping up through the image and analyzing each row sequentially. For each subsequent row in the loop, the rounded value of the peak from the last row is served as a new center point, fitting a quadratic function that is forced to fit the fringe data around the peaks with windowed curves, as shown in Figure 2-10. Once the tracking algorithm reaches the upper extent of the bounded surface, it starts over from a new row and tracks down to the lower extent of the bounded surface. These tracking steps are performed for both laser images within the same loop.

The fringe peak shift is only dependent on the projection angle, β, which is governed by Eq. 2-2. Therefore, the entire surface pattern shifts horizontally when the mean surface height changes. Two interferograms are projected at different wavelengths, and each will experience an identical shift.

$$\Delta_z x_0^{(M)} = -\Delta z \tan\beta \qquad \text{Eq. 2-2}$$

Figure 2-4. Angled mirror and adjustable-height particle tray (left), and the CCD camera, bellows, and lens system (right) (Lally, 2010).

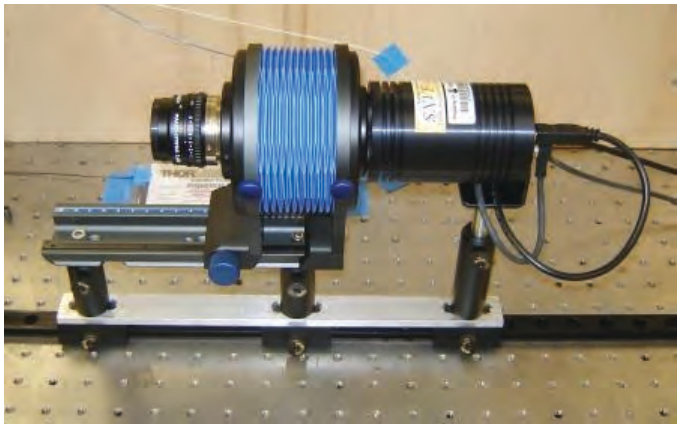

Figure 2-5. CCD camera, bellows, and lens assembly.

where $\Delta_z x_0^{(M)}$ is the shift value for the M^{th} order fringe and Δz is the aggregate surface height.

After the selected reference fringe is tracked, the fringe order lookup table is automatically generated to determine the unique fringe order. First, a set of roughly 12 fringes is selected based on the average x_0 value, and then the specific fringe is identified by matching the measured value of peak location difference shown in the lookup table, which is represented in Figure 2-11. Fringe tracking and averaging is a highly effective means of noise reduction.

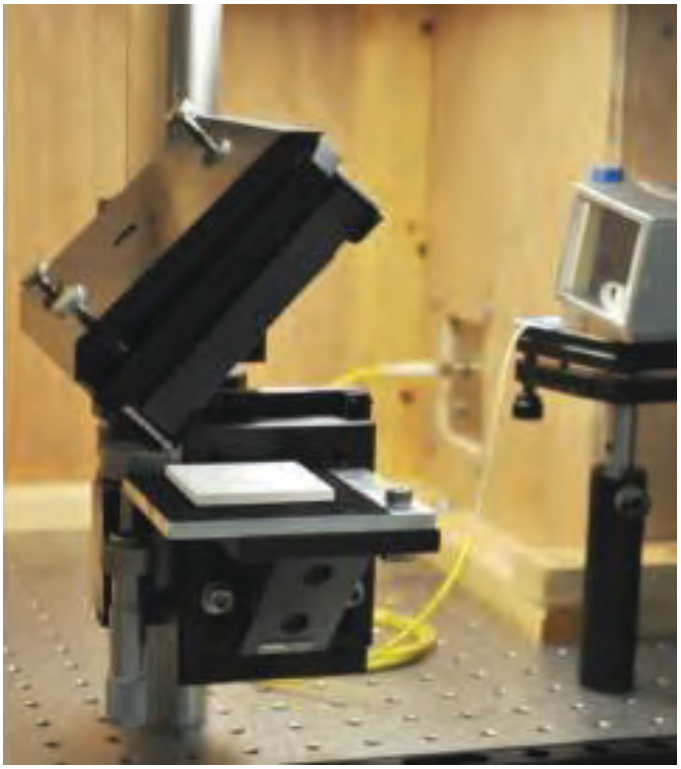

Figure 2-6. Adjustable-height particle tray.

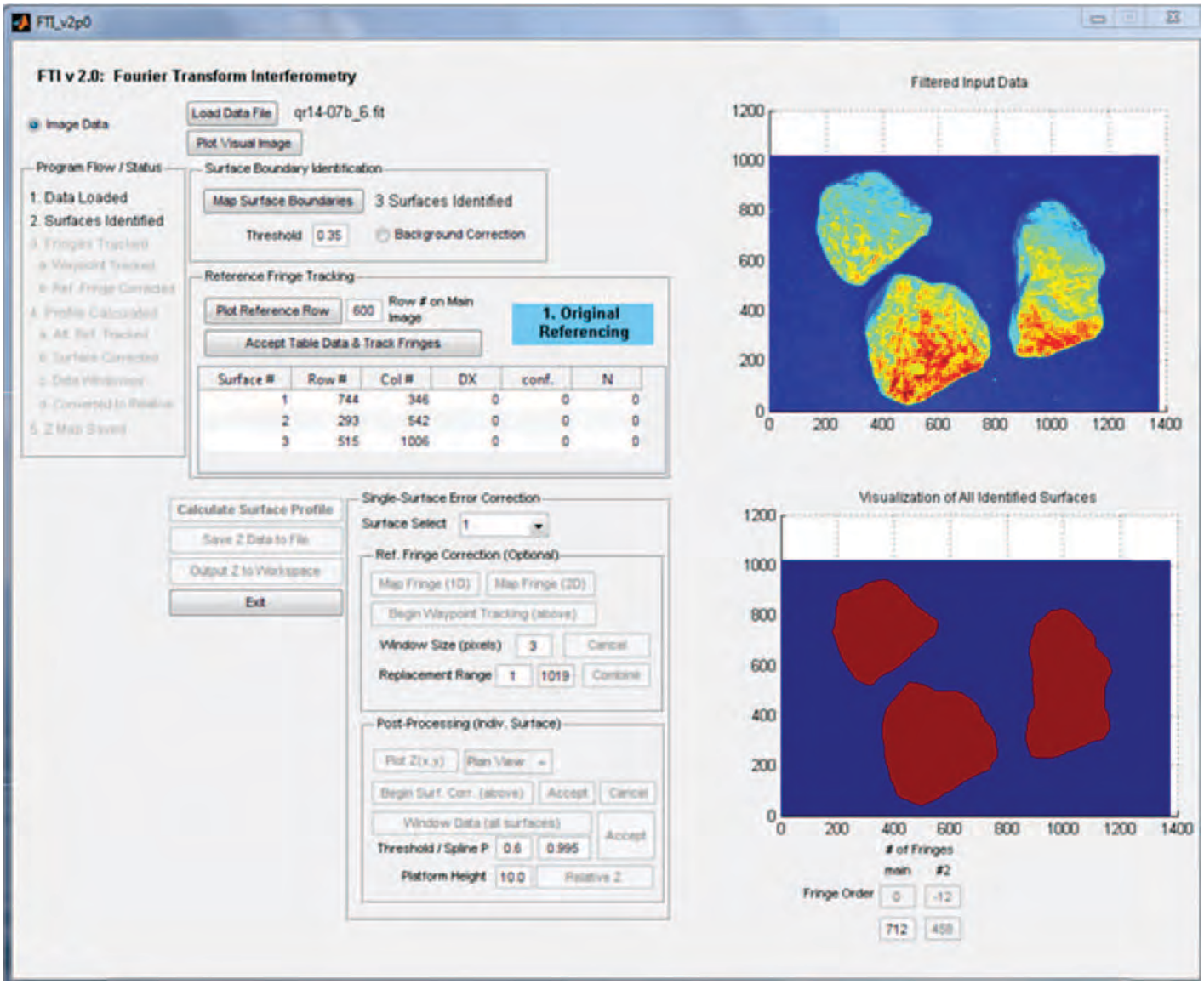

Figure 2-7. GUI of the FTI software.

Once the reference fringe order is determined, it must be applied to the unwrapped phase map $\varphi_u(x, y)$, calculated only once for the entire image, regardless of surface boundary or reference fringe selection. All subsequent operations can be thought of as independent modifications of the master phase map to prepare it for surface reconstruction over different areas of the image.

2.3.2 Error Correction Program

After running the main program, the procedure will continue by running an error correction module. In the error correction program, surface errors are identified by users, and a secondary reference fringe is selected to reprocess the $z(x, y)$ matrix to modify and improve the reconstructed surface map. Since many errors can be caused by steep edges along the surface boundary, a windowing algorithm that automatically locates these erroneous data regions and removes bad data from the $z(x, y)$ matrix was developed. By manually entering the variable height of the particle tray measured with a built-in micrometer, the surface height map can be converted to measure the particle thickness above its resting plane (i.e., the tray that the aggregate rests on).

If row errors are present, they are clearly identifiable during visual inspection of the reconstructed surface profile. A secondary reference fringe is selected near the center of the bad data region. Based on the mechanism for error propagation, it can be assumed that the source of the errors is located near the interface between smooth and erroneous

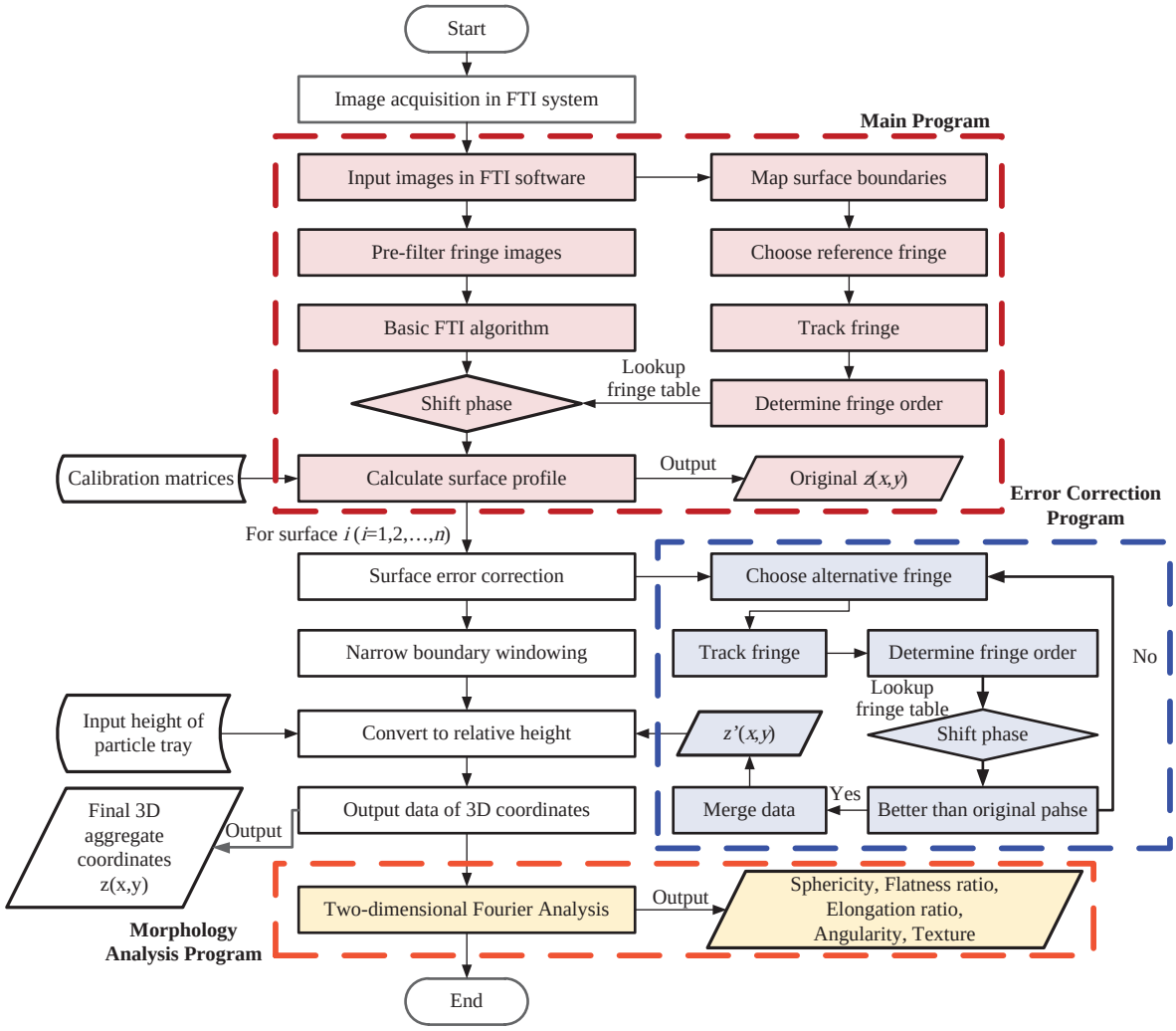

Figure 2-8. Flowchart of the FTI aggregate image analysis program.

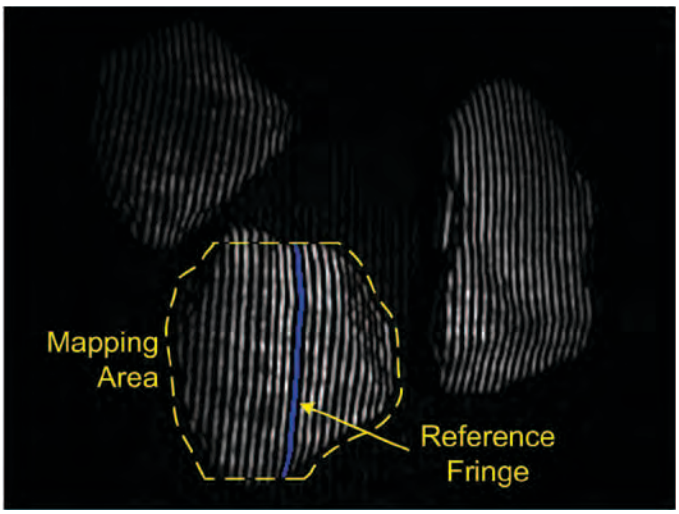

Figure 2-9. Surface reconstruction from the reference fringe.

data. The secondary reference is tracked and its order identified using the lookup table representation shown in Figure 2-11. When this occurs, the original unwrapped phase map is shifted to match the secondary reference fringe, resulting in two data sets (i.e., the data set by use of the main reference fringe and data set by use of the secondary reference fringe). To correct the errors, the method of multiple references is adopted to perform automatic decision making to combine two data sets processed with different reference fringes.

Figure 2-12 shows the map of surface errors used in the narrow windowing algorithm. The windowing algorithm works directly with the reconstructed surface map, identifies error areas, and constructs a narrow boundary to exclude the erroneous data. To achieve this goal, original Cartesian coordinates are converted to polar coordinates, and a piecewise cubic polynomial curve fitting is applied akin to inflating a balloon inside the good area of the surface data.

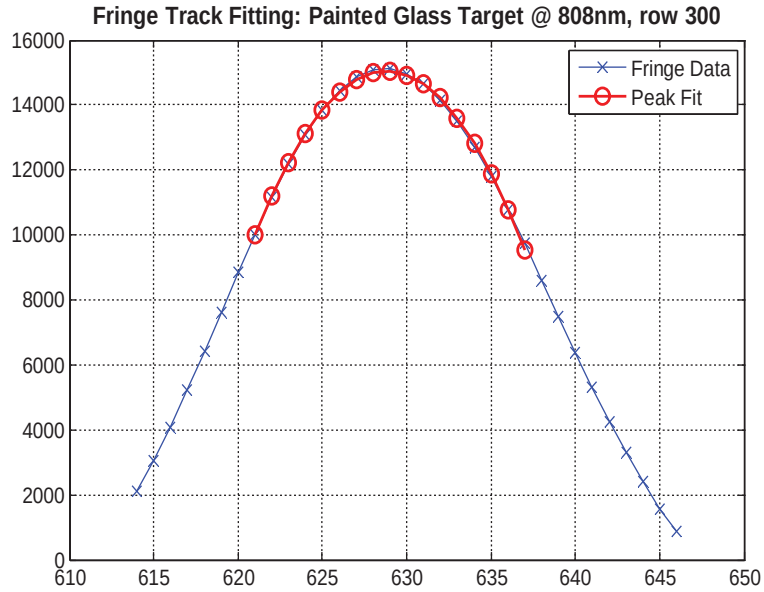

Figure 2-10. Narrow window curve fitting during fringe peak tracking (Lally, 2010).

2.3.3 Output Data Format

Figure 2-13 plots the geometry configuration of the output data format. The output $z(x, y)$ matrix from the FTI software is a matrix giving surface height z for every (x, y) coordinate as a three-dimensional surface map that has been bounded, corrected, and windowed. The mapped boundary data of the imaged particle are also included in the output to give the exact dimensions of the particle in the horizontal plane. These data could be interpreted as the vertical distance between a point on the aggregate top surface and the particle tray at the bottom.

2.4 Accuracy and Resolution

2.4.1 Calibration

To reconstruct aggregate surfaces pixel by pixel, the system must undergo a one-time calibration to generate the quadratic fit matrices, and a 2-in.-square optical flat plate painted white was adopted as the calibration plate. In the calibration process, the optical flat plate sprayed with white paint was imaged at 19 points throughout the 25-mm mapping height range that the adjustable-height particle tray could be adjusted within. The particle tray height can be adjusted using the Vernier

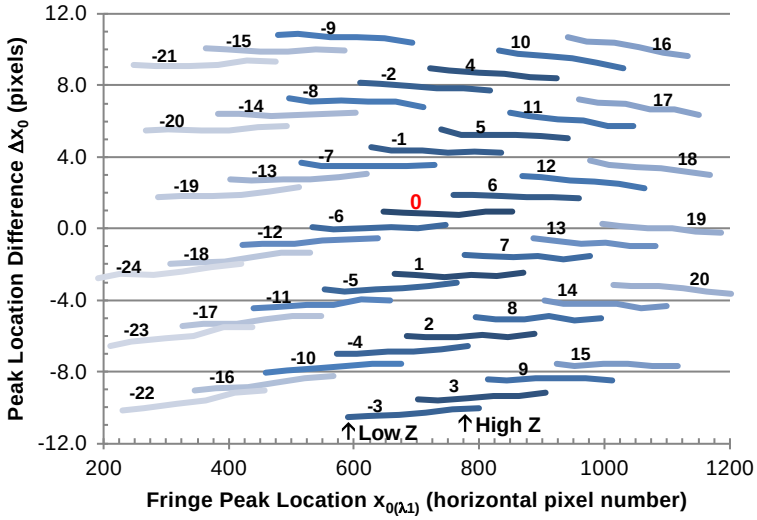

Figure 2-11. Graphical representation of the lookup table for fringe order identification (Lally, 2010).

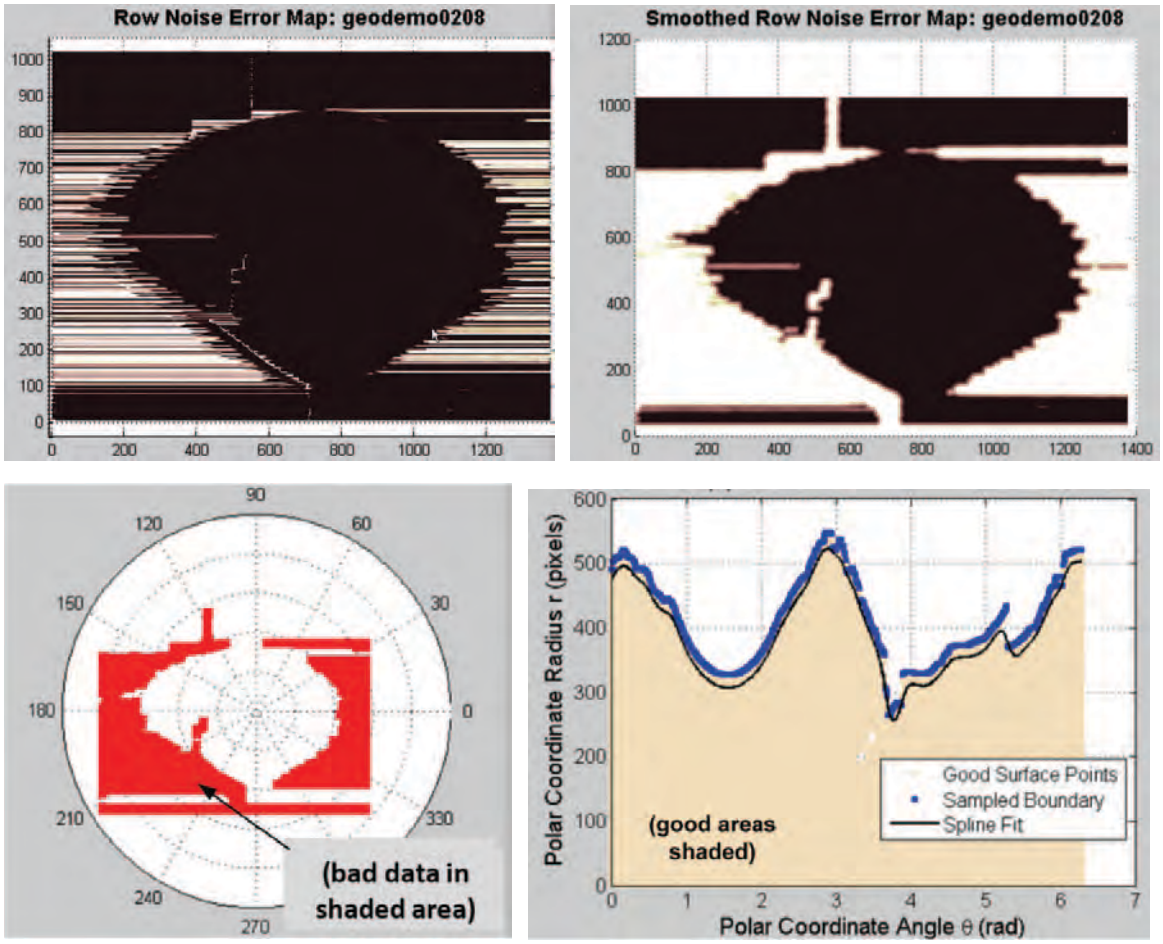

Figure 2-12. Surface error map used for windowing (Lally, 2010).

micrometer underneath the adjustable-height particle tray to take fringe images on the calibration plate. Then the phase of each interferogram was calculated using the FTI process. After compilation of 19 phase maps at varying z-values, a pixel-by-pixel quadratic fit was performed to calculate $z(x, y)$. The z-value was assumed to be constant in each image; the $z(x, y)$ matrices were reconstructed based on the images. The direct measurement of $z(x, y)$ was calculated at each pixel; the quadratic fit in the calibration process automatically accounts for misalignment and aberration errors in the system.

The calibration step is time consuming, but it only needs to be performed once. Figure 2-14 plots the fringe patterns in the calibration process, and Figure 2-15 illustrates the pixel-by-pixel quadratic calibration process.

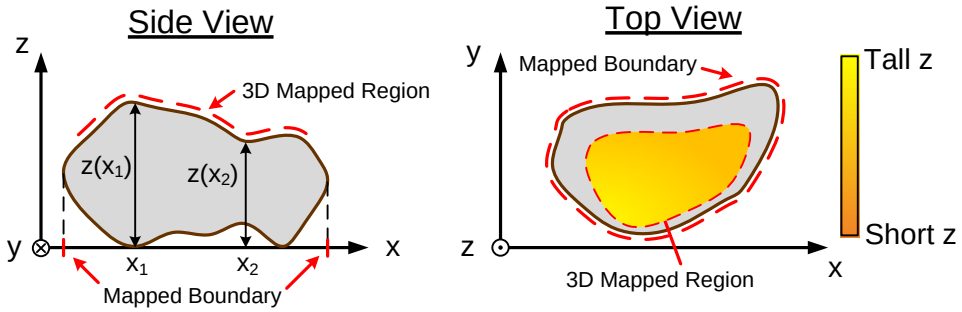

Figure 2-13. Three-dimensional output data format of z(x, y) (Lally, 2010).

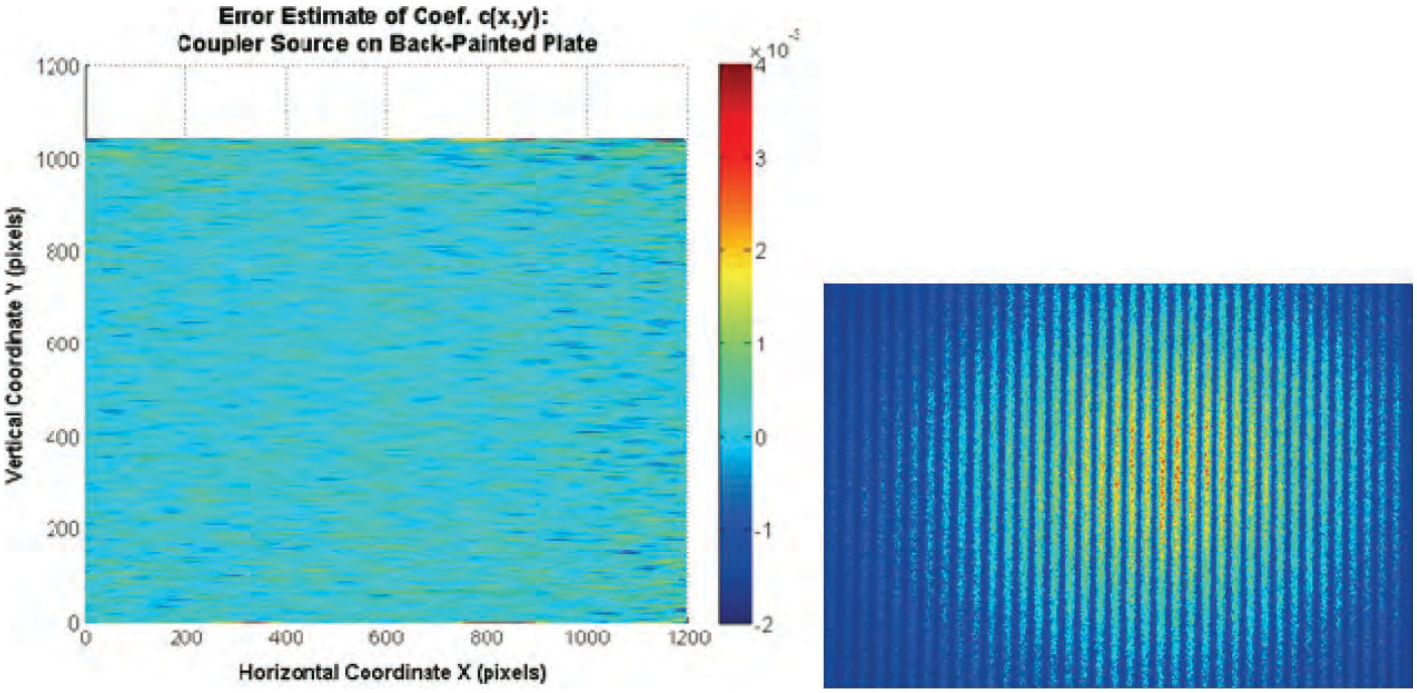

Figure 2-14. Quality of fringes generated with fiber coupler: calibration coefficient deviation (left); fringe pattern (right).

2.4.2 Flat Target Accuracy and Resolution

The nominal resolution of the FTI system is 35.4 μm per pixel in both *x*-axis and *y*-axis directions, and the measured *z*-axis resolution is 22 μm per pixel. The true horizontal resolution of the system is primarily limited by the FTI filtering operations. The accuracy and resolution of the FTI system are determined during calibration. It is important to note that the accuracy and resolution measurements are not simply a repetition of the calibration process. During resolution and accuracy testing, six of the calibration fringe images were recalled and processed using the full FTI algorithm with the application of the fitted calibrated data. The reconstructed surface profiles were checked for variations above the mean and deviations from the true nominal surface value to yield accuracy and resolution information. Resolution was quoted as twice the 2-D standard deviation, and accuracy was the 2-D root-mean-square (RMS) deviation from the true surface height.

Figure 2-16 shows that the maximum single-point surface error varies from 45 μm to 75 μm with the surface height, and the resolution varies from 19 μm to 22 μm. Results in this figure show that the best resolution and accuracy are achieved when the adjustable particle tray is positioned between Z = 10 mm and Z = 15 mm. The best height is illustrated in Figure 2-17. RMS error is better than 15 μm across the entire range, with a minimum value of 10 μm in the center. Table 2-2 shows the resolution of the FTI system.

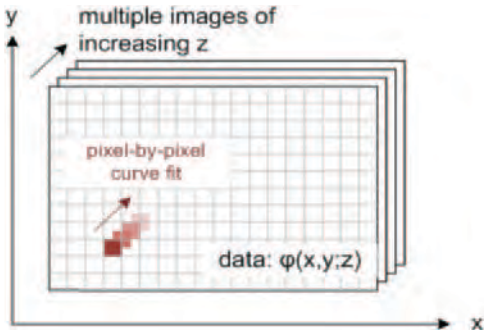

Figure 2-15. Pixel-by-pixel quadratic fit calibration process.

2.5 Safety Concern

The major safety risk incurred by the users of the system is the risk of eye damage associated with the laser source. The risk of ocular damage can be managed by limiting the power of the HeNe laser source for the interferometer. Any collimated beam at a power level less than 1 mW is safe to work around without eye protection, although eye damage can occur if the user stares directly into the beam for several seconds. The risks associated from power levels of less than 10 mW can be safely managed by wearing a basic pair of attenuating glasses designed for the

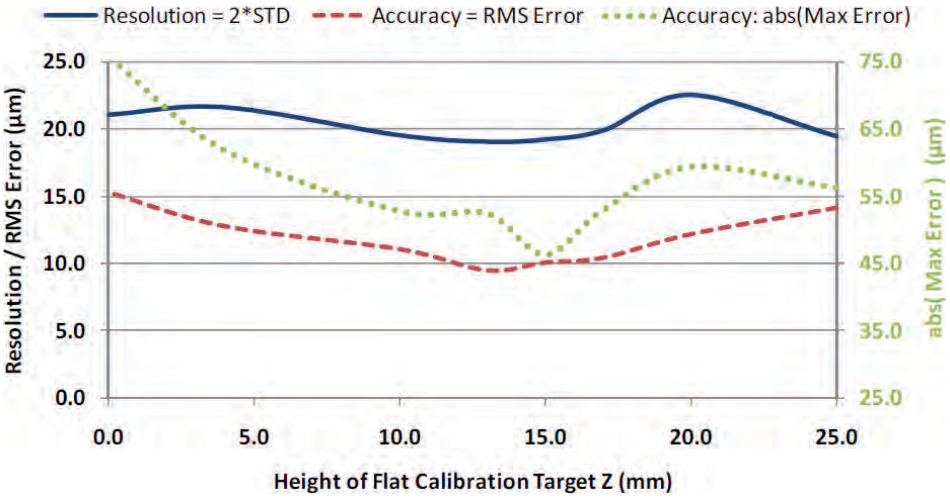

Note: STD = standard deviation, abs = absolute value

Figure 2-16. z-axis resolution and accuracy calculation (Lally, 2010).

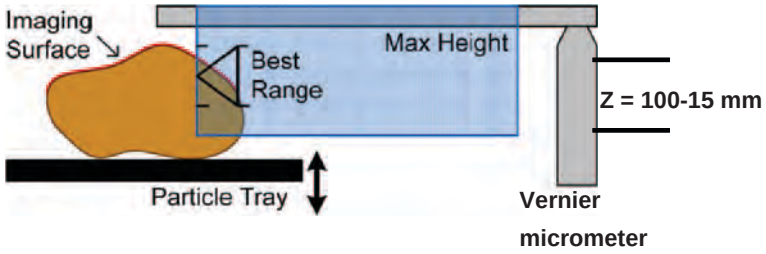

Figure 2-17. Illustration of best height range of the adjustable-height particle tray.

Table 2-2. Resolution of the FTI system.

	Over Entire Range	Over Z = 10–15mm
Surface Height Resolution	±25 µm	±20 µm
Surface Height Accuracy (RMS Error)	±15 µm	±10 µm

HeNe laser wavelength of 633 nm. Such glasses are relatively inexpensive and widely available.

The proposed CCD camera, the Starlight Xpress SXVF-H9, was originally designed for astronomical imaging, and therefore it can be operated at relatively low power levels. For this reason, the system can effectively operate at an input power level of between 1 mW and 5 mW. Due to the varied, inhomogeneous structures of the particles being imaged, any calculation of the reflected power is at best a rough estimate. For this reason, the input power level must be experimentally confirmed before a particular laser is selected. We are confident that, regardless of the object under test, the proposed design will be able to operate effectively at a safe power level appropriate for a user with basic eye protection.

CHAPTER 3

Aggregate Shape, Angularity, and Texture Analysis Methods

3.1 Shape

In the paving industry, shape is usually described by sphericity, flatness ratio, and elongation ratio. The FTI system implemented the characterization of these terms following Eq. 3-1 to Eq. 3-4. Sphericity is defined by Eq. 3-1. It describes the overall 3-D shape of a particle. Sphericity has a relative scale of 0 to 1. A sphericity value of 1 indicates that a particle has equal dimensions (cubical or spherical).

$$S = \sqrt[3]{\frac{D_s D_m}{D_l^2}} \qquad \text{Eq. 3-1}$$

Where D_s is the shortest dimension of a particle, D_m is the intermediate dimension of a particle, and D_l is the longest dimension of a particle.

The flatness ratio is defined by Eq. 3-2, and the elongation ratio is defined by Eq. 3-3. The FTI direct output of shape characteristics includes all three parameters. The flatness and elongation (FE) ratio can be conveniently calculated from the flatness ratio and the elongation ratio by Eq. 3-4. Aggregates are considered flat or elongated if their flatness ratio or elongation ratio is greater than 3:1.

$$\text{Flatness Ratio} = D_s / D_m \qquad \text{Eq. 3-2}$$

$$\text{Elongation Ratio} = D_m / D_l \qquad \text{Eq. 3-3}$$

$$\text{FE Ratio} = 1/(\text{Flatness Ratio} \times \text{Elongation Ratio}) = D_l / D_s \qquad \text{Eq. 3-4}$$

3.2 Angularity and Texture

The discrete Fourier transform (DFT) is applied for the 3-D surface as a discrete function $z(x, y)$ that is nonzero over the finite region $0 \le x \le N-1$ and $0 \le y \le N-1$ in the space domain. The two-dimensional N-by-N DFT and inverse N-by-N DFT relationships are given by Eq. 3-5 and Eq. 3-6 (Wang, 2007; MathWorks, 2010).

$$Z(p,q) = \sum_{x=0}^{N-1}\sum_{y=0}^{N-1} z(x,y) e^{-j\left(\frac{2\pi}{N}xp + \frac{2\pi}{N}yq\right)} \qquad \text{Eq. 3-5}$$

$$z(x,y) = \sum_{p=0}^{N-1}\sum_{q=0}^{N-1} Z(p,q) e^{j\left(\frac{2\pi}{N}xp + \frac{2\pi}{N}yq\right)} \qquad \text{Eq. 3-6}$$

$$f_x = \frac{2\pi}{N}x \qquad \text{Eq. 3-7}$$

$$f_y = \frac{2\pi}{N}y \qquad \text{Eq. 3-8}$$

Where $Z(p, q)$ is the DFT coefficient matrix in the frequency domain, $z(x, y)$ is the z coordinates of an aggregate surface, j is the imaginary root, and f_x and f_y are frequencies in x and y directions, respectively.

This approach is similar to the 1-D Fourier analysis method developed by Wang et al. (2005). High frequency and small magnitude represent texture; low frequency and large magnitude represent the gentle slopes and flat planes (of a surface) related to shape; intermediate frequency is related to angularity (Smith, 1999; Wang, 2007). Therefore, a critical step is to determine threshold frequencies that separate shape, angularity, and texture from each other.

A matrix of a predetermined size is selected as a roughness matrix to represent a sample of the surface within the boundary of the particle. Fast Fourier transform is performed on the matrix in order to determine the roughness factors. Obviously, when the matrix is large, the data may include information for texture, angularity, and shape; when the matrix is adequately small, the data may reflect the texture only. Figure 3-1 shows the schematic configuration of the roughness matrix. Roughness matrices are selected as square matrices sampled from the aggregate surface with various matrix sizes.

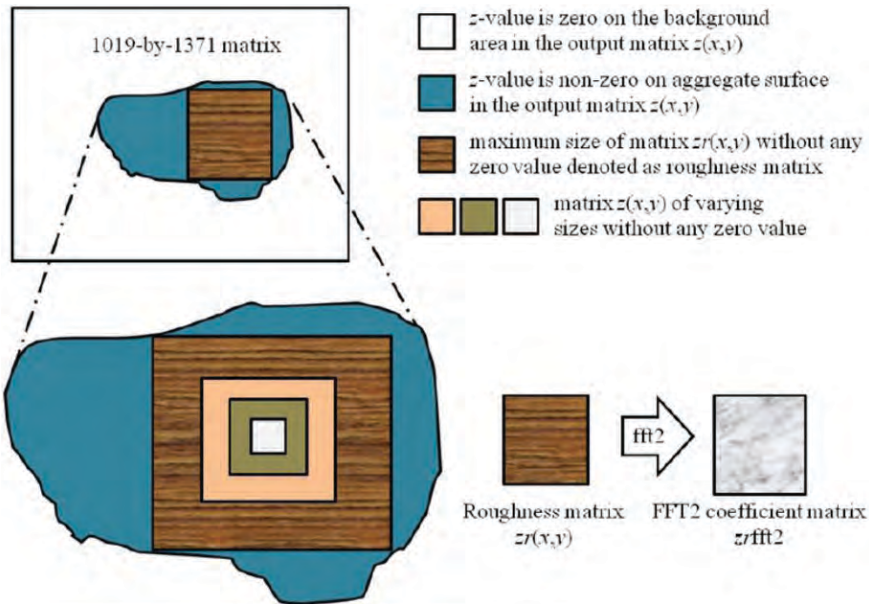

Figure 3-1. Schematic configuration of roughness matrix.

Angularity factor (AF) and texture factor (TF) are defined by Eq. 3-9 in MATLAB.

$$\text{Angularity Factor (AF)} = \sum_{p=1}^{N_A}\sum_{q=1}^{N_A}\left[\left(a(p,q)/a_0\right)^2 + \left(b(p,q)/a_0\right)^2\right] \quad \text{Eq. 3-9}$$

$$\text{Texture Factor (TF)} = \sum_{p=1}^{N}\sum_{q=1}^{N}\left[\left(a(p,q)/a_0\right)^2 + \left(b(p,q)/a_0\right)^2\right] - \text{AF}$$

where a_0 is the average height of $z(x, y)$, a and b are the real and imaginary parts of the coefficients for the 2-D fast Fourier transform (FFT2), N is the size of the $z(x, y)$ matrix, and N_A is defined as a threshold frequency, with which a 3-D surface reconstructed using the inverse of FFT2 coefficients that have their frequencies smaller than $2\pi N_A/N$ in either the x direction or y direction should represent the angularity. The FFT2 coefficients are considered to only contribute to angularity if the mean value of distance between the original surface and the reconstructed surface using the inverse of FFT2 is greater than 0.2 mm, which is the spatial spacing discernible by the unaided human eye (Brandon et al., 1999). The other Fourier coefficients are considered to contribute to texture only.

As given in Eq. 3-9, the size of $z(x, y)$ matrix N has a great influence on both AF and TF values. That is, values of both AF and TF would increase with the increase of $z(x, y)$ matrix size N since the total number of pixels (sampled points) on the x-y plane increases by the order of N^2. Consequently, it is necessary to determine the maximum values of N to quantify angularity and texture for aggregates of different sizes. In this project, the area of the roughness matrix ranges from 1.0 mm^2 to a maximum of 25% of an aggregate surface, based on the sieve size of the aggregate being analyzed. For instance, to evaluate the angularity and texture of aggregates passing a 1-in. sieve and retaining on a ¾-in. sieve, the maximum roughness matrix area is 90.7 mm^2, which is 25% of the area of a hole on a ¾-in. sieve. The center of the roughness matrix is chosen as the center of the aggregate surface. That is, the roughness matrices of varying sizes keep the same center point. This is to evaluate how the roughness changes as the roughness matrix area increases.

Figure 3-2 shows how to separate texture from angularity on an aggregate surface by applying the FFT2 method to the roughness matrix. In the first column, an original 3-D surface of a roughness matrix (301 × 301 pixel by pixel) is presented (with all the sampled points). Reconstructed surfaces are achieved by conducting an inverse Fourier transform to the Fourier coefficients with different frequencies, shown in the second column. In the third column, the differences Δz between the original surface and the reconstructed surface using different critical frequencies are plotted. The reconstructed surface increasingly approaches the actual angular and textured original surface, and the difference dramatically decreases since there are more high-frequency components included in the reconstructed surface. When using frequency f_3 to separate angularity from texture for this original surface shown in the first column, the average value of the absolute

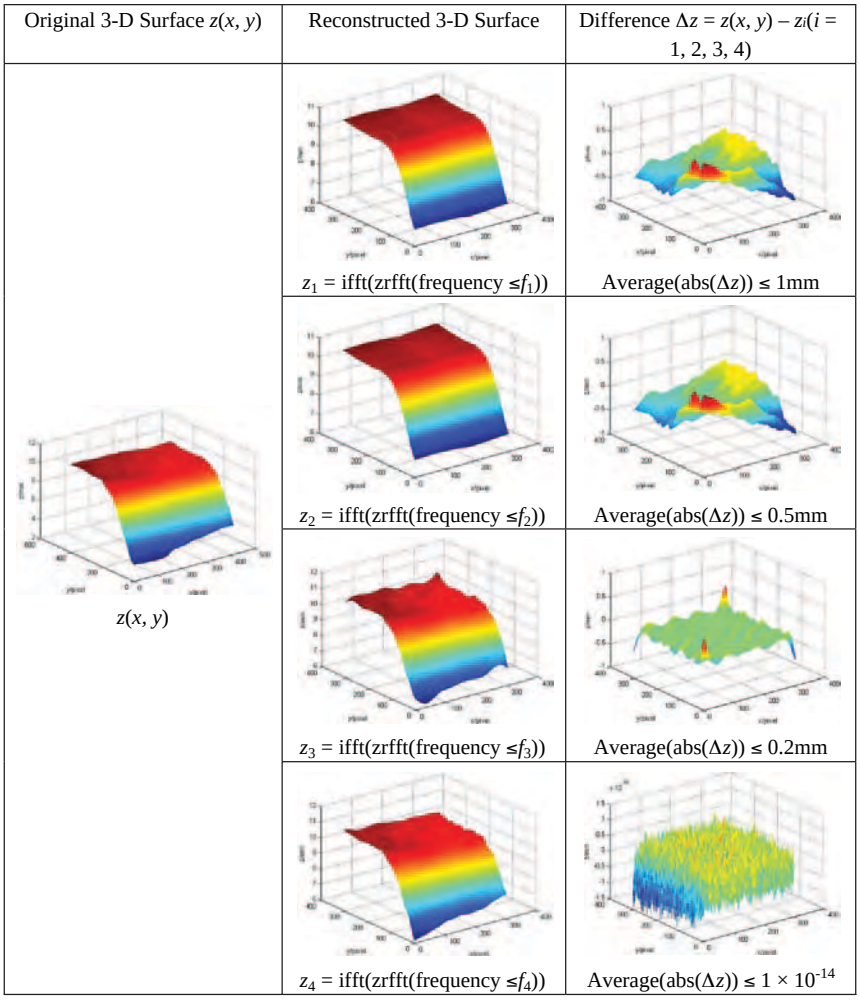

Note: 301 × 301 pixel by pixel in *x*-*y* plane, mm in *z*-axis.

Figure 3-2. Illustration of the separation between angularity and texture in roughness matrix.

difference between the original surface and the reconstructed surface is less than 0.2 mm; therefore, frequency f_3 is the critical frequency for this original surface shown in the first column.

The relationship between the AF and the corresponding area of the roughness matrix is plotted in Figure 3-3 for some aggregate particles retaining on ½-in. sieve sizes for seven types of aggregates. By plotting the relationship between AF (or TF) and roughness matrix area (hereinafter referred to as AF plot or TF plot), one will notice that the AF and TF values follow a linear relationship in both AF and TF plots. Furthermore, aggregates with more angular surfaces tend to have steeper slopes in the AF plot, and aggregates with rougher surfaces tend to have steeper slopes in the TF or AF plots. Therefore, it is reasonable to define the linear relationship (slope) in the AF and TF plots as the angularity and texture of an aggregate, respectively.

3.3 Surface Area, Volume, and Dimensions

As a result of method development, a separate program has been developed to calculate the surface areas, volumes, and dimensions. Due to the complicated nature of stitching the sections of the surfaces, these methods have not been adopted for the final version. This program has the following functionalities: data input and output, aggregate surface area and volume calculation, aggregate surface visualization, aggregate dimension analysis, and calculation of the shape factor, angularity, and texture. Figure 3-4 presents a flowchart of the FTI program.

3.3.1 Surface Area and Volume Calculation

A serial program was developed to analyze and visualize aggregate particles on a MATLAB platform. First, original

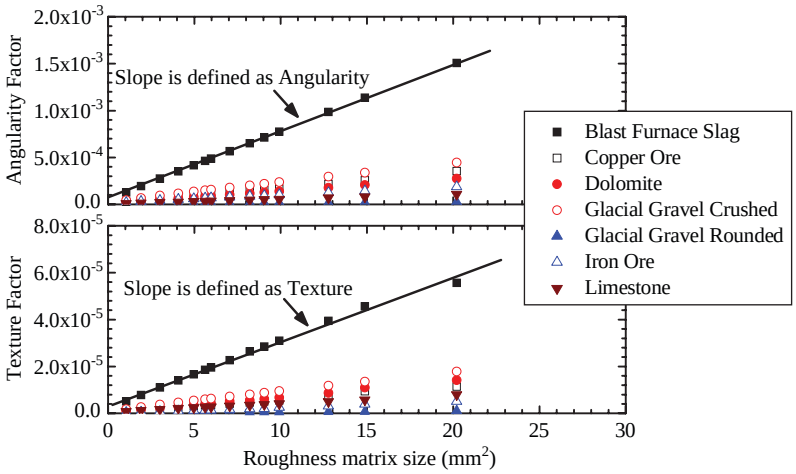

Figure 3-3. Illustration of angularity and texture in the FTI system.

data of aggregate surface point coordinates are read to the computer's memory. The data format is as follows:

```
99  101  9999
–0.1571  0.2500  5.0000
–0.3140  0.5000  5.0000
–0.4705  0.7500  5.0000
–0.6267  1.0000  5.0000
–0.7822  1.2500  5.0000
. . . .  . . . .  . . . .
```

The first row is the number of pixels in the x direction and y direction and the total number of pixels in the x-y plane. The second row until the end records the x coordinate, y coordinate, and z coordinate of each point on the aggregate surface.

We can calculate the aggregate surface area and volume from the original data (Figure 3-5). The data must be divided into two groups. One is for the upside surface. The other is for the downside surface. We can pair points (x, y, z coordinates) into triangle meshes. Every triangle surface area can be calculated as in Eq. 3-10, and so the total surface area is as calculated as in Eq. 3-11.

$$S_i = \frac{1}{2}\begin{vmatrix} x_{i1} & y_{i1} & 1 \\ x_{i2} & y_{i2} & 1 \\ x_{i3} & y_{i3} & 1 \end{vmatrix} \qquad \text{Eq. 3-10}$$

$$S = \sum_{i=1}^{n} S_i \qquad \text{Eq. 3-11}$$

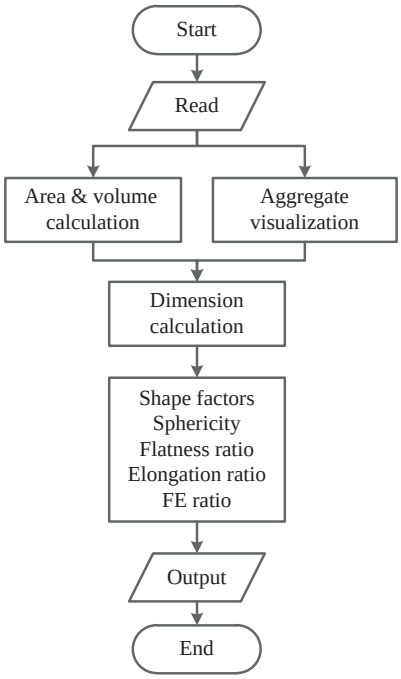

Figure 3-4. Flowchart of the FTI program.

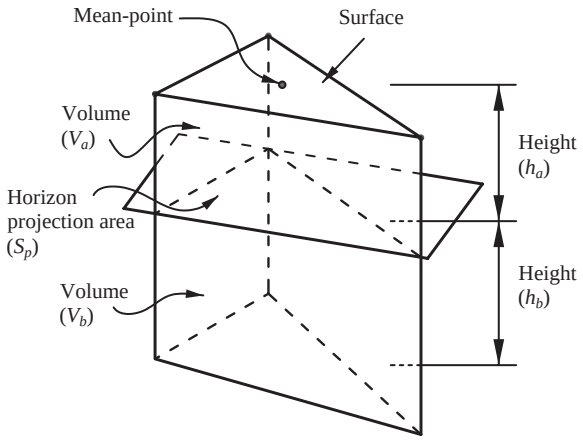

Figure 3-5. Illustration of the surface area and volume calculation.

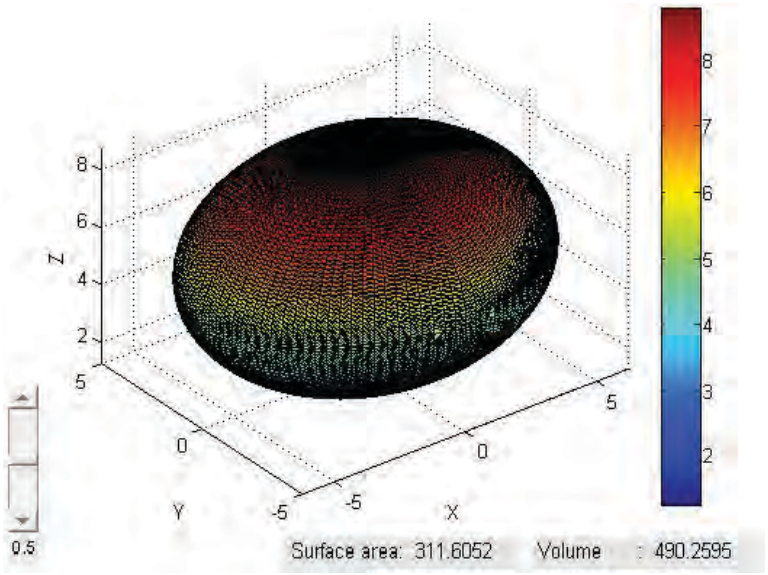

Figure 3-6. Mesh surface.

where S_i is the area of the ith triangle, S is total surface area, n is the number of triangles, and (x_{i1}, y_{i1}), (x_{i2}, y_{i2}), and (x_{i3}, y_{i3}) are coordinates of the three points on the ith triangle.

The total volume (V_i) is the sum of volume (V_a) between the top surface and the horizontal projection surface and volume (V_b) between the bottom surface and the horizontal projection surface for each element, as illustrated in Figure 3-5. The calculation methods of V, V_a, and V_b are shown by Eq. 3-12, Eq. 3-13, and Eq. 3-14.

$$V_i = V_a + V_b \qquad \text{Eq. 3-12}$$

$$V_a = S_p \times h_a V_b = S_p \times h_b \qquad \text{Eq. 3-13}$$

$$V_{a,b} = \sum_{i=1}^{n} V_i \qquad \text{Eq. 3-14}$$

3.3.2 Aggregate Visualization

Once the aggregate surface points are available, we have three options for aggregate visualization: mesh, color, and light surface, as illustrated in Figure 3-6, Figure 3-7, and Figure 3-8. The visualization helps us make qualitative assessments.

3.3.3 Aggregate Dimension Analysis

One of the important aggregate characteristics is three dimensions, shown in Figure 3-9. The three dimensions are

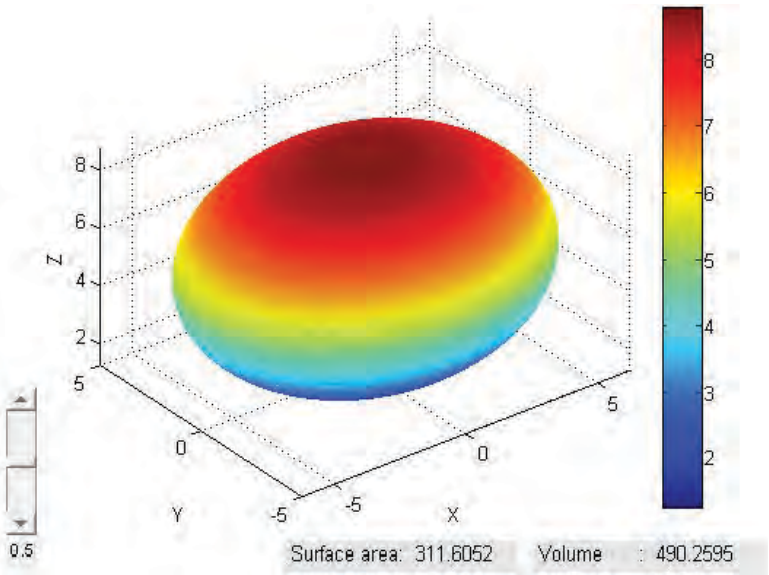

Figure 3-7. Color surface.

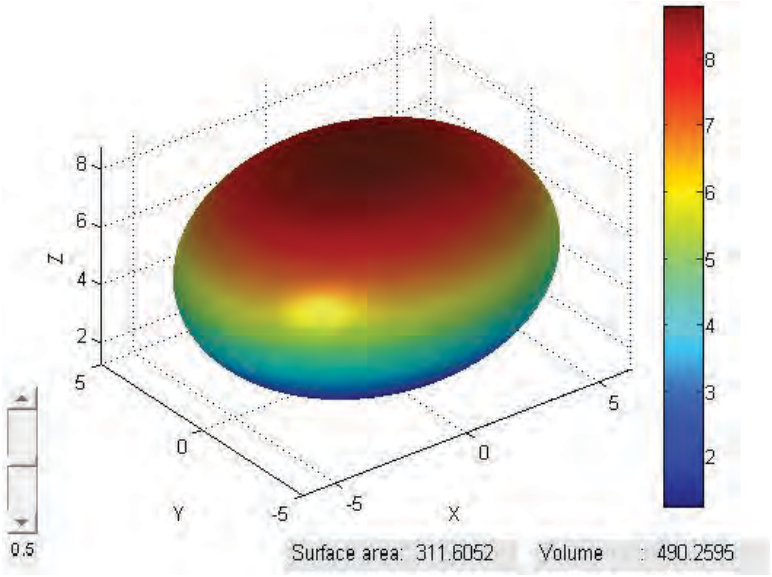

Figure 3-8. Light surface.

orthogonal to each other. The first maximum dimension is the longest one of the aggregate. We can measure all distances of any pair of points on the surface, and the longest distance is the first maximum dimension. P_i (x_i, y_i, z_i) and P_j (x_j, y_j, z_j) are any of the two points on the aggregate surface. The distance between the two points is D_{ij}:

$$D_{ij} = \sqrt{(x_j - x_i)^2 + (y_j - y_i)^2 + (z_j - z_i)^2} \qquad \text{Eq. 3-15}$$

$$D_l = \max_{1 \le i,j \le n} D_{ij} \qquad \text{Eq. 3-16}$$

where (x_i, y_i, z_i), (x_j, y_j, z_j) are coordinates of points P_i and P_j, D_{ij} is the distance between points P_i and P_j, D_l is the longest length, and n is the total number of the points on the surface.

In the next step we determine the intermediate dimension, which is perpendicular to both the longest dimension and the shortest dimension. Figure 3-10 illustrates the way we calculate the intermediate dimension. All the vertical planes

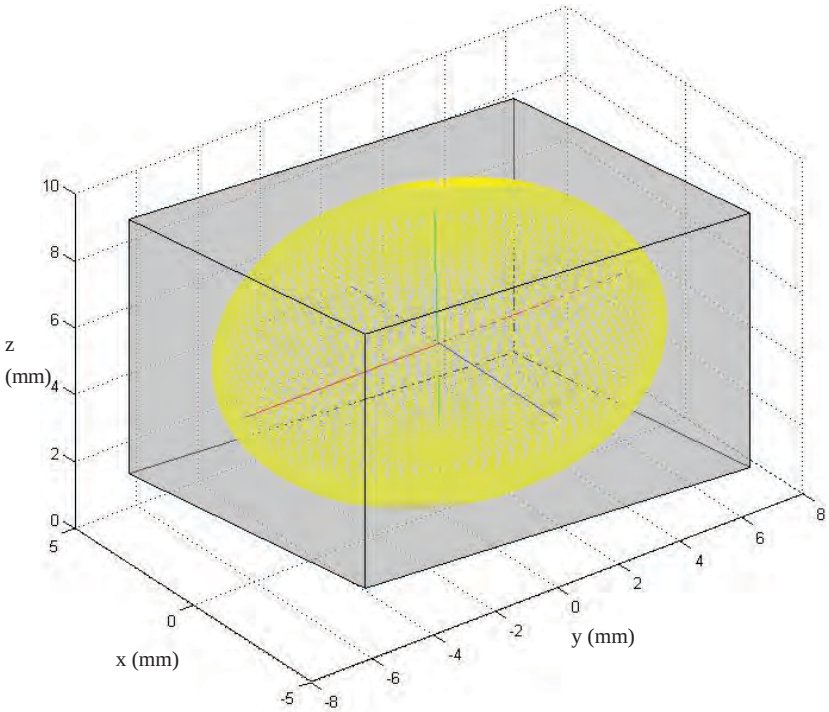

Figure 3-9. Three dimensions.

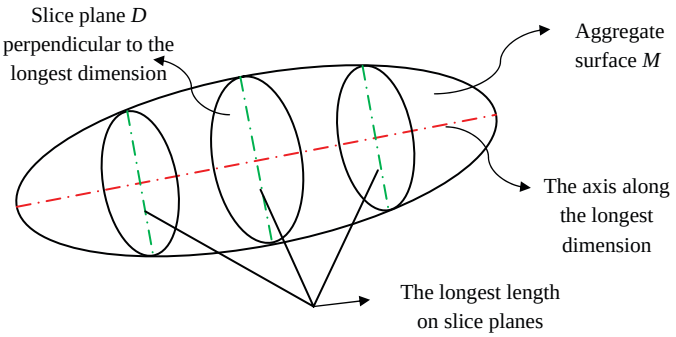

Figure 3-10. The intermediate dimension.

shown in Figure 3-10 are slices perpendicular to the longest dimension. We measure all the distances between the points intersecting the plane and the surface of the particle and get the longest one. The maximum of all the longest distances on all the slices is the second maximum dimension.

The point $P_r(x_r, y_r, z_r)$ is a joint point of the first maximum axis and the normal plane containing the second dimension. The direction of the first maximum axis is (a, b, c) or $(x_{m2} - x_{m1}, y_{m2} - y_{m1}, z_{m2} - z_{m1})$ (end points of the longest dimension). So the normal plane is:

$$a(x - x_r) + b(y - y_r) + c(z - z_r) = 0 \qquad \text{Eq. 3-17}$$

$$a = x_{m2} - x_{m1}, b = y_{m2} - y_{m1}, c = z_{m2} - z_{m1} \qquad \text{Eq. 3-18}$$

where (x_r, y_r, z_r) is the cross point between the longest dimension and a plane perpendicular to the longest dimension, (a, b, c) is the direction along the longest dimension, and (x_{m1}, y_{m1}, z_{m1}) and (x_{m2}, y_{m2}, z_{m2}) are the coordinates of two ends on the longest dimension.

Given (a, b, c) and (x_r, y_r, z_r) calculated using the aforementioned method, we can get every point coordinate on the plane D shown in Figure 3-10. There is a curved line of intersection between surface M and slice plane D. The maximum distance between two points on the curved intersection line is the longest length on the slice plane. The intermediate dimension is the maximum value among all these longest lengths on slice planes.

Finally, the shortest dimension is calculated as follows. The shortest dimension is perpendicular to both the longest dimension and the intermediate dimension. As shown in Figure 3-11, plane E is perpendicular to the intermediate dimension, and it is perpendicular to plane D with an intersection line. Obviously, any line on plane E is perpendicular to both axis A and axis B. The longest length G between two points on the intersection line F is defined as the shortest dimension.

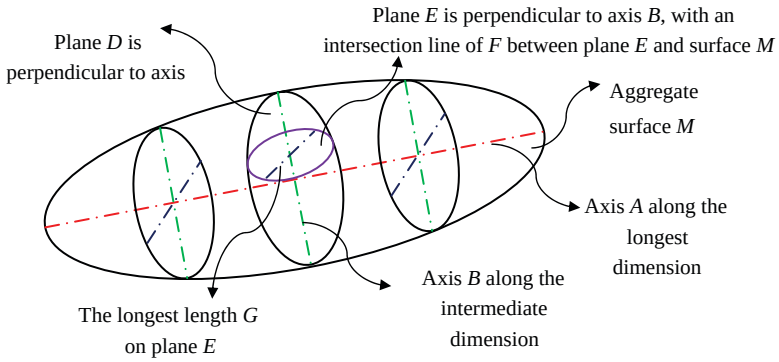

Figure 3-11. The shortest dimension.

CHAPTER 4

FTI Results

This chapter first verifies the accuracy and repeatability of the FTI results by comparing the dimension results using FTI results by different operators to manual measurements of the particles with standard shapes, such as triangular prism, circulate plate, and lens. After that, there are two sets of coarse aggregates, including seven types of aggregates in Aggregate Set 1 (hereinafter referred to as Set 1) and four types of aggregates in Aggregate Set 2 (hereinafter referred to as Set 2), and some fine aggregates imaged and analyzed using the FTI system. The FTI results of shape, angularity, and texture of various aggregates are presented and discussed. Detailed data for the shape, angularity, and texture of coarse aggregates can be found in Appendix E; images of the aggregates analyzed are presented in Appendix F.

4.1 Verification of FTI Results to Manual Measurements of Particles with Standard Shapes

To verify the accuracy of the FTI system, particles of standard shapes, such as triangular prism, circular plate, and lens, were analyzed using the FTI system by two different operators, and also manually measured using a Vernier caliper. Each particle was imaged by the first operator twice and by the second operator three times. The accuracy and repeatability of FTI system and analysis were verified by comparing FTI analysis results to manual measurements.

Figure 4-1 shows the images of a triangular prism particle acquired with the FTI system. In the plan view color map, dark areas at the center represent larger *z*-values, while darker areas at both ends indicate low points on the prism surface. The object's 2-D boundary is shown as a white line in Figure 4-1(c). Table 4-1 tabulates its dimensions by manual measurements and FTI analyses, and the differences between the FTI and manual measurements. All parameters are shown in Figure 4-1(d). The triangular prism has a height of 7.06 mm and a maximum length of 13.91 mm along the L4 direction with a vertex angle α of 91∞. In general, FTI analysis results are consistent with manual measurements with very small deviations, which verifies the accuracy of the FTI system. FTI results of length are more accurate than those of height. Deviation of height is 8.42%, while the maximum deviation of length is 2.56%. The calculated vertex angle α' is 86° based on FTI analysis results, with a deviation of 5°.

Figure 4-2 shows a circular plate particle imaged in the FTI system. In the plan view color map, the circled dark area represents larger *z*-values, and the object's 2-D boundary is shown as a white line in isometric shaded surface profile in Figure 4-2(c).

Table 4-2 presents dimensions of the circular plate by manual measurement and FTI analysis, and deviations of FTI results from manual measurements. FTI analysis results show good agreement with manual measurements. The plate has a height of 6.01 mm with a diameter of 24.97 mm. Deviations of height and diameter are 1.95% and 0.12%, respectively. The repeatability of the FTI system is validated by the good consistency between FTI results operated by different operators and the very close FTI results of remeasuring the same particle.

Figure 4-3 shows a lens imaged in the FTI system. In the plan view color map, the white area represents larger z-values, and the object's 2-D boundary is shown as a white line in isometric shaded surface profile in Figure 4-3(c). Table 4-3 shows dimensions of the lens by manual measurement and FTI analysis, and deviations. Deviations of height and diameter are 5.12% and 1.47%, respectively. There is a larger deviation in diameter than that of the circular plate due to a smaller diameter (11.97 mm).

Figure 4-4 shows the relationship between manual measurements and FTI analysis results. The manual measurement *x* is the average value of physical measurements of the parameters in all aggregates of standard shapes. The FTI analysis results of the corresponding parameters are labeled as *y*. As shown in this figure, the relationship between *x* and *y* can be regressed by a linear function. FTI analysis results show good agreement with the manual measurements as the correlation coefficient R^2 is 0.9957. Possible reasons for the deviations are windowing out of error areas along the surface boundary during surface

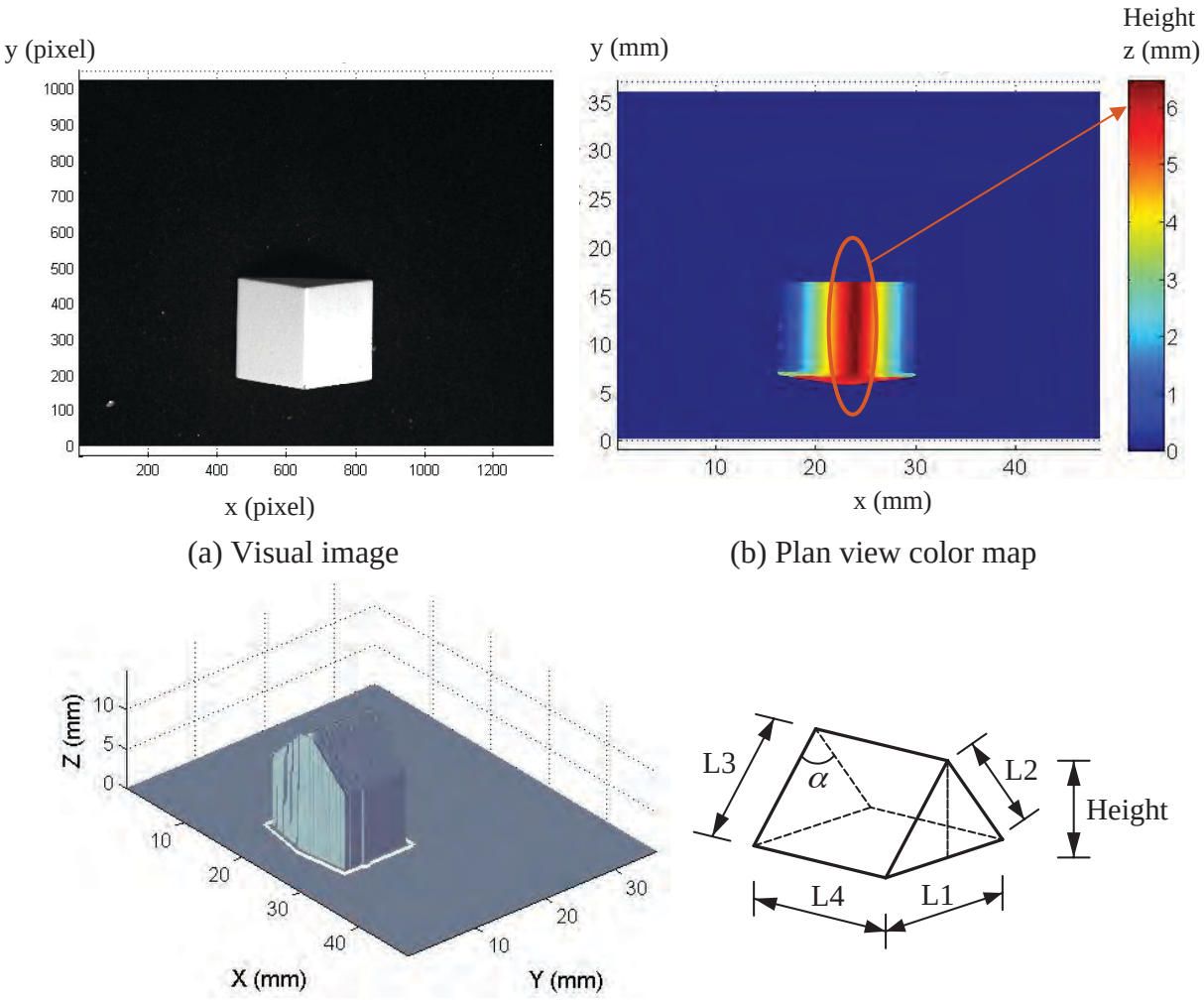

Figure 4-1. Triangular prism particle, imaged in the FTI system.

reconstruction and computation errors during MATLAB program analysis of data acquired from the FTI system.

4.2 FTI Results of Coarse Aggregates in Set 1

In Set 1, seven types of coarse aggregate with sizes ranging from ¾ in. to #4 are imaged and analyzed. The seven types of aggregate are blast furnace slag (BFS), copper ore, dolomite, crushed glacial gravel, rounded glacial gravel, iron ore, and limestone. For each type of aggregate, the four size ranges are passing a 1-in. sieve and retaining on a ¾-in. sieve (hereinafter referred to as ¾ in.), passing a ¾-in. sieve and retaining on a ½-in. sieve (hereinafter referred to as ½ in.), passing a ½-in. sieve and retaining on a ⅜-in. sieve (hereinafter referred to as ⅜ in.), and passing a ⅜-in. sieve and retaining on a #4 sieve (hereinafter referred to as #4). Table 4-4 presents the origins and physical properties of aggregates in Set 1. Table 4-5 presents the total number of aggregates imaged in the FTI system. These aggregates were selected for the purpose of evaluating whether the FTI system is able to detect some special aggregates due to the aggregate colors and the surface porosity.

Asymptotic analysis is performed to determine the required sample size for aggregate evaluations, at which constant morphological results can be achieved. Figure 4-5 through Figure 4-8 present the mean value sample size relationship for the shape factor (i.e., sphericity, flatness ratio, and elongation ratio), angularity, and texture for dolomite aggregates of sizes of ¾ in., ½ in., ⅜ in., and #4, respectively. As shown in these figures, 30 aggregate particles are sufficient for achieving stable and constant values for each morphological characteristic. Asymptotic analysis results of the other types of aggregates also lead to the same sample size requirement of 30 particles. Therefore, with the consideration of statistical stability, 30 aggregate particles are analyzed within each aggregate size range for every type of coarse aggregate.

Table 4-6 shows the average values of the five morphological parameters for the seven types of aggregate in Set 1. The

Table 4-1. Parameters of triangular prism by FTI analysis and manual measurement (unit: mm).

Triangular Prism	FTI Analysis		Manual Measurements		Deviation
Parameter	Analysis Results	Average	Measured Results	Average	(%)
Height	6.5455 6.4376 6.4469 6.4476 6.4510	6.4657	7.06 7.06 7.05	7.06	8.42
L1	13.7895 13.8250 13.9313 13.9313 13.9313	13.8817	13.91 13.91 13.91	13.91	0.20
L2	9.7513 9.8011 9.7438 9.7815 9.7734	9.7702	9.92 9.93 9.92	9.92	1.51
L3	9.7952 9.7507 9.8015 9.7832 9.8034	9.7868	9.91 9.92 9.92	9.92	1.34
L4	9.8954 9.9018 9.8201 9.7756 9.8633	9.8512	10.12 10.10 10.11	10.11	2.56

morphological parameters presented are sphericity, flatness ratio, elongation ratio, angularity, and texture. Each mean value of the morphological parameter in this table represents the mean value of the 30 aggregate particles of each type of aggregate within a specific size range. Further illustrations are presented in this section with figures.

4.2.1 Shape

Figure 4-9 presents the sphericity distribution of ¾-in. aggregate particles in Set 1. As we can see from the figure, both crushed glacial gravel and blast furnace slag have greater values of sphericity, whereas dolomite and iron ore have smaller sphericity among the seven types of aggregate. Sphericity distributions of rounded glacial gravel and limestone are very close.

Figure 4-10 shows the sphericity distribution of ½-in. aggregates of the seven types of aggregate in Set 1. Compared with ¾-in. aggregates, crushed glacial gravel still remains the largest in sphericity of the seven types of aggregate; iron ore has the smallest sphericity.

Figure 4-11 presents the sphericity distribution of ⅜-in. aggregates in Set 1. Both crushed glacial gravel and rounded glacial gravel aggregates have large sphericity values. Conversely, iron ore has the smallest sphericity values.

Figure 4-12 presents the sphericity distribution of #4 aggregates in Set 1. Both crushed glacial gravel and blast furnace slag have relatively larger values of sphericity; iron ore has smaller values of sphericity. Unlike the large dolomite aggregates (¾ in., ½ in., and ⅜ in.), dolomite #4 aggregates have the smallest sphericity values.

Figure 4-13 shows the distribution of the flatness ratio of ¾-in. aggregates in Set 1. Dolomite and rounded glacial gravel have smaller values of flatness ratios, whereas iron ore has the largest values of flatness ratio.

Figure 4-14 plots the distribution of the flatness ratio of ½-in. aggregates in Set 1. Aggregates of crushed glacial gravel and limestone have very close flatness ratio values. Different from the ¾-in. aggregates, dolomite has the greatest flatness ratio values, and iron ore has the smallest flatness ratio values.

Figure 4-15 presents the flatness ratio distribution of ⅜-in. aggregates in Set 1. In this figure, crushed glacial gravel and rounded glacial gravel have similar distributions, with large values of flatness ratio. The flatness ratios of iron ore and copper ore are smaller than those of other aggregates. Blast furnace slag, dolomite, and limestone have flatness ratio distributions very close to each other.

Figure 4-16 presents the flatness ratio distribution of #4 aggregates in Set 1. Similar to ⅜-in. aggregates, both

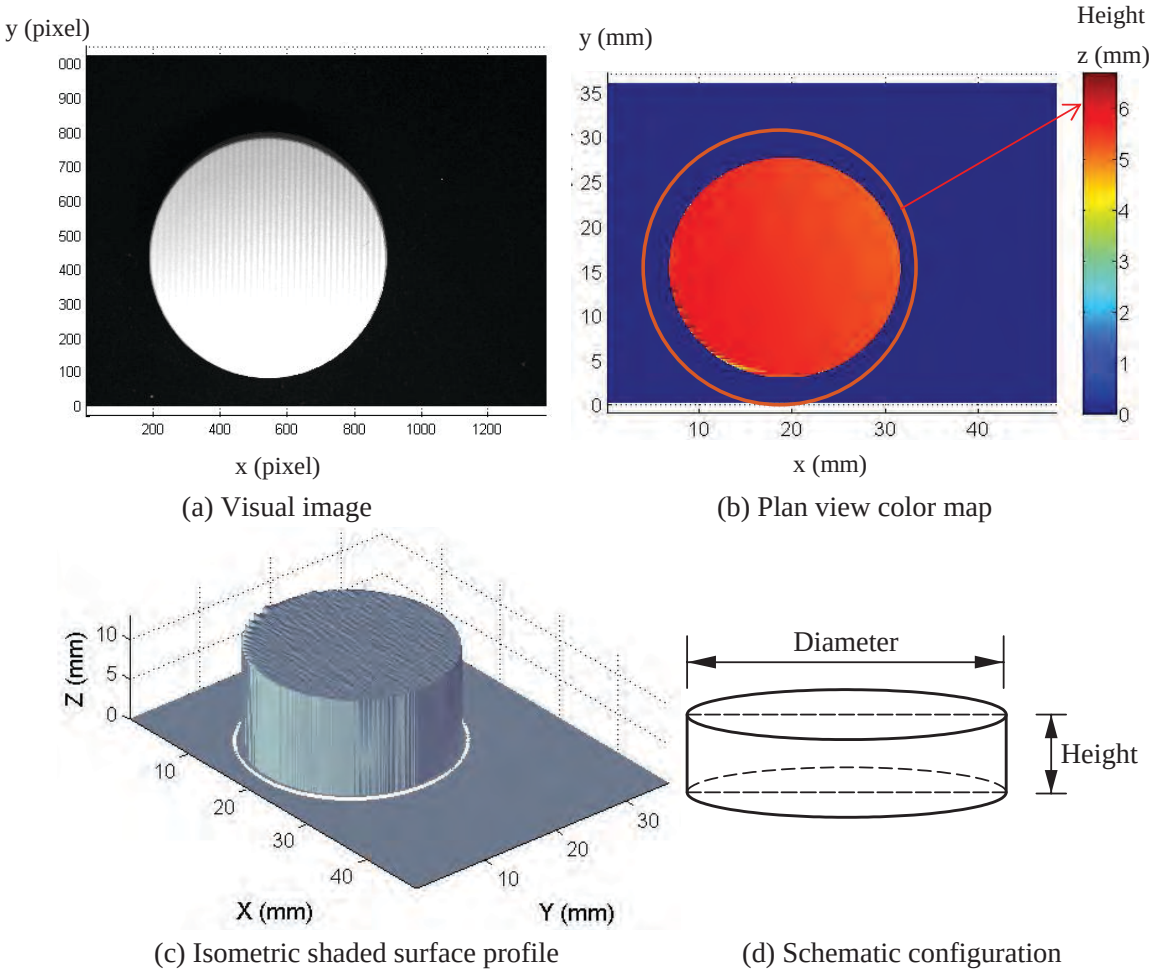

(a) Visual image

(b) Plan view color map

(c) Isometric shaded surface profile

(d) Schematic configuration

Figure 4-2. Circular plate particle, imaged in the FTI system.

crushed glacial gravel and rounded glacial gravel have large flatness ratio values, copper ore and dolomite have very close distributions, and iron ore has the smallest values of flatness ratio.

Figure 4-17 plots the elongation ratio distribution of ¾-in. aggregates in Set 1. Of the seven types of aggregate, crushed glacial gravel has the largest elongation ratios, and iron ore has the smallest elongation ratios. All the other aggregates have distributions of elongation ratios that are very close to each other.

Figure 4-18 shows the elongation ratio distribution of ½-in. aggregates in Set 1. In this figure, limestone has the

(*continued on page 27*)

Table 4-2. Parameters of circular plate by FTI analysis and manual measurement (unit: mm).

Circular Plate	FTI Analysis		Manual Measurements		Deviation
Parameter	Analysis Results	Average	Measured Results	Average	(%)
Height	5.9030 5.8730 5.9167 5.8846 5.8955	5.8946	6.01 6.01 6.01	6.01	1.91
Diameter	24.7010 24.6443 24.6443 24.6797 24.6797	24.6698	24.97 24.97 24.97	24.97	0.12

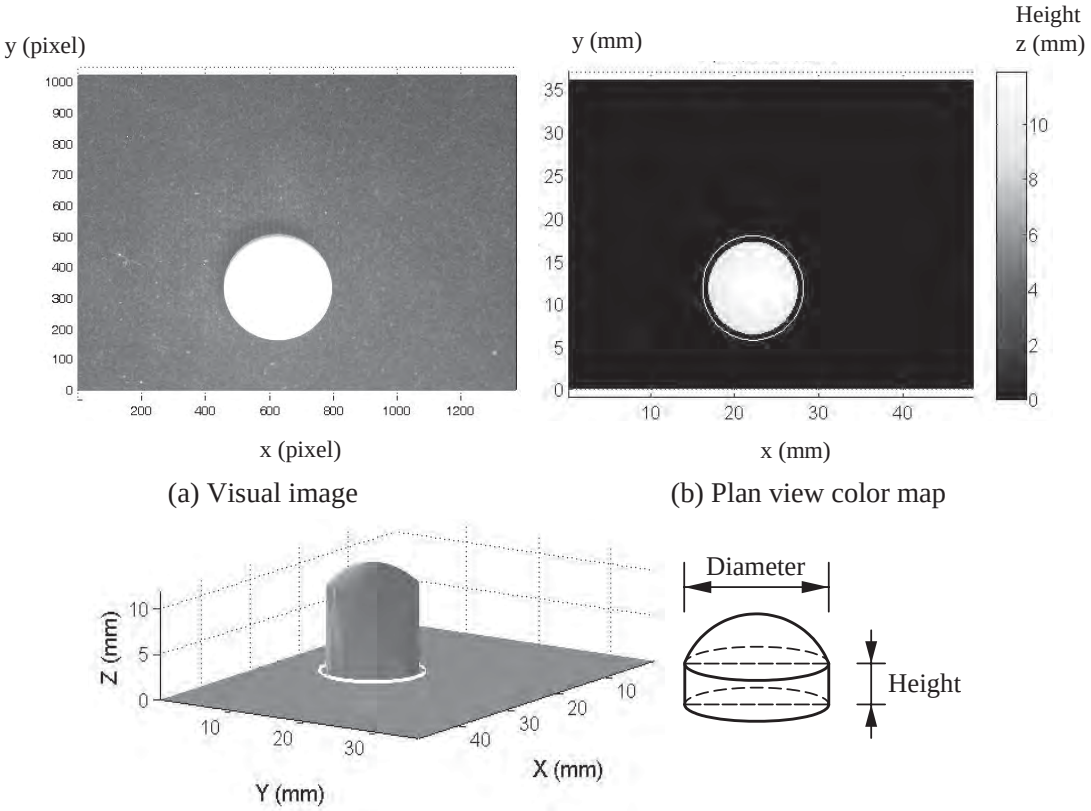

(a) Visual image (b) Plan view color map

(c) Isometric shaded surface profile (d) Schematic configuration

Figure 4-3. Lens, imaged in the FTI system.

Table 4-3. Parameters of lens by FTI analysis and manual measurement (unit: mm).

Lens	FTI Analysis		Manual Measurements		Deviation
Parameter	Analysis Results	Average	Measured Results	Average	(%)
Height	5.4978 5.5033 5.5123 5.5031 5.4877	5.5031	5.80 5.80 5.81	5.80	5.12
Diameter	11.8012 11.7876 11.7795 11.7937 11.8052	11.7942	11.97 11.96 11.97	11.97	1.47

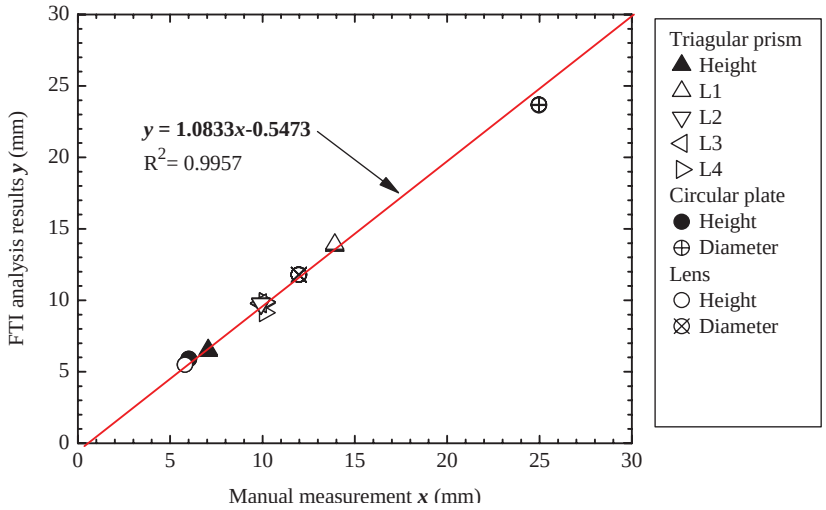

Figure 4-4. Comparison of dimensions by manual measurement to FTI analysis results for particles with standard shapes.

Table 4-4. Types and the physical properties of aggregates in Set 1.

Aggregate Type	Origin	Lithographic Description	LAA Loss (%)	Bulk Dry SpGr (g/cm^3)	24-hr Soak Absorption (%)
Blast furnace slag	Wayne, MI	Gray to black vesicular with poorly developed crystalline structure	43	2.27	3.18
Copper ore	Keweenaw, MI	Mixture of white, green, pink, and burgundy colors, fine to coarse grains	19	2.64	0.95
	Houghton, MI		16	2.76	2.12
Dolomite	Mackinac, MI	Light tan to light gray, medium to coarse crystals	27	2.78	0.52
	Monroe, MI	Tan, well-defined, small euhedral dolomite crystals	45	2.45	4.16
Glacial gravel – crushed	Kent, MI	Various colors	17	2.73	0.71
Glacial gravel – rounded	Kent, MI	Various colors	19	2.68	1.10
Iron ore	Marquette, MI	Black with hints of brown, very fine grained and hard metamorphic rock	11	—	—
Limestone	Schoolcraft, MI	Light tan with very fine subcrystalline texture	25	2.65	0.64
	Arenac, MI	Light gray, very fine crystalline with abundant frosted quartz sand grains	42	2.56	2.13

Note: LAA = Los Angeles abrasion; Bulk dry SpGr = Bulk dry specific gravity.

Table 4-5. Number of coarse aggregate particles imaged and analyzed in Set 1.

Aggregate Retaining Sieve Size		3/4”	1/2”	3/8”	#4
Aggregate Set 1	Blast furnace slag	30	30	30	30
	Copper ore	30	30	30	30
	Dolomite	30	30	30	30
	Glacial gravel – crushed	30	30	30	30
	Glacial gravel – rounded	30	30	30	30
	Iron ore	30	30	30	30
	Limestone	30	30	30	30
	Total number of aggregates	840			

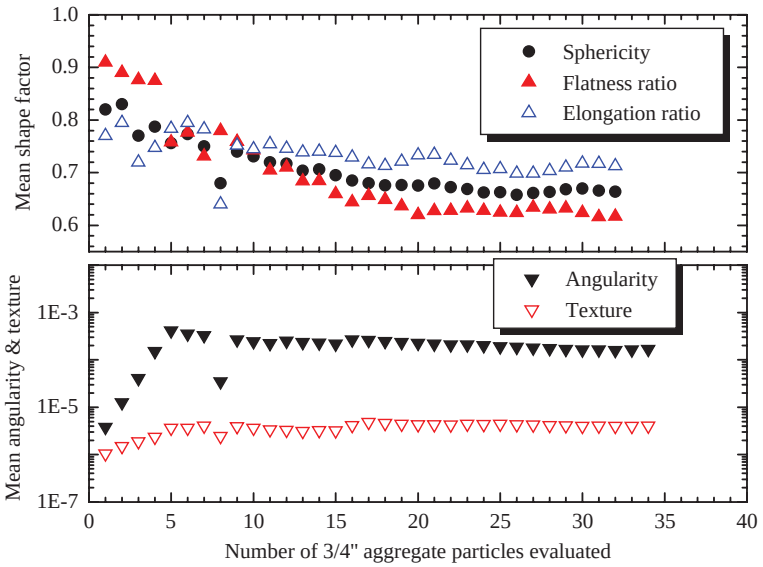

Figure 4-5. Asymptotic analysis to determine required sample size for ¾-in. dolomite aggregates.

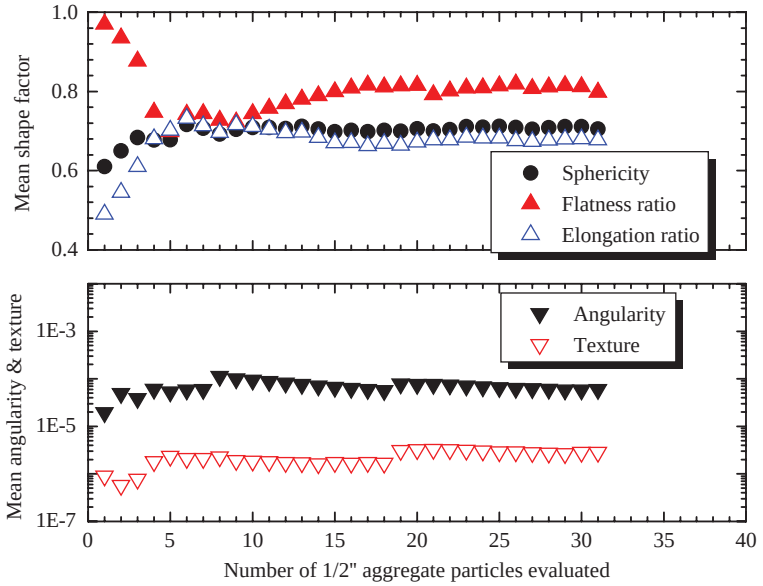

Figure 4-6. Asymptotic analysis to determine required sample size for ½-in. dolomite aggregates.

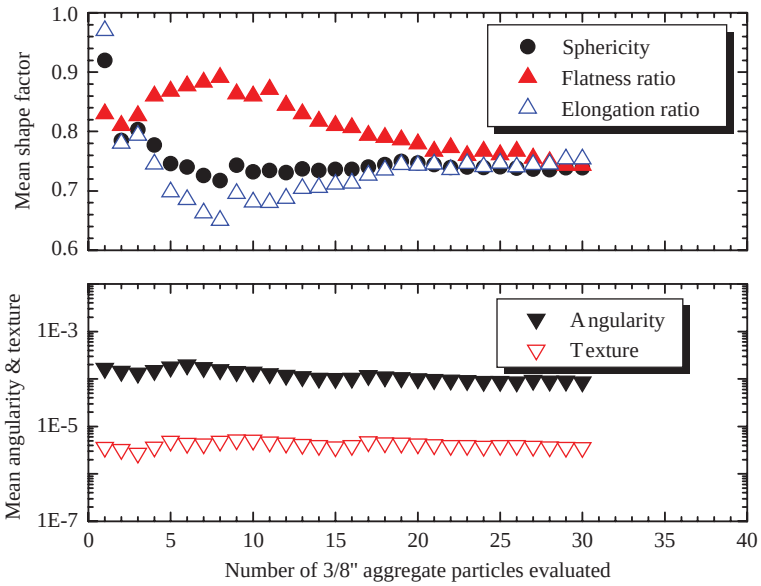

Figure 4-7. Asymptotic analysis to determine required sample size for ⅜-in. dolomite aggregates.

smallest values of elongation ratio, with very close distributions of all other types of aggregates.

Figure 4-19 is the elongation ratio distribution of ⅜-in. aggregates in Set 1. In this figure, iron ore has much smaller elongation ratios than all the other types of aggregate. Both crushed glacial gravel and rounded glacial gravel have greater values of elongation ratio, and the elongation ratio distributions of blast furnace slag and copper ore are very close.

Figure 4-20 depicts the elongation ratio distribution of #4 aggregates. Blast furnace slag aggregates are the most elongated; dolomite aggregates are the least elongated. The elongation ratio distributions of all the other aggregates are very close.

4.2.2 Angularity

Figure 4-21 plots the angularity distribution of all the ¾-in. aggregates in Set 1. It was found that crushed glacial gravel aggregates have the largest angularity values. Rounded glacial gravel and iron ore have smaller values of angularity compared to the other aggregates.

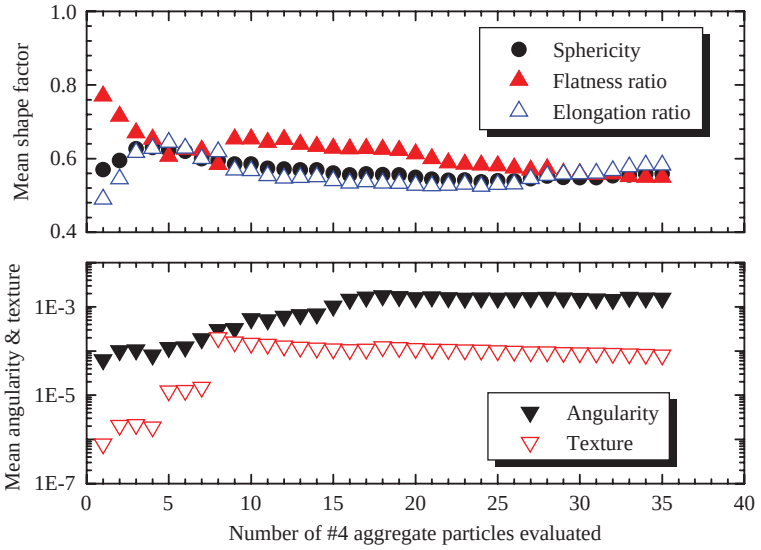

Figure 4-8. Asymptotic analysis to determine required sample size for #4 dolomite aggregates.

Table 4-6. Average values of morphological parameters of aggregates in Set 1.

Aggregate Size		Sphericity	Flatness Ratio	Elongation Ratio	Angularity	Texture
3/4" Aggregates	Blast furnace slag	0.72	0.72	0.73	2.74E-04	6.38E-06
	Copper ore	0.69	0.66	0.72	2.69E-04	4.97E-06
	Dolomite	0.66	0.62	0.71	1.58E-04	3.90E-06
	Glacial gravel – crushed	0.74	0.71	0.77	2.31E-04	3.86E-06
	Glacial gravel – rounded	0.68	0.59	0.75	8.44E-05	1.60E-06
	Iron ore	0.67	0.73	0.65	1.01E-04	2.13E-06
	Limestone	0.69	0.71	0.70	9.85E-05	2.52E-06
1/2" Aggregates	Blast furnace slag	0.72	0.76	0.72	2.44E-04	9.57E-06
	Copper ore	0.69	0.69	0.71	9.76E-05	4.69E-06
	Dolomite	0.70	0.80	0.68	5.99E-05	2.86E-06
	Glacial gravel – crushed	0.74	0.77	0.74	1.46E-04	2.70E-06
	Glacial gravel – rounded	0.70	0.71	0.71	9.71E-05	3.54E-06
	Iron ore	0.67	0.68	0.68	9.93E-05	5.17E-06
	Limestone	0.66	0.78	0.62	1.90E-04	4.60E-06
3/8" Aggregates	Blast furnace slag	0.73	0.73	0.75	2.19E-04	9.48E-06
	Copper ore	0.70	0.72	0.71	1.39E-04	4.39E-06
	Dolomite	0.74	0.75	0.75	8.74E-05	3.59E-06
	Glacial gravel – crushed	0.79	0.80	0.80	1.47E-04	6.94E-06
	Glacial gravel – rounded	0.79	0.78	0.80	1.09E-04	4.81E-06
	Iron ore	0.57	0.64	0.57	1.09E-03	7.75E-05
	Limestone	0.69	0.72	0.68	3.32E-04	1.59E-05
#4 Aggregates	Blast furnace slag	0.70	0.66	0.73	1.47E-03	6.00E-05
	Copper ore	0.60	0.59	0.64	4.25E-03	1.90E-04
	Dolomite	0.56	0.55	0.58	1.57E-03	8.23E-05
	Glacial gravel – crushed	0.69	0.71	0.69	2.48E-04	9.33E-06
	Glacial gravel – rounded	0.73	0.77	0.73	2.48E-04	1.44E-05
	Iron ore	0.58	0.53	0.63	2.16E-03	7.42E-05
	Limestone	0.65	0.63	0.67	1.25E-03	9.18E-05

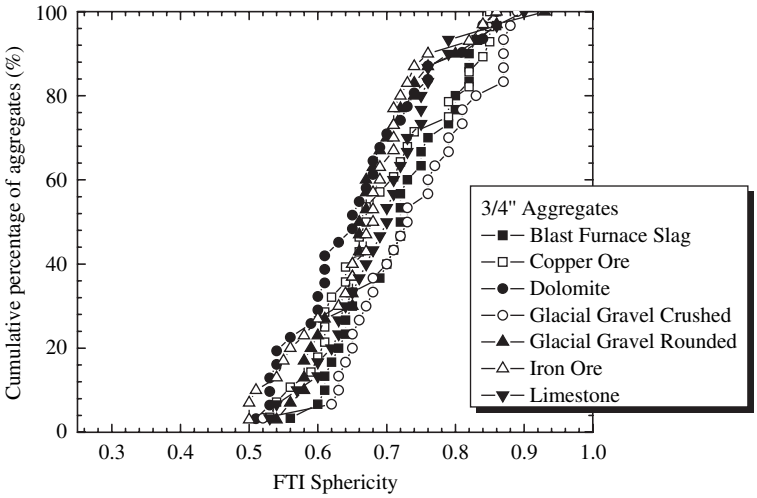

Figure 4-9. FTI sphericity distribution of ¾-in. aggregates in Set 1.

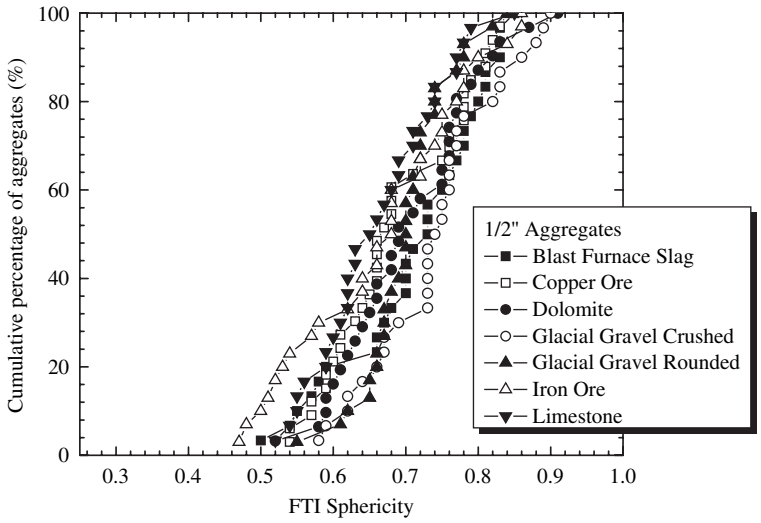

Figure 4-10. FTI sphericity distribution of ½-in. aggregates in Set 1.

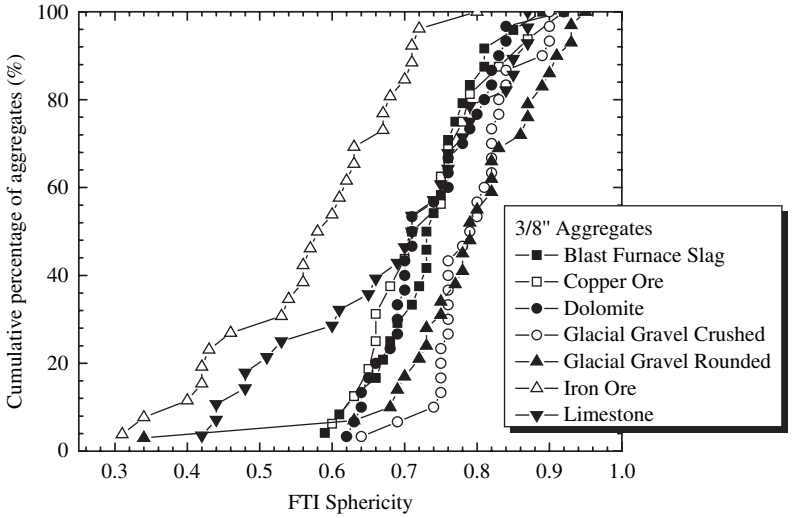

Figure 4-11. FTI sphericity distribution of ⅜-in. aggregates in Set 1.

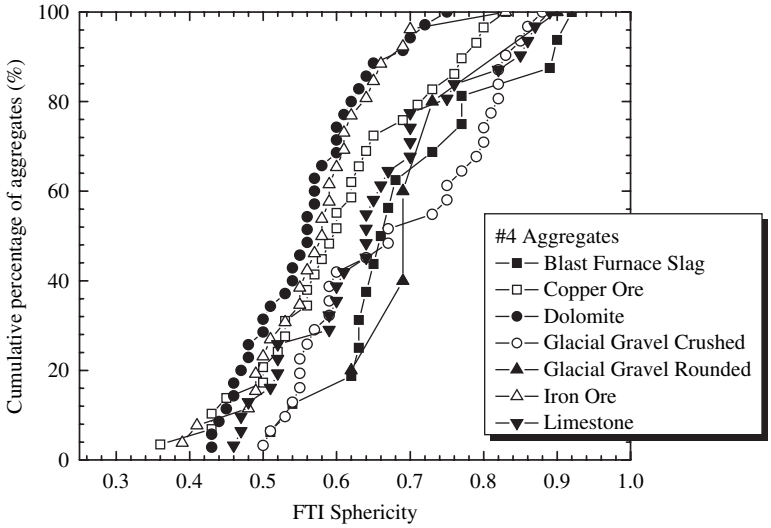

Figure 4-12. FTI sphericity distribution of #4 aggregates in Set 1.

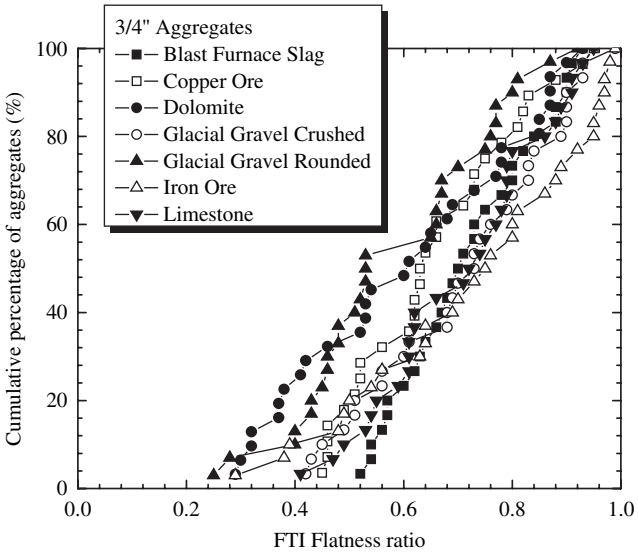

Figure 4-13. FTI flatness ratio distribution of ¾-in. aggregates in Set 1.

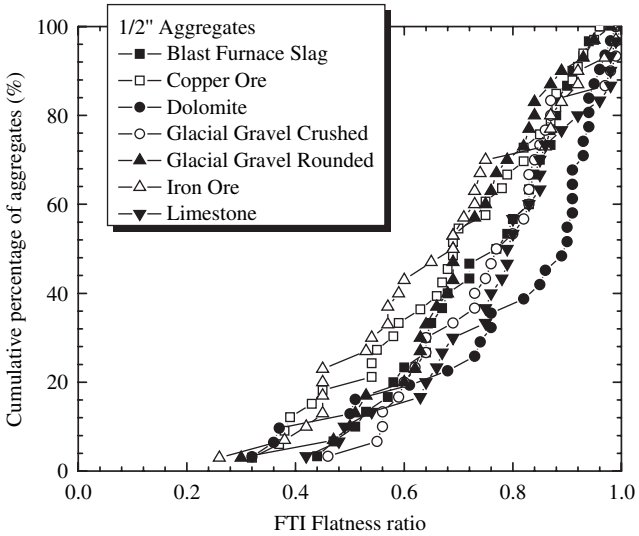

Figure 4-14. FTI flatness ratio distribution of ½-in. aggregates in Set 1.

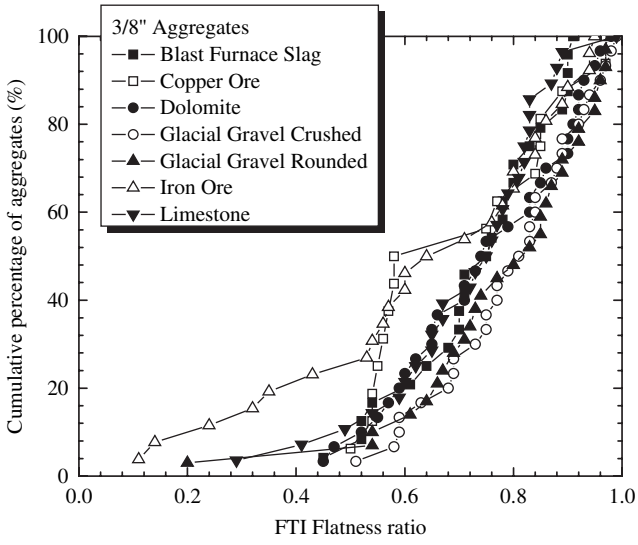

Figure 4-15. FTI flatness ratio distribution of ⅜-in. aggregates in Set 1.

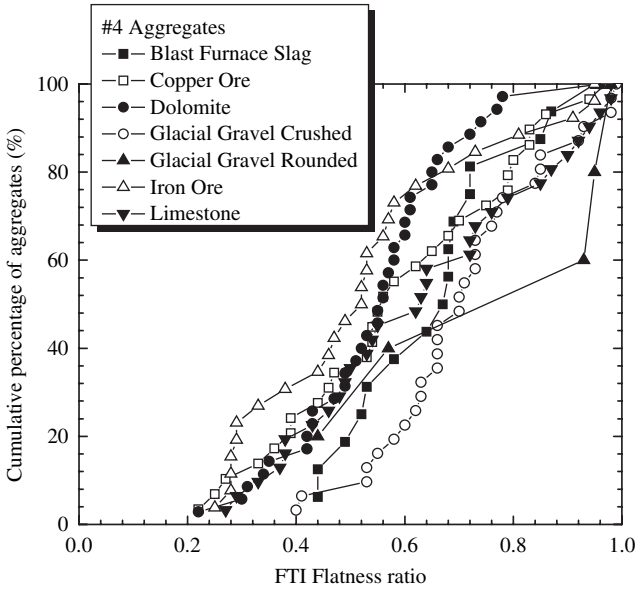

Figure 4-16. FTI flatness ratio distribution of #4 aggregates in Set 1.

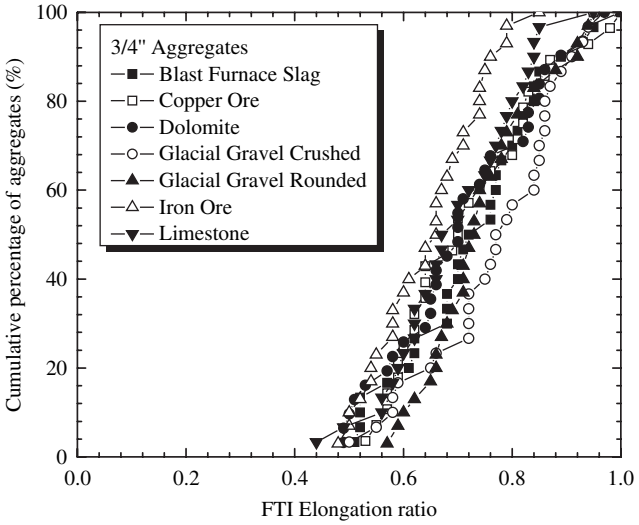

Figure 4-17. FTI elongation ratio distribution of ¾-in. aggregates in Set 1.

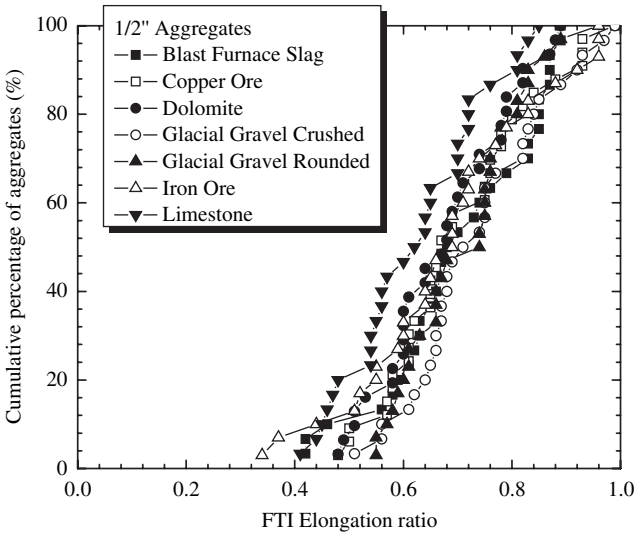

Figure 4-18. FTI elongation ratio distribution of ½-in. aggregates in Set 1.

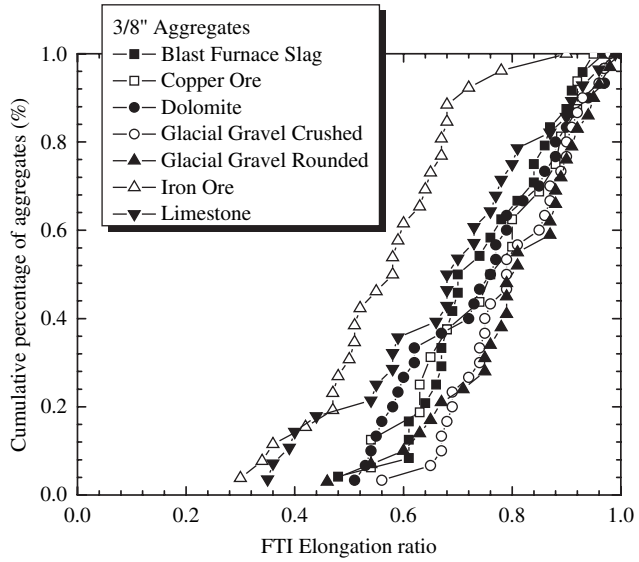

Figure 4-19. FTI elongation ratio distribution of ⅜-in. aggregates in Set 1.

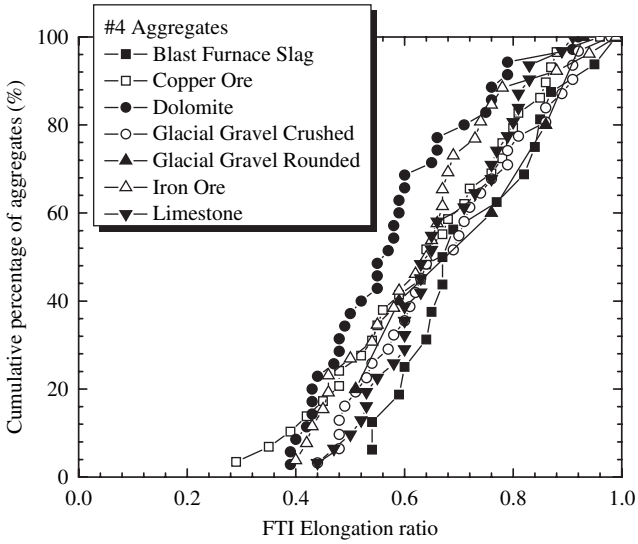

Figure 4-20. FTI elongation ratio distribution of #4 aggregates in Set 1.

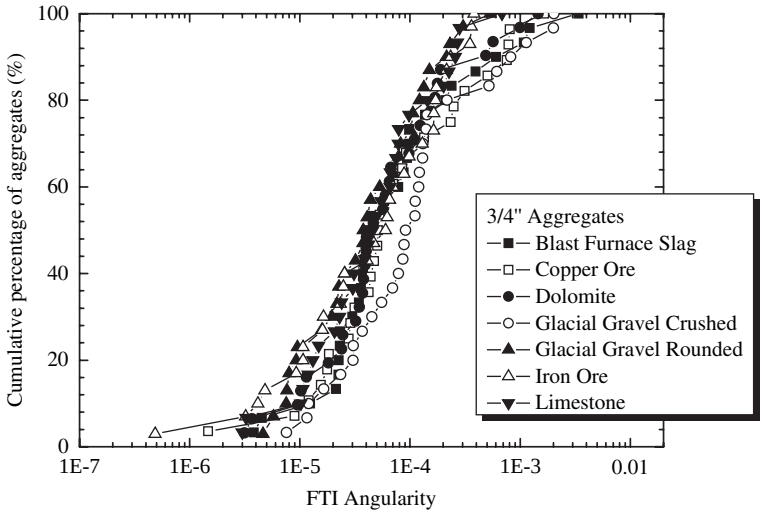

Figure 4-21. FTI angularity distribution of ¾-in. aggregates in Set 1.

Figure 4-22 depicts the angularity distribution of all the ½-in. aggregates in Set 1. All the aggregates have close distribution of angularity except dolomite aggregates, which have much smaller values.

Figure 4-23 shows the angularity distribution of all the ⅜-in. aggregates. Copper ore has the smallest angularity values; iron ore and limestone are the most angular aggregates of the seven types of aggregate. Rounded glacial gravel and dolomite have angularity distributions that are very close to each other.

Figure 4-24 presents the angularity distribution of all the #4 aggregates. Iron ore remains as the most angular aggregate. Unlike ⅜-in. aggregates, both copper ore and iron ore aggregates are very angular, whereas blast furnace slag aggregates are much less angular. From the angularity distribution figures, it can be inferred that angularity rankings of aggregates may be size dependent.

4.2.3 Texture

Figure 4-25 presents the texture distribution of ¾-in. aggregates in Set 1. As expected, rounded glacial gravel aggregates have the smoothest surfaces, whereas blast furnace slag aggregates have the roughest surfaces. Copper ore and dolomite have similar values of surface texture; iron ore and limestone have very close surface texture values.

Figure 4-26 plots the texture distribution of ½-in. aggregates in Set 1. As shown in this figure, blast furnace slag

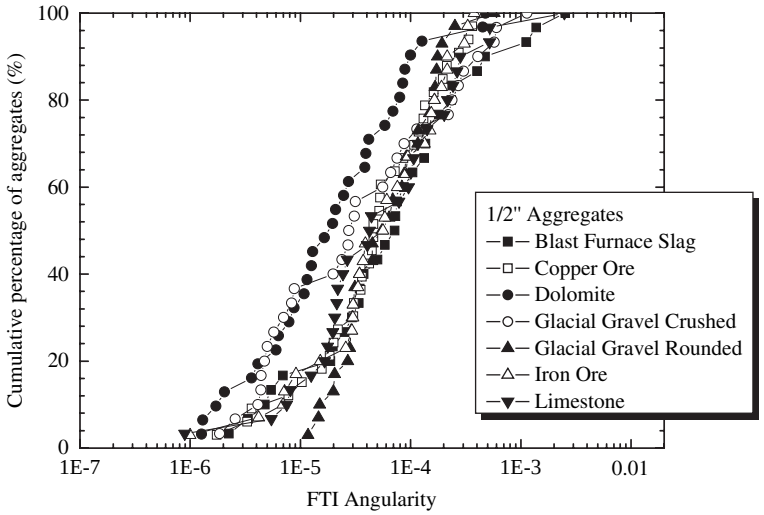

Figure 4-22. FTI angularity distribution of ½-in. aggregates in Set 1.

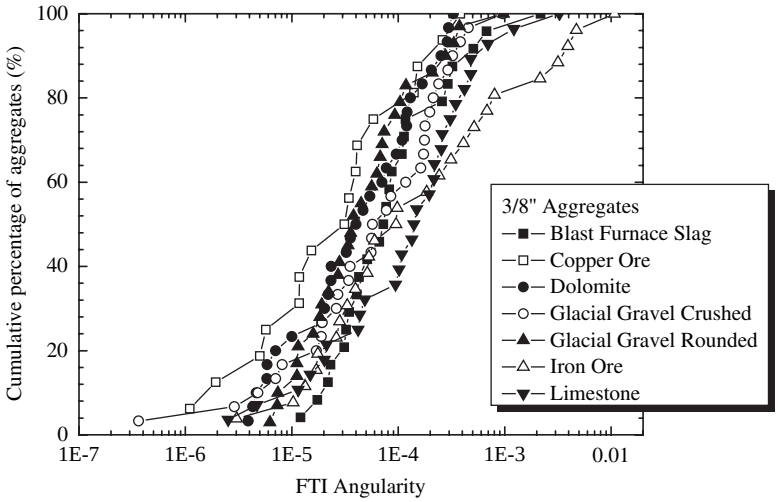

Figure 4-23. FTI angularity distribution of ⅜-in. aggregates in Set 1.

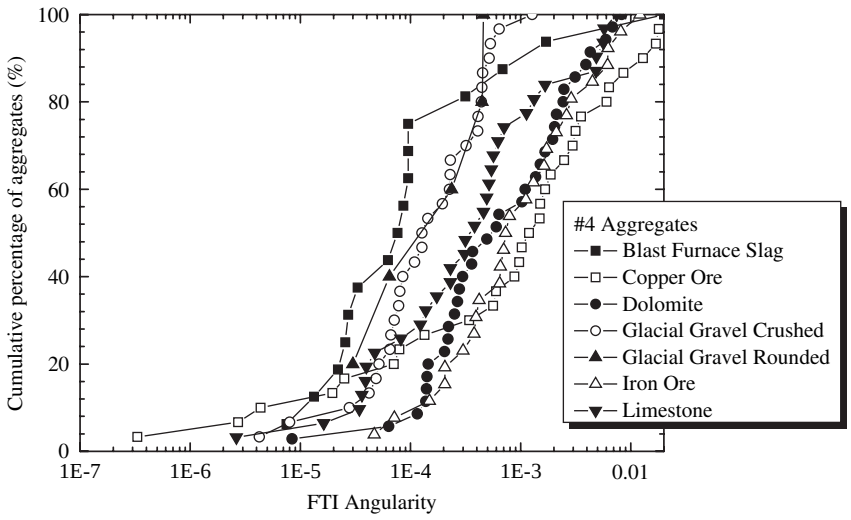

Figure 4-24. FTI angularity distribution of #4 aggregates in Set 1.

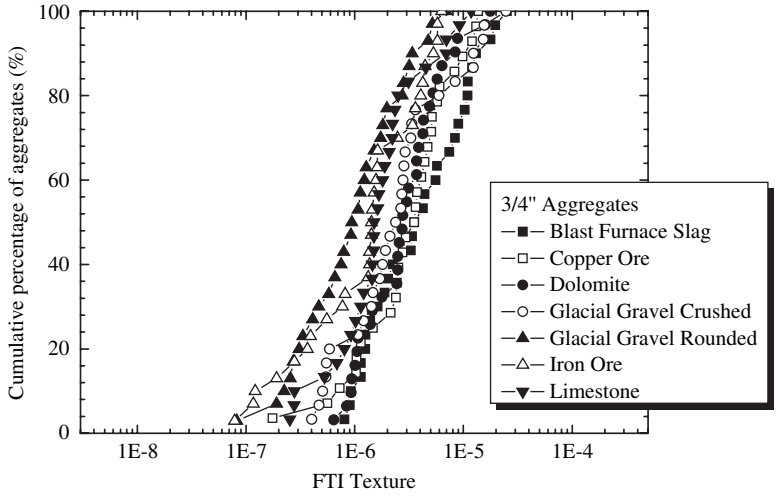

Figure 4-25. FTI texture distribution of ¾-in. aggregates in Set 1.

aggregates are the roughest, followed by iron ore. Copper ore and limestone have very close values of surface texture. Dolomite, crushed glacial gravel, and rounded glacial gravel have very similar surface textures, all of which are smoother than the other aggregates.

Figure 4-27 shows the texture distribution of ⅜-in. aggregates. Iron ore aggregates are the roughest, followed by limestone and blast furnace slag aggregates; copper ore and rounded glacial gravel aggregates have the smoothest surface textures.

Figure 4-28 depicts the texture distribution of #4 aggregates. Both crushed glacial gravel and rounded glacial gravel have very smooth surface textures. However, different from large aggregates (¾ in., ½ in., and ⅜ in.), copper ore #4 aggregates have the roughest surface texture, followed by limestone, dolomite, and blast furnace slag.

Table 4-7 shows the relative rankings of sphericity, flatness ratio, elongation ratio, angularity, and texture for coarse aggregates in Set 1 based on the average values of each morphological parameter shown in Table 4-6. The ranking indicates that rankings of morphological properties are size dependent.

4.3 FTI Results of Coarse Aggregates in Set 2

In Set 2, four types of aggregate (Broadway, Maymead, Salem, and Strasburg) were analyzed. There are five aggregate particles passing the ¾-in. sieve and retaining on the ½-in. sieve for each type of the four aggregates that were imaged and analyzed, and there are 20 particles in total imaged and analyzed. The 20 aggregate particles were

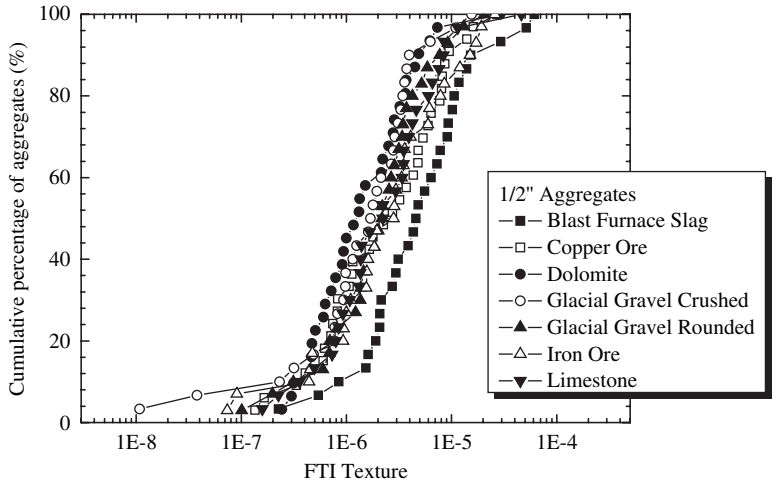

Figure 4-26. FTI texture distribution of ½-in. aggregates in Set 1.

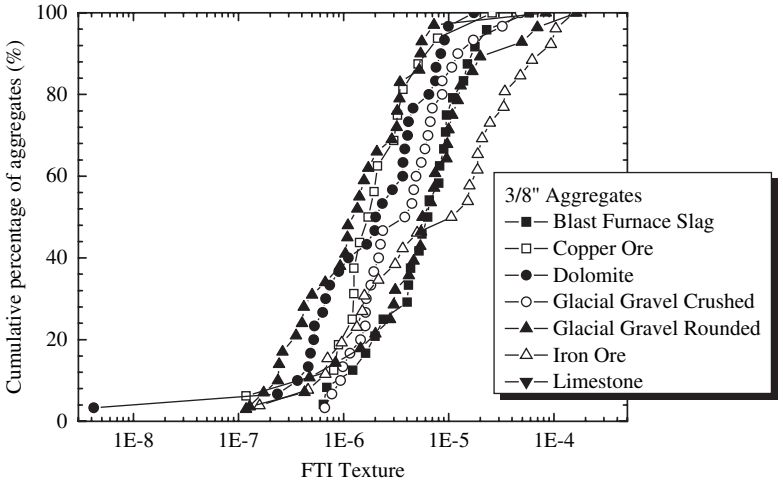

Figure 4-27. FTI texture distribution of ⅜-in. aggregates in Set 1.

scanned using the FTI system prior to the Micro-Deval tests. The FTI results of the original aggregates were referred to as "0-min. Micro-Deval FTI results." Then the 20 aggregate particles were subjected to the Micro-Deval test for 15 min., and scanned again using the FTI system. The FTI results (shape, angularity, and texture) of the 20 aggregate particles after 15 min. of Micro-Deval testing were referred to as the "15-min. Micro-Deval FTI results." The 20 aggregate particles were subjected to the Micro-Deval test for another 30 min., with a total of 45 min. of Micro-Deval testing. At the end of 45 min., the aggregate particles were imaged and analyzed using the FTI system again. The results will be hereinafter referred to as "45-min. Micro-Deval FTI results." The three sets of FTI results of the 20 aggregates were compared

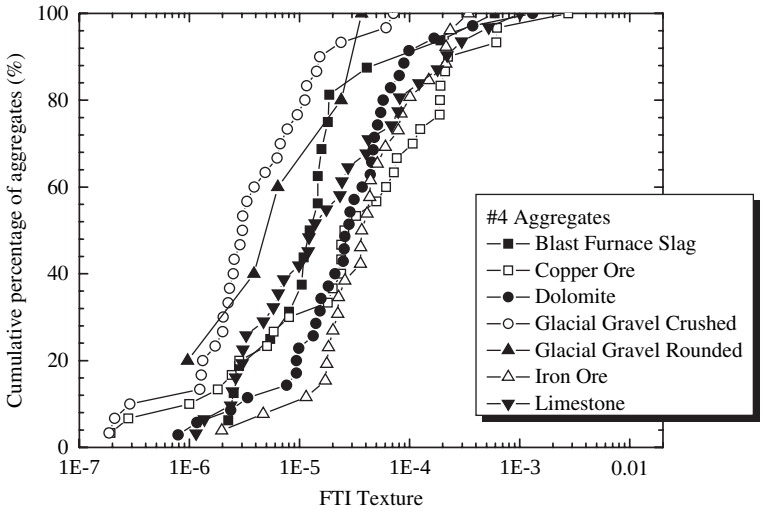

Figure 4-28. FTI texture distribution of #4 aggregates in Set 1.

Table 4-7. Ranking summary of shape, angularity, and texture for coarse aggregates in Set 1.

Aggregate Size	Ranking	1	2	3	4	5	6	7
3/4"	Sphericity	GGC	BFS	CO	LST	GGR	IO	DLT
	Flatness ratio	IO	BFS	GGC	LST	CO	DLT	GGR
	Elongation ratio	GGC	GGR	BFS	CO	DLT	LST	IO
	Angularity	BFS	CO	GGC	DLT	IO	LST	GGR
	Texture	BFS	CO	DLT	GGC	LST	IO	GGR
1/2"	Sphericity	GGC	BFS	DLT	GGR	CO	IO	LST
	Flatness ratio	DLT	LST	GGC	BFS	GGR	CO	IO
	Elongation ratio	GGC	BFS	CO	GGR	DLT	IO	LST
	Angularity	BFS	LST	GGC	IO	CO	GGR	DLT
	Texture	BFS	IO	CO	LST	GGR	DLT	GGC
3/8"	Sphericity	GGC	GGR	DLT	BFS	CO	LST	IO
	Flatness ratio	GGC	GGR	DLT	BFS	CO	LST	IO
	Elongation ratio	GGC	GGR	BFS	DLT	CO	LST	IO
	Angularity	IO	LST	BFS	CO	GGC	GGR	DLT
	Texture	IO	LST	BFS	GGC	GGR	CO	DLT
#4	Sphericity	GGR	BFS	GGC	LST	CO	IO	DLT
	Flatness ratio	GGR	GGC	BFS	LST	CO	DLT	IO
	Elongation ratio	BFS	GGR	GGC	LST	CO	IO	DLT
	Angularity	CO	IO	DLT	BFS	LST	GGC	GGR
	Texture	CO	LST	DLT	IO	BFS	GGR	GGC

Note: BFS = Blast furnace slag; CO = Copper ore; DLT = Dolomite; GGC = Glacial gravel – crushed; GGR = Glacial gravel – rounded; IO = Iron ore; LST = Limestone.

Table 4-8. Types of aggregates in Set 2.

Aggregate Source	Aggregate Description		Aggregate Size
Maymead	Granite	Non-carbonate	3/4"–1/2"
Salem	Quartzite		
Broadway	Dolomite	Carbonate	
Strasburg	Limestone		

Table 4-9. Average values of angularity and texture of aggregate in Set 2.

Micro-Deval Duration	0 Min.		15 Min.		45 Min.	
Morphological parameters	Angularity	Texture	Angularity	Texture	Angularity	Texture
Broadway	8.64E-05	3.30E-06	8.94E-05	3.62E-06	1.27E-04	1.05E-05
Maymead	1.58E-04	8.01E-06	1.17E-04	9.38E-06	2.86E-04	1.95E-05
Salem	1.22E-04	5.66E-06	1.03E-04	6.50E-06	2.06E-04	1.50E-05
Strasburg	1.02E-04	5.01E-06	9.26E-05	6.56E-06	9.73E-05	3.56E-06

with each other to detect the changes of both angularity and texture due to different durations of the Micro-Deval test. Table 4-8 shows the aggregate types in Set 2.

The tests and results presented in this section are to assess whether the FTI system is sensitive to detecting the angularity and texture changes due to the abrasion in the Micro-Deval test. The same particles are imaged before and after Micro-Deval testing of different durations. We assume that shape will not change significantly during Micro-Deval testing; therefore, only angularity and texture are analyzed in this section.

Table 4-9 shows the average values of angularity and texture for each type of aggregate in Set 2. Regardless of the duration of the Micro-Deval test, Broadway and Strasburg have relatively smaller angularity, and Maymead has the largest angularity of the four types of aggregate. An interesting observation is that the Micro-Deval test does not necessarily help to decrease the angularity of aggregates. Among the four types of aggregate, the angularities of Strasburg aggregates decreased from 1.02×10^{-4} for the unpolished to 9.26×10^{-5} after 15 min. of the Micro-Deval test, and finally to 9.73×10^{-5} after 45 min. of Micro-Deval. As the images were acquired from the same locations of the same aggregate particles, no statistical analysis is needed.

Figure 4-29 plots the mean value of FTI angularity and texture for Broadway in the 65% confidence interval of FTI angularity and texture for dolomite ½-in. aggregates in Set 1. Figure 4-30 plots the mean value of FTI angularity and texture for Strasburg in the 65% confidence interval of FTI angularity and texture for limestone ½-in. aggregates in Set 1. Mean values of FTI angularity and texture for Broadway and Strasburg aggregates show good correlations with the FTI angularity and

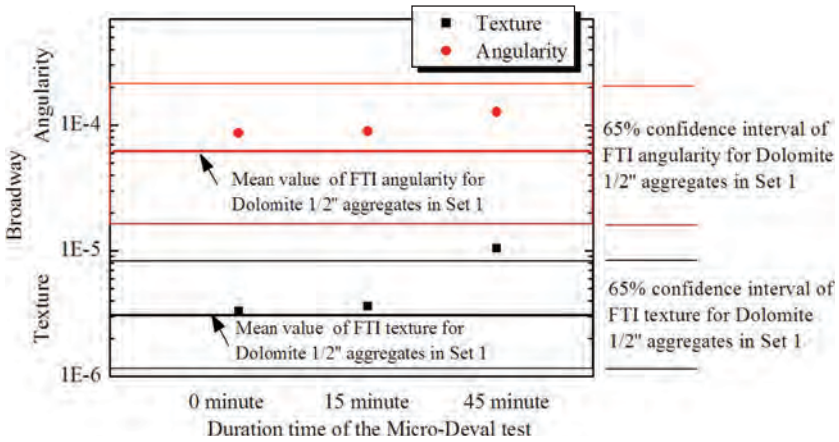

Figure 4-29. The mean value of FTI angularity and texture of Broadway in the 65% confidence interval of FTI angularity and texture for dolomite ½-in. aggregates in Set 1.

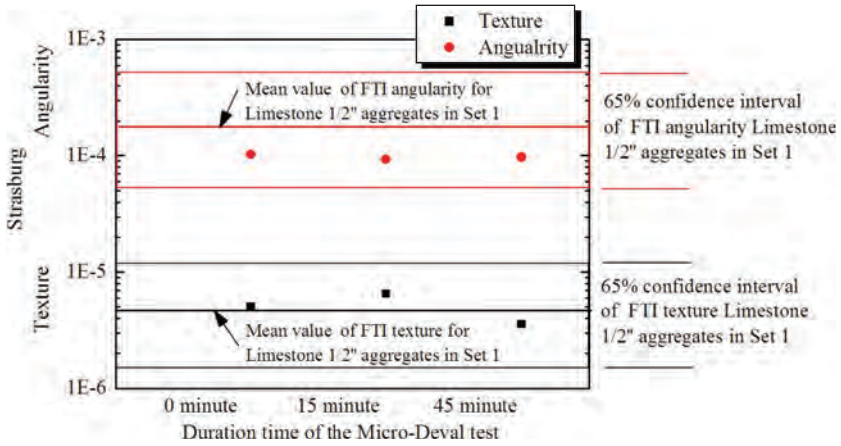

Figure 4-30. The mean value of FTI angularity and texture of Strasburg in the 65% confidence interval of FTI angularity and texture for limestone ½-in. aggregates in Set 1.

texture of dolomite and limestone ½-in. aggregates in Set 1, as the majority of mean values are reasonably distributed within the 65% confidence interval of FTI angularity and texture for dolomite and limestone ½-in. aggregates.

4.3.1 Graphical Presentation of Angularity

Due to the relatively small values of angularity and texture, it is hard to appreciate the sense of these values in the absolute scale. This subsection presents these values graphically so that one can make a better judgment about the relative ranking of these aggregates.

Figure 4-31 plots the angularity distribution of the aggregates before they are subjected to Micro-Deval testing, denoted as "after 0 min. of Micro-Deval." It can be seen that Broadway aggregates are the most angular; Salem and Strasburg have smaller angularity values.

Figure 4-32 shows the angularity distribution of the aggregates after being subjected to the Micro-Deval test for 15 min. Broadway and Strasburg have similar angularity distributions and smaller values, whereas Maymead and Salem have similar distributions with greater values.

Figure 4-33 shows the angularity distribution of aggregates after being subjected to the Micro-Deval test for 45 min. Both Maymead and Strasburg have larger angularity values. The FTI angularity ranking is consistent with the AIMS II result for aggregates after being subjected to 45 min. of the Micro-Deval test, shown in Appendix F. By compar-

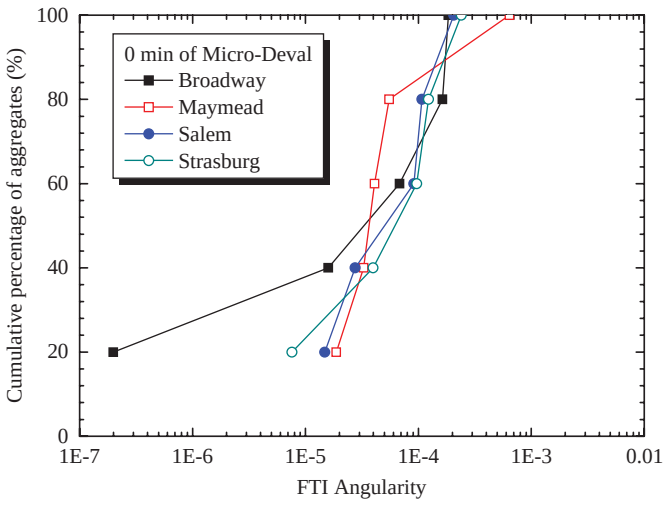

Figure 4-31. FTI angularity distribution before test.

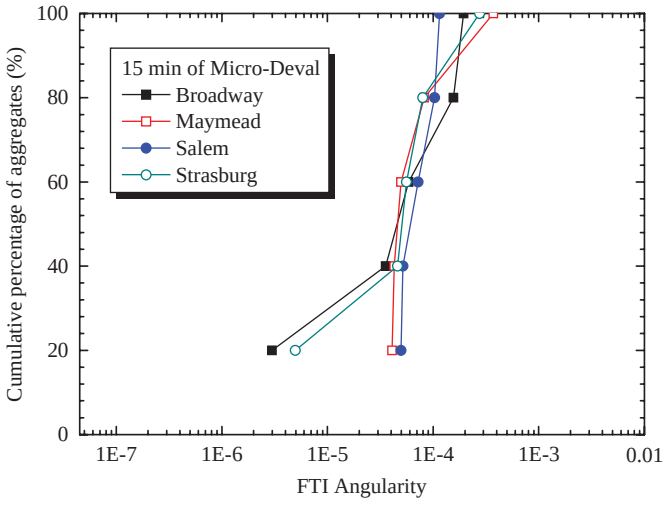

Figure 4-32. FTI angularity distribution after 15 min. of the Micro-Deval test.

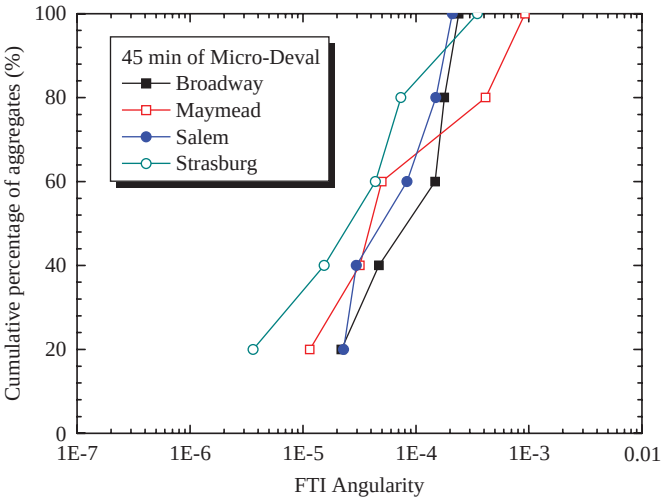

Figure 4-33. FTI angularity distribution of aggregates after 45 min. of the Micro-Deval test.

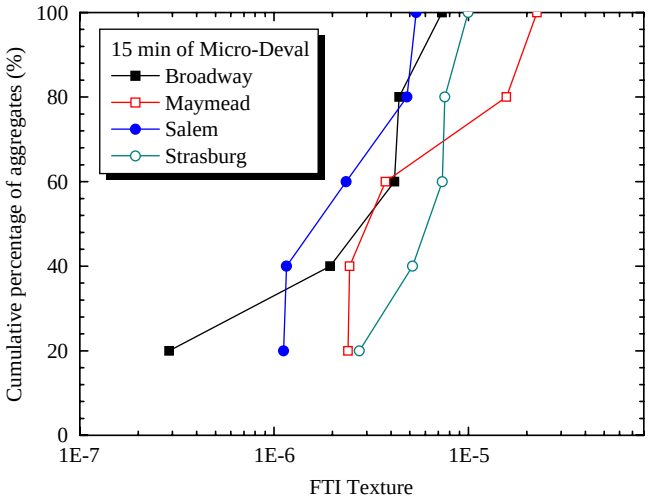

Figure 4-35. FTI texture distribution after 15 min. of the Micro-Deval test.

ing the angularity distributions in Figure 4-31, Figure 4-32, and Figure 4-33, it can be seen that aggregates having larger angularity tend to remain relatively more angular after the Micro-Deval test.

4.3.2 Graphical Representation of Texture

Figure 4-34, Figure 4-35, and Figure 4-36 plot the texture distributions for aggregates in Set 2 after Micro-Deval testing for 0 min., 15 min., and 45 min., respectively. Of the four types of aggregates, Maymead has the largest texture values, whereas Broadway and Strasburg have smaller texture values, regardless of the duration of the Micro-Deval test.

4.4 FTI Analysis of Fine Aggregates

Images in Figure 4-37 through Figure 4-39 show that the FTI system is capable of capturing high-resolution images of fine aggregates. Image processing and morphological analysis can also be performed on these images. The aggregate particles studied were #30 to #50 crushed limestone. For each particle, a set of images were taken: the left was taken under ambient light, and the right was taken under fringe illumination. The angular particle outlines and rough surface texture can be clearly seen from these images.

Several tests were conducted to illustrate the system's ability to image fine particles; examples of these images are shown

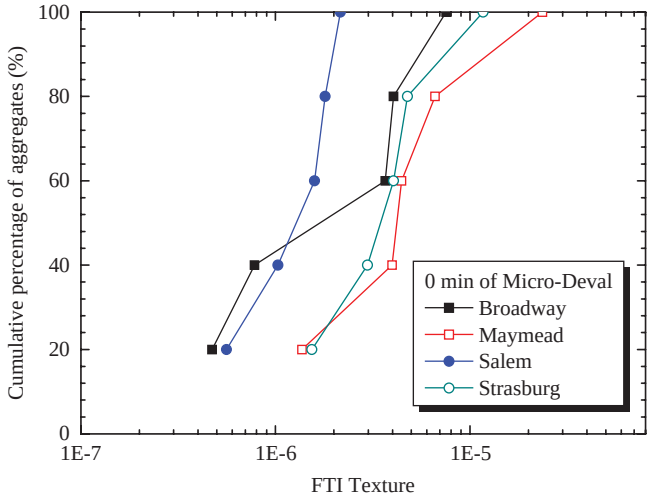

Figure 4-34. FTI texture distribution before test.

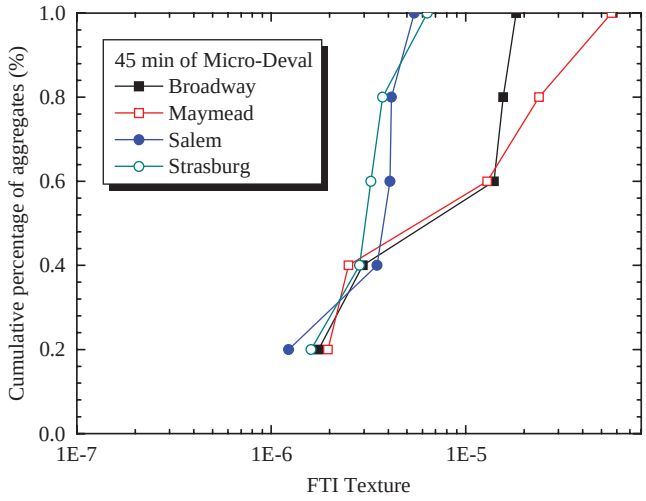

Figure 4-36. FTI texture distribution after 45 min. of the Micro-Deval test.

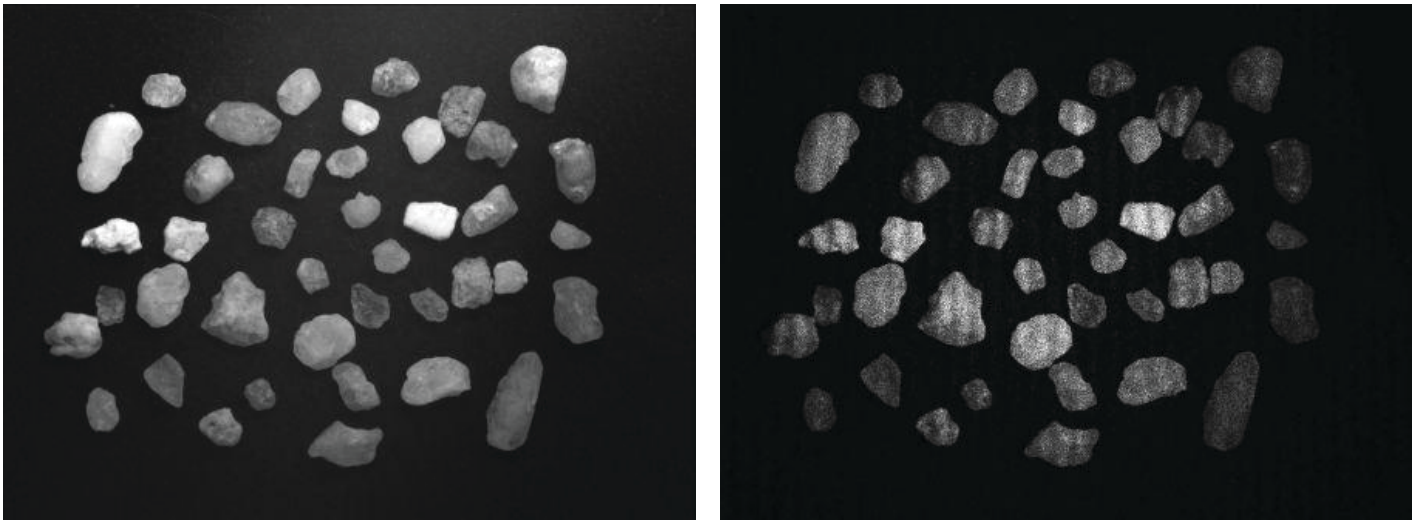

Figure 4-37. Crushed gravel (Montgomery, AL), #4–#8, magnification = 0.15.

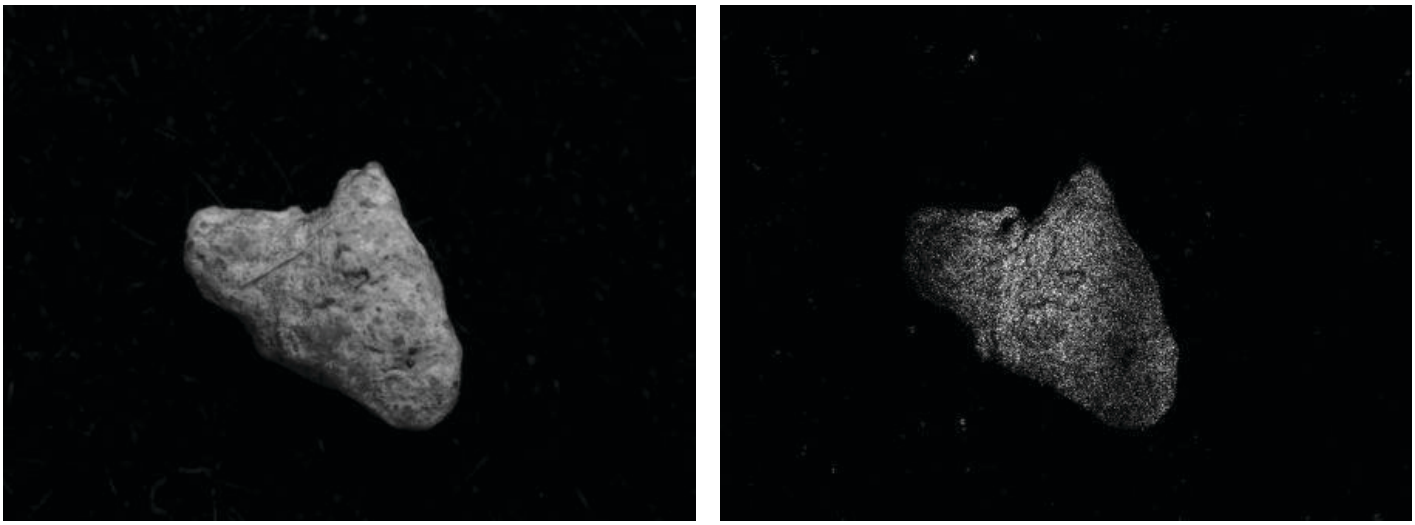

Figure 4-38. Crushed limestone (Brownwood, TX), #8–#16, magnification = 1.5.

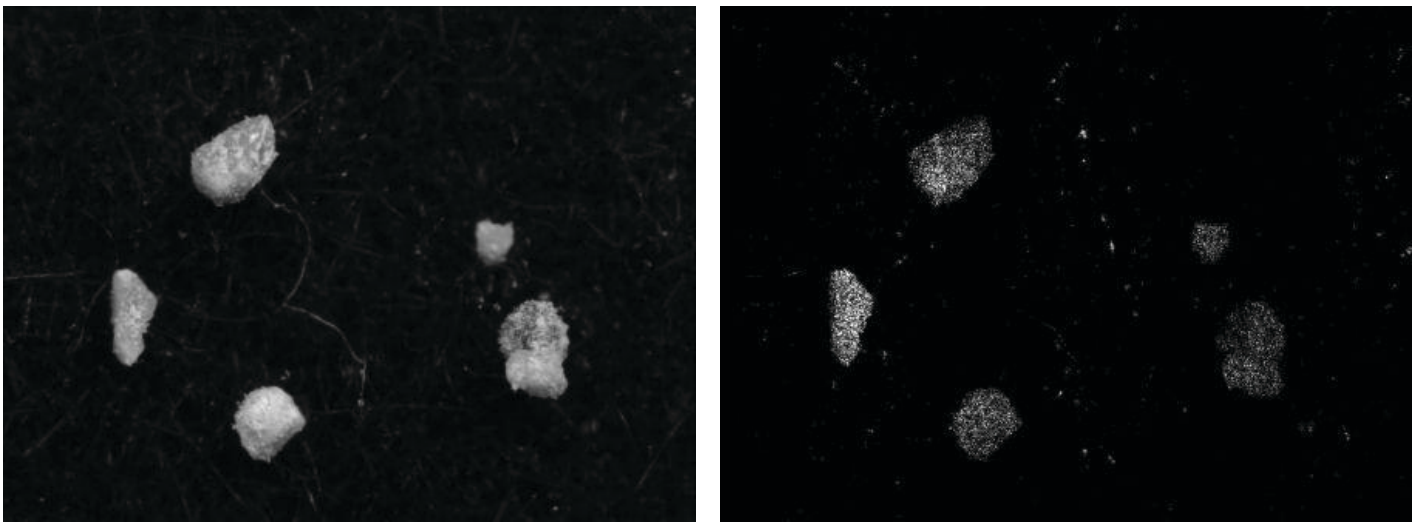

Figure 4-39. Crushed limestone (Brownwood, TX), #30–#50, magnification = 2.0.

in Figure 4-40 and Figure 4-41. In these figures, a small cap was filled nearly level with #50 glacial gravel sand, and a 3-D image was generated. The fine texture of the sand sample surface is clearly visible. No row-to-row errors were generated on this highly rough surface, so no error correction techniques are used here. It should be noted that the cup containing the aggregates in this test has a lip, which caused artifacts in the boundary calculation. Using a cup with straight sides should eliminate the boundary errors. Qualitative comparison with the commercial systems illustrates the fundamental resolution of the systems. In the case of the FTI system, the row-by-row processing technique means that there is slightly higher resolution of fine detail in the *y* direction than in the *x* direction. In both directions, the fine detail is better than the line-scan system, and comparable to the XCT system.

The #8 and #16 glacial gravel—rounded (GGR) and glacial gravel—crushed (GGC) aggregates were analyzed using the FTI system. The FTI analysis results of GGR and GGC fine aggregate and the other fine aggregates are discussed in Chapter 6.

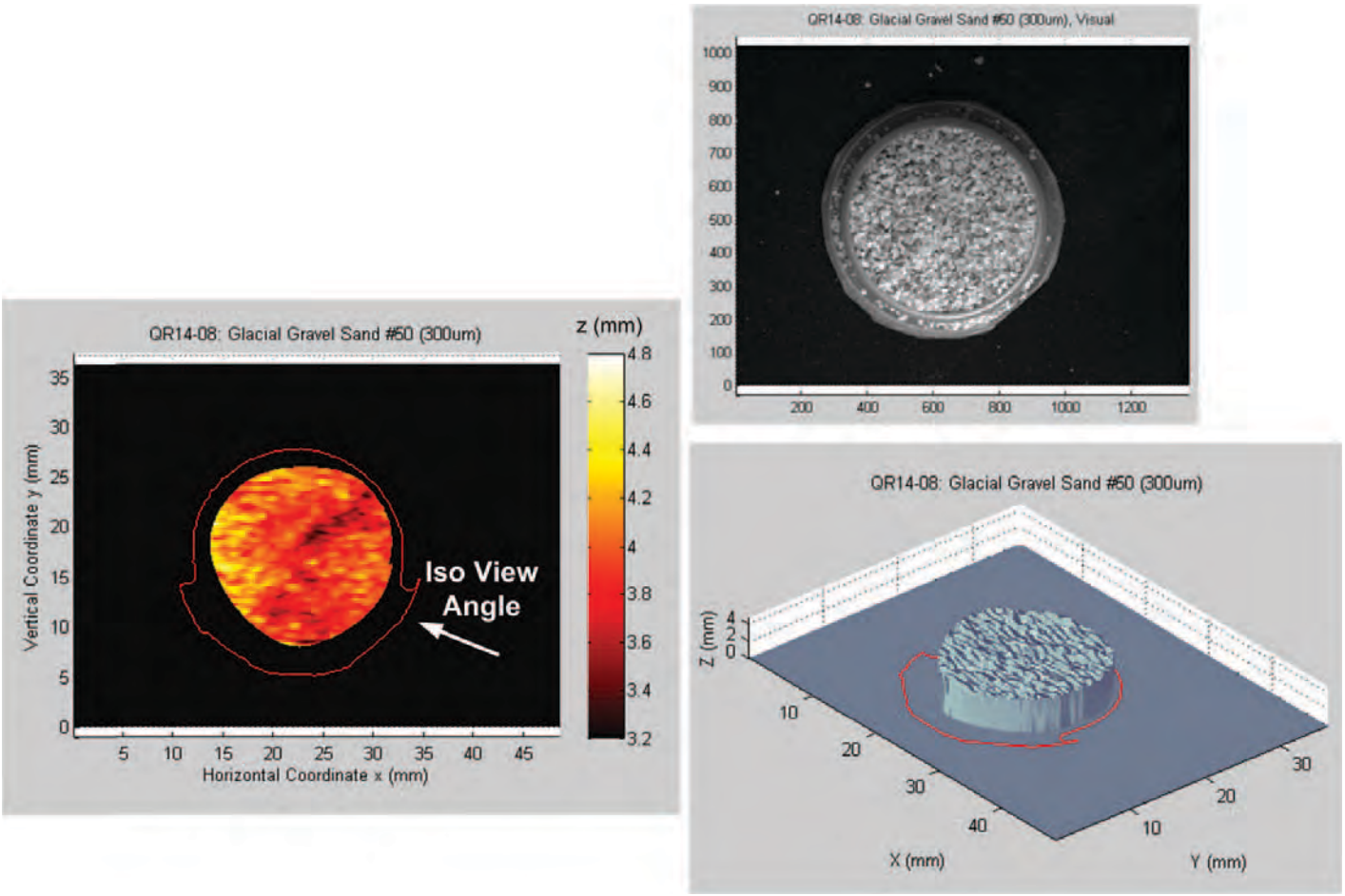

Figure 4-40. Glacial gravel sand #50, imaged in the FTI system.

(a) Visual image (b) XCT image (c) in laser line-scan system

Figure 4-41. Glacial gravel sand #50, imaged in other commercial systems.

CHAPTER 5

Statistical Analysis

Complete distributions provide more information when comparing the morphological characteristics of different aggregates. However, statistical parameters, such as mean and standard deviation, can be used to represent the entire distribution and distinguish different aggregates more concisely and conveniently. Data transformation (square root of original values) has been performed for data analysis since it better fits the normal distribution. In Appendix H, the histogram and normal quantile plots have been developed using the statistical software JMP for the seven types of coarse aggregate in Set 1. A statistical analysis has been conducted to compare the variability of different measurement methods and determine whether the differences among the measurement methods for sphericity, flatness ratio, elongation ratio, angularity, and texture are significant. The statistical analysis includes both ANOVA and *t*-test using JMP.

5.1 Analysis of Variance

ANOVA can be used to compare several groups of observations, which are independent and possibly have a different mean for each group. A test of importance is whether all the means are equal statistically. The basic assumptions of the ANOVA test are as follows:

1. Sample data are collected using a simple random sampling method,
2. Sample groups are independent from each other,
3. There are equal variances across groups, and
4. Each group follows a normal distribution.

5.1.1 ANOVA for Coarse Aggregates in Set 1

The ANOVA test performed in this section is used to compare sphericity and FE ratio of all seven coarse aggregates in Set 1 and to determine whether the differences among the measurement methods are significant for shape characteristics. Angularity and texture characteristics cannot be directly compared to each other using ANOVA in JMP because the angularity term and texture term are defined differently. The ANOVA test can only detect whether there are significant differences between results using different methods (i.e., FTI, AIMS II, UIAIA, and manual measurement). Once there is a difference between means of these groups, Tukey's HSD test is conducted via JMP to determine which mean is significantly different from the others. Table 5-1 presents the method groups for ANOVA. There are three methods used to characterize sphericity and four methods to characterize FE ratios for all the coarse aggregates in Set 1.

ANOVA test for sphericity:

H_0: $\mu_1 = \mu_2 = \mu_3$
H_a: at least one mean differs

where μ_1, μ_2, μ_3 are the means of sphericity using the FTI system, the AIMS II system, and the manual measurements, respectively. Set $\alpha = 0.05$; reject H_0 if p-value $< \alpha = 0.05$. Multiple comparison tests should be conducted using Tukey's HSD test.

ANOVA test for FE ratio:

H_0: $\mu_1 = \mu_2 = \mu_3 = \mu_4$
H_a: at least one mean differs

where μ_1, μ_2, μ_3, μ_4 are the means of FE ratio using the FTI, AIMS II, and UIAIA systems, and manual measurements, respectively. Set $\alpha = 0.05$, reject H_0 if p-value < 0.05 ($\alpha = 0.05$), and then multiple comparison tests should be conducted. Herein Tukey's HSD test is performed.

Table 5-2 and Table 5-3 show the ANOVA summaries for sphericity and FE ratio of the seven types of aggregate in Set 1. ANOVA plots of sphericity and FE ratio for copper ore aggregates via JMP are then shown for illustration in Figures 5-1 through 5-8.

5.1.2 ANOVA for Coarse Aggregates in Set 2

The ANOVA test is also performed in JMP to detect whether there is significant difference among the means of three FTI

Table 5-1. Analysis method groups for ANOVA.

Sphericity		FE Ratio	
Method	**Group**	**Method**	**Group**
FTI	1	FTI	1
AIMS II	2	AIMS II	2
Manual measurement	3	UIAIA	3
		Manual measurement	4

Table 5-2. ANOVA summary of sphericity for Set 1.

Sphericity	3/4”	1/2”	3/8”	#4
BFS	The FTI mean is smaller than the other two means.	No significant difference among three means.	No significant difference among three means.	No significant difference among three means.
CO	No significant difference among three means.	No significant difference among three means.	The FTI mean is greater than the other two means.	No significant difference among three means.
DLT	No significant difference among three means.	No significant difference among three means.	The FTI mean is greater than the other two means.	The FTI mean is the smallest, and the AIMS II mean is the greatest.
GGC	No significant difference among three means.	The AIMS II mean is significantly greater than the other two means.	The manual measurement mean is significantly smaller than the other two means.	No significant difference among three means.
GGR	The FTI result is smaller than the other two means.	The FTI mean is the greatest, and the AIMS II mean is the smallest.	The manual measurement mean is significantly smaller than the other two means.	No significant difference among three means.
IO	No significant difference among three means.	No significant difference among three means.	No significant difference among three means.	No significant difference among three means.
LST	The FTI mean is very close to the manual measurement mean.	The FTI mean is very close to the manual measurement mean.	No significant difference among three means.	No significant difference among three means.

Table 5-3. ANOVA summary of FE ratio for Set 1.

FE Ratio	3/4"	1/2"	3/8"	#4
BFS	The FTI mean is greater than the AIMS II and manual measurement means.	No significant difference among the four means.	No significant difference among the four means.	The FTI mean is very close to both the AIMS II and manual measurement means.
CO	The FTI is slightly greater than the AIMS II and UIAIA means.	No significant difference among the four means.	No significant difference among the four means.	The UIAIA mean is significantly smaller than the other three means.
DLT	No significant difference among the four means.	The UIAIA mean is significantly smaller than the other three means.	The FTI and UIAIA means are very close, and both are much smaller than the AIMS II and manual measurement means.	The UIAIA mean is significantly smaller than the other three means.
GGC	No significant difference among the four means.	The AIMS II mean is significantly smaller than the other three means.	The manual measurement mean is significantly greater than the other three means.	The FTI mean is very close to the manual measurement mean,
GGR	The FTI mean is the greatest mean, and the AIMS II mean is the smallest.	The AIMS II mean is significantly smaller than the other three means.	The manual measurement and UIAIA means are much greater than the FTI and AIMS II means.	No significant difference among the four means.
IO	No significant difference among the four means.	No significant difference among the four means.	No significant difference among the four means.	No significant difference among the four means.
LST	The FTI mean is very close to the manual measurement mean.	The FTI mean is very close to the manual measurement mean and the UIAIA mean.	No significant difference among the four means.	The FTI, AIMS II, and manual measurement means are very close to each other.

result groups for coarse aggregates in Set 2 [i.e., FTI results before Micro-Deval testing (hereinafter referred to as "MD-0 min."), FTI results after 15 min. of Micro-Deval testing (hereinafter referred to as "MD-15 min."), and FTI results after 45 min. of Micro-Deval testing (hereinafter referred to as "MD-45 min.")].

The hypothesis of the ANOVA test for FTI angularity is as follows:

H_0: $\mu_1 = \mu_2 = \mu_3$
H_a: at least one mean differs

where μ_1, μ_2, μ_3 are the means of the FTI angularity for MD-0 min., MD-15 min., and MD-45 min., respectively. Set $\alpha = 0.05$; reject H_0 if p-value $< \alpha = 0.05$. Multiple comparison tests should be conducted using Tukey's HSD test.

The hypothesis of the ANOVA test for FTI texture is as follows:

H_0: $\mu_1 = \mu_2 = \mu_3$
H_a: at least one mean differs

where μ_1, μ_2, μ_3 are the means of the FTI texture for MD-0 min., MD-15 min., and MD-45 min., respectively. Set $\alpha = 0.05$; reject H_0 if p-value $< \alpha = 0.05$. Multiple comparison tests should be conducted using Tukey's HSD test.

The ANOVA test results are plotted in Figure 5-9 through Figure 5-16. All the ANOVA tests show that there is insufficient sample evidence to indicate that the duration of the Micro-Deval test has an effect on the true mean of FTI angularity (or texture) of the five Broadway (or Maymead, Salem, and Strasburg) aggregates. Possible reasons leading to such a conclusion are as follows: (1) the fact that some groups have a variance that is greater than twice the variances of the other groups may violate the third ANOVA assumption of equal variance among groups, and (2) a small sample population of five may violate the forth ANOVA assumption of normal distribution. Therefore, a large sample population of aggregates going through Micro-Deval tests at different times is necessary to study the abrasion effect on aggregates due to the different durations of

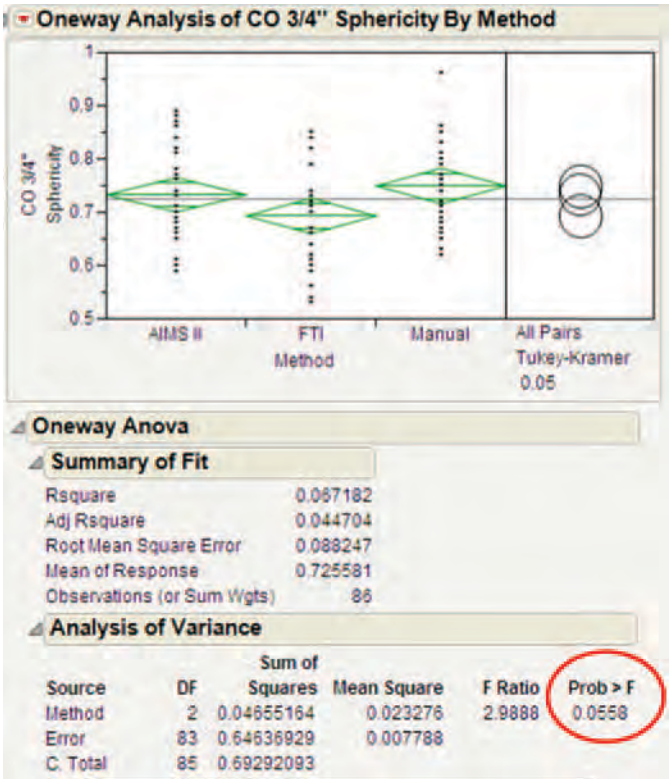

Note: Since p-value = 0.0558 > 0.05, fail to reject H_0. Therefore, there is no significant difference between the AIMS II, FTI, and manual measurement means.

Figure 5-1. One-way ANOVA of sphericity for copper ore ¾-in. aggregates.

Micro-Deval tests. Future research should be conducted on this topic using the FTI system.

5.2 Unpaired *t*-Test Analysis

The *t*-test analysis assesses whether the means of two groups are statistically different from each other. The *t*-test can be used to check the validity of the FTI results in comparison to manual measurement results. Flatness ratios of all the ¾-in. aggregates in Set 1 are compared. Since the variance of the FTI results and manual measurements might be different, the unpaired *t*-test with unequal variances is performed via JMP. The unpaired *t*-test assesses whether the two groups of flatness ratio results are statistically different in the evaluation of the same aggregates. The unpaired *t*-test is performed as follows:

H_0: $\mu_1 = \mu_2$, there is no difference in the mean values between the FTI results and the manual measurements

H_a: $\mu_1 \neq \mu_2$, there is a difference in the mean values between the FTI results and the manual measurements

where μ_1 and μ_2 are, respectively, the mean values of the flatness ratio using the FTI system and manual measurements for each type of aggregate. Set $\alpha = 0.02$; reject H_0 if p-value < $\alpha = 0.02$.

Table 5-4 shows the unpaired *t*-test results of the aggregates in Set 1. According to the *t*-test results, no significant

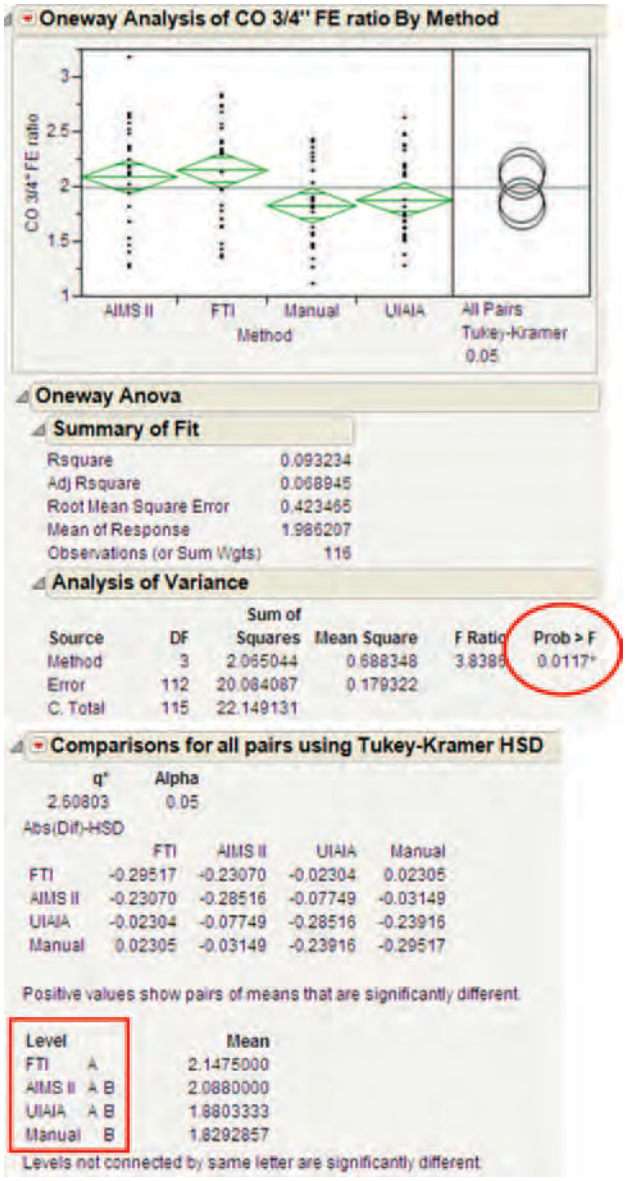

Note: Since p-value = 0.0117 < 0.05, reject H_0. Therefore, there is sufficient sample evidence to support that there are significant differences among the four means. Tukey's HSD test suggests that the manual mean (level B) is slightly smaller than the AIMS II and UIAIA means, whereas the FTI mean (level A) is slightly greater than the AIMS II and UIAIA means.

Figure 5-2. One-way ANOVA of FE ratio for copper ore ¾-in. aggregates.

differences are observed among six out of seven ¾-in. aggregates, showing consistent results of flatness ratio via FTI and manual measurements with a caliper, except for copper ore ¾-in. aggregates. The *t*-test result of copper ore ¾-in. aggregates indicates that the manually measured flatness ratio is slightly smaller than the results using FTI because the *t*-ratio is negative.

Figure 5-17 through Figure 5-23 plot the *t*-test results of flatness ratio for all the ¾-in. aggregates via FTI and manual measurements. However, for conciseness, the *t*-test results for the other aggregates are not listed in this report.

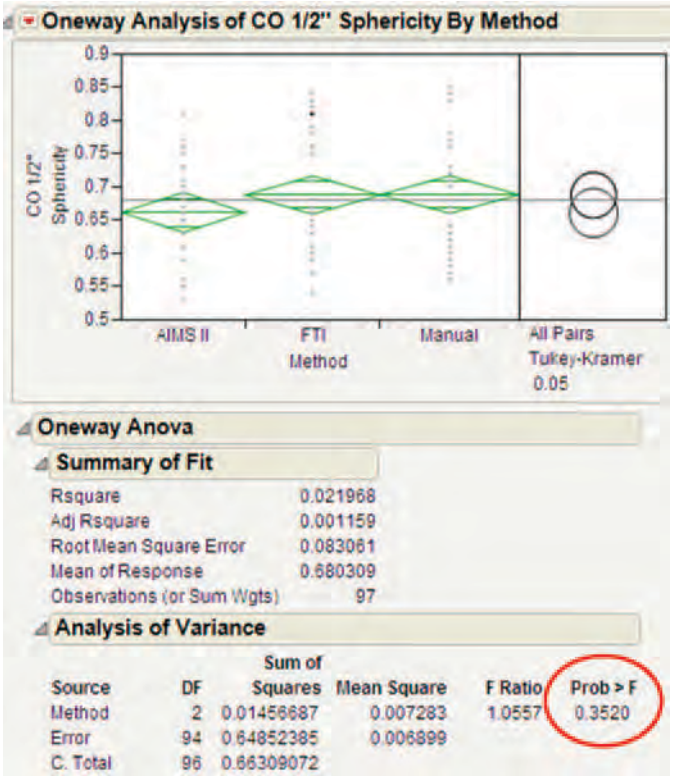

Note: Since p-value = 0.3520 > 0.05, fail to reject H_0. Therefore, there is no significant difference among the three means.

Figure 5-3. One-way ANOVA of sphericity for copper ore ½-in. aggregates.

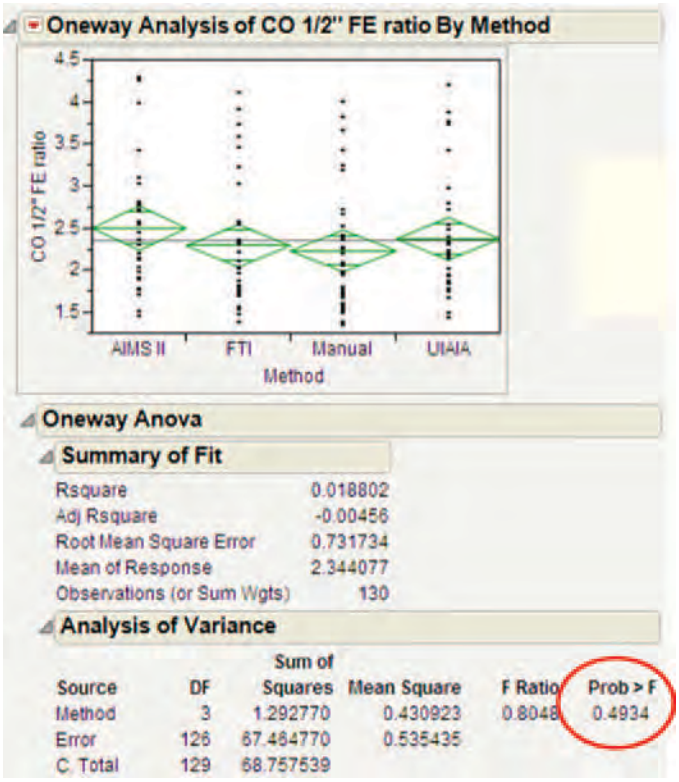

Note: Since p-value = 0.4934 > 0.05, fail to reject H_0. Therefore, there is insufficient sample evidence to support that there are significant differences among the four means.

Figure 5-4. One-way ANOVA of FE ratio for copper ore ½-in. aggregates.

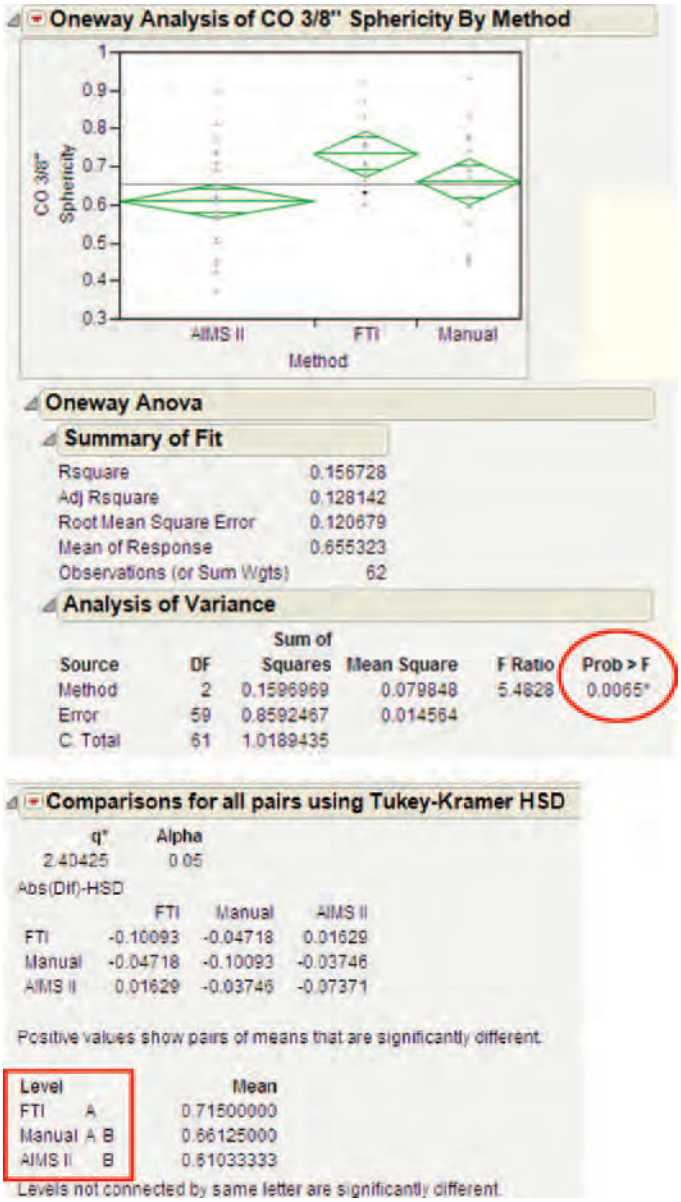

Note: Since p-value = 0.0065 < 0.05, reject H_0. Therefore, there is sufficient sample evidence to support that there are significant differences among the three methods. Tukey's HSD test suggests that the FTI mean is greater than the AIMS II and manual measurement means.

Figure 5-5. One-way ANOVA of sphericity for copper ore ⅜-in. aggregates.

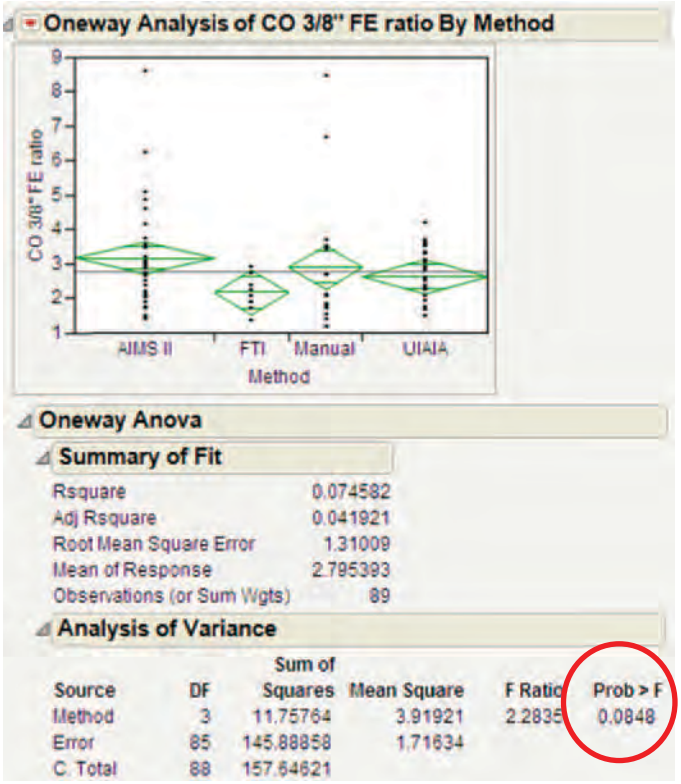

Note: Since p-value = 0.0848 > 0.05, fail to reject H_0. Therefore, there is insufficient sample evidence to support that there are significant differences among the four means.

Figure 5-6. One-way ANOVA of FE ratio for copper ore ⅜-in. aggregates.

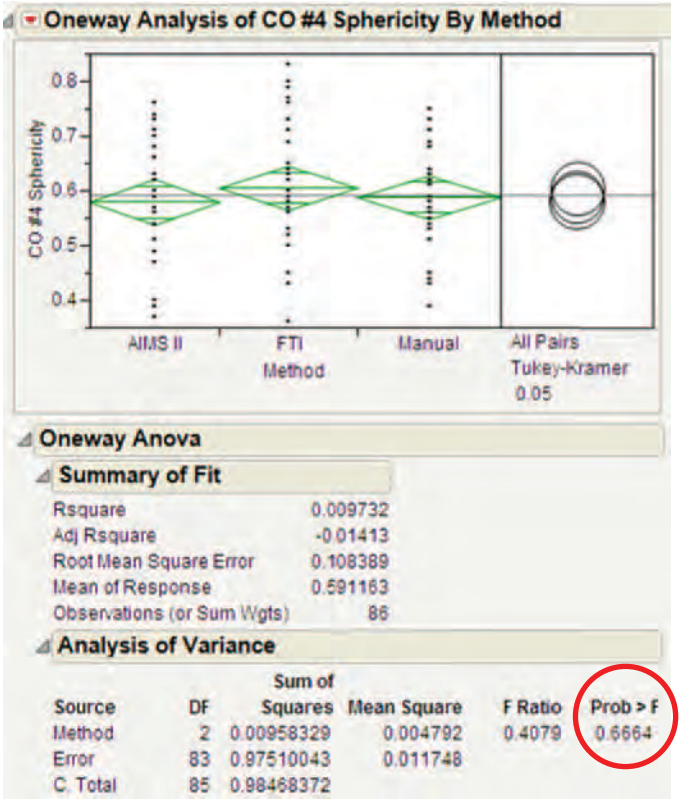

Note: Since *p*-value = 0.6664 > 0.05, fail to reject H_0. Therefore, there is no significant difference among the AIMS II, FTI, and manual means.

Figure 5-7. One-way ANOVA of sphericity for copper ore #4 aggregates.

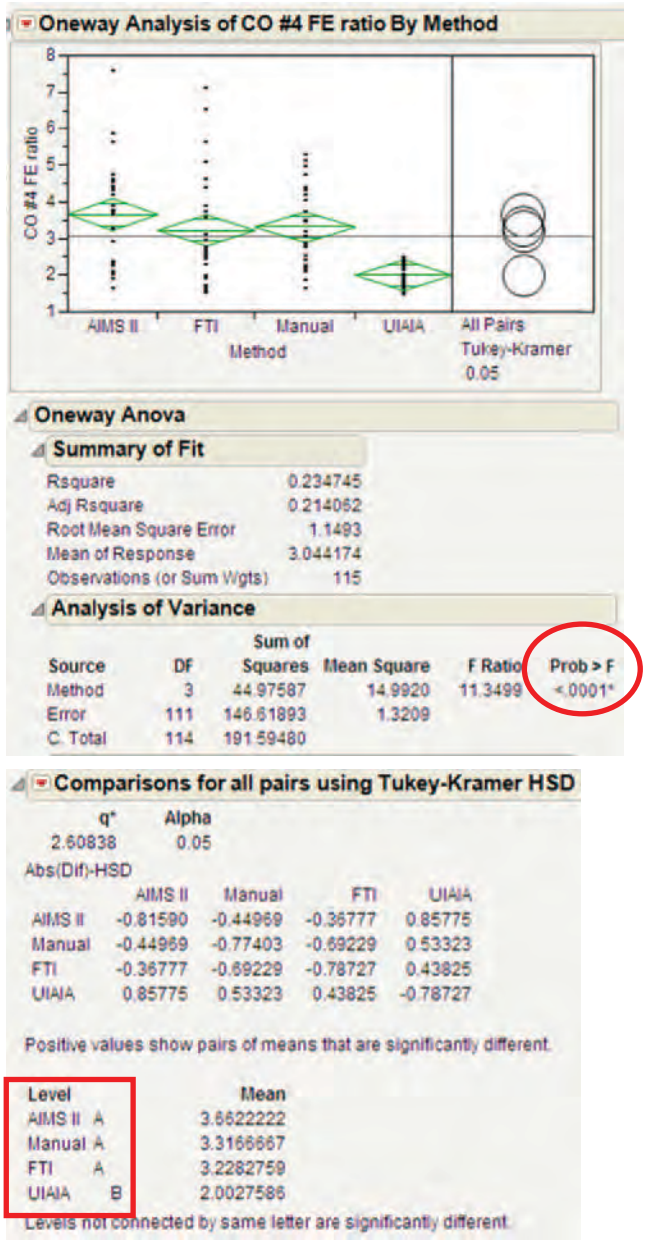

Note: Since *p*-value <0.0001 < 00.05, reject H_0. Therefore, there is sufficient sample evidence to support that there are significant differences among the four means. Tukey's HSD test suggests that the UIAIA mean is significantly smaller than the other three means.

Figure 5-8. One-way ANOVA of FE ratio for copper ore #4 aggregates.

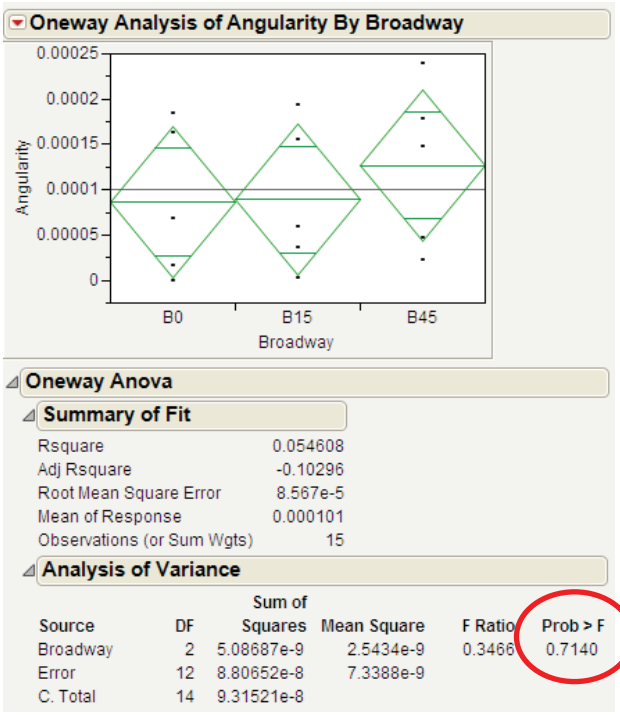

Note: Since *p*-value = 0.7140 > 0.05, fail to reject H_0. Therefore, there is insufficient sample evidence to suggest that there is significant difference of FTI angularity among the three groups (i.e., we cannot detect that the duration of the Micro-Deval test has an effect on the true mean of FTI angularity of the five Broadway aggregates).

Figure 5-9. One-way ANOVA of angularity for Broadway aggregates.

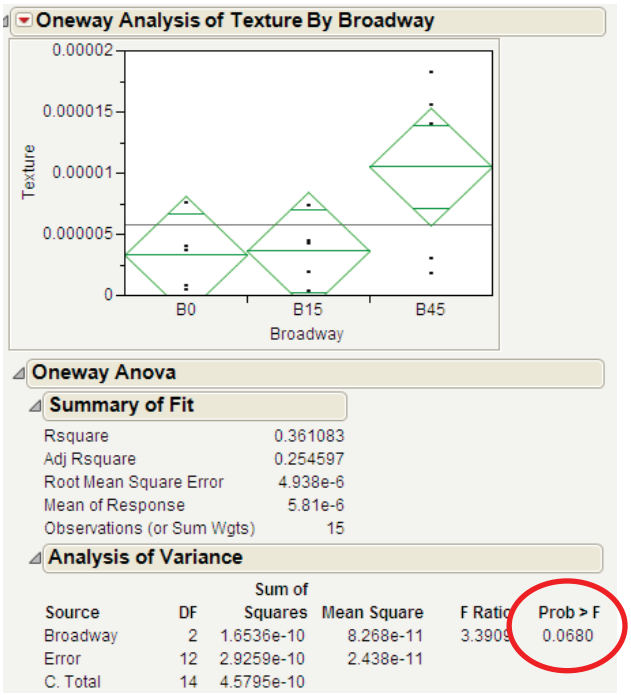

Note: Since *p*-value = 0.6800 > 0.05, fail to reject H_0. Therefore, there is insufficient sample evidence to suggest that there is significant difference of FTI texture among the three groups (i.e., we cannot detect that the duration of the Micro-Deval test has an effect on the true mean of FTI texture of the five Broadway aggregates).

Figure 5-10. One-way ANOVA of texture for Broadway aggregates.

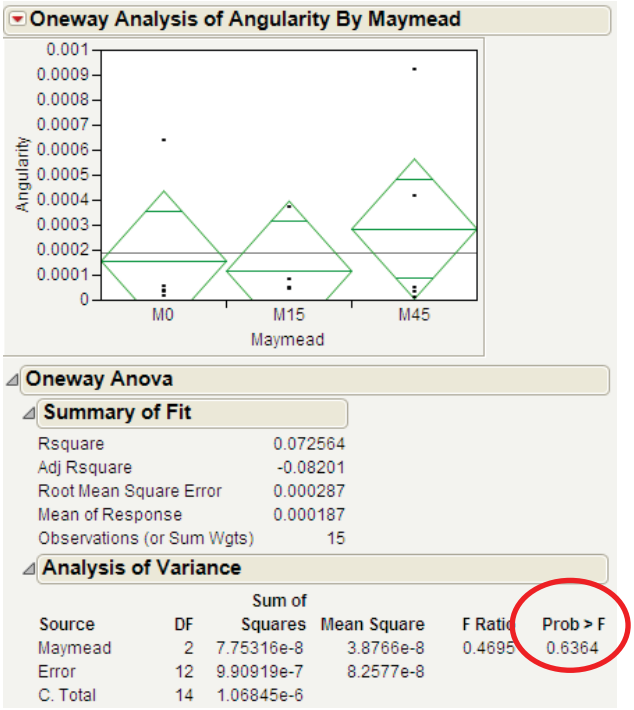

Note: Since *p*-value = 0.6364 > 0.05, fail to reject H_0. Therefore, there is insufficient sample evidence to suggest that there is significant difference of FTI angularity among the three groups (i.e., we cannot detect that the duration of the Micro-Deval test has an effect on the true mean of FTI angularity of the five Maymead aggregates).

Figure 5-11. One-way ANOVA of angularity for Maymead aggregates.

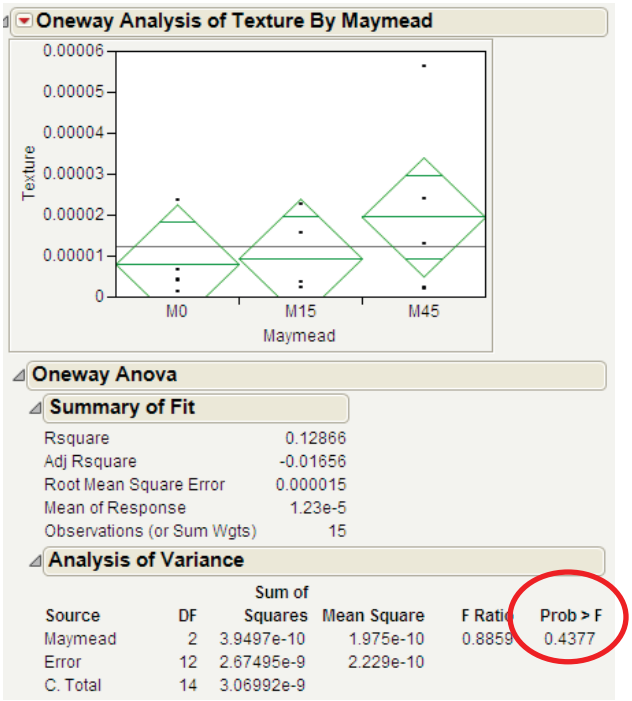

Note: Since *p*-value = 0.4377 > 0.05, fail to reject H_0. Therefore, there is insufficient sample evidence to suggest that there is significant difference of FTI texture among the three groups (i.e., we cannot detect that the duration of the Micro-Deval test has an effect on the true mean of FTI texture of the five Maymead aggregates).

Figure 5-12. One-way ANOVA of texture for Maymead aggregates.

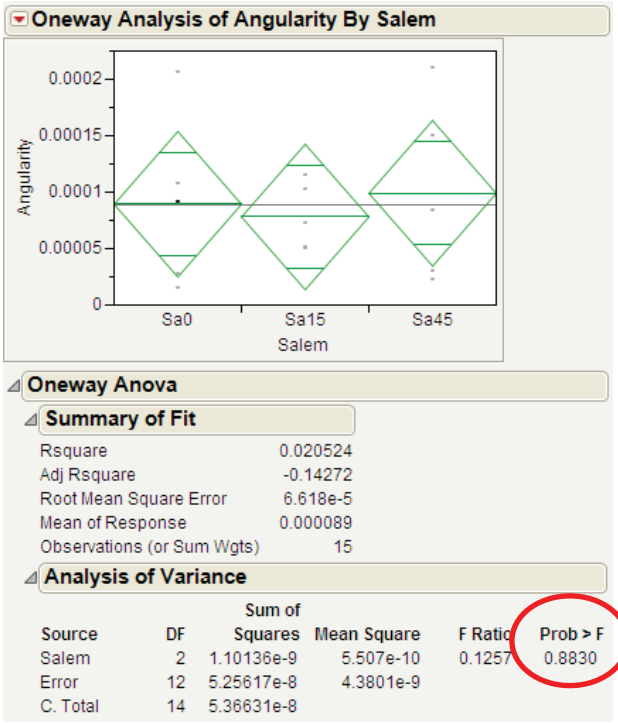

Note: Since *p*-value = 0.8830 > 0.05, fail to reject H_0. Therefore, there is insufficient sample evidence to suggest that there is significant difference of FTI angularity among the three groups (i.e., we cannot detect that the duration of the Micro-Deval test has an effect on the true mean of FTI angularity of the five Salem aggregates).

Figure 5-13. One-way ANOVA of angularity for Salem aggregates.

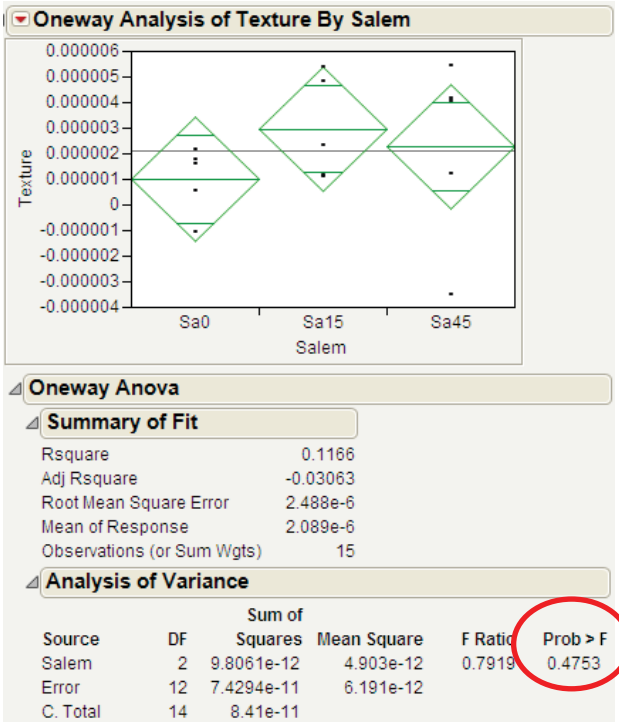

Note: Since *p*-value = 0.4753 > 0.05, fail to reject H_0. Therefore, there is insufficient sample evidence to suggest that there is significant difference of FTI texture among the three groups (i.e., we cannot detect that the duration of the Micro-Deval test has an effect on the true mean of FTI texture of the five Salem aggregates).

Figure 5-14. One-way ANOVA of texture for Salem aggregates.

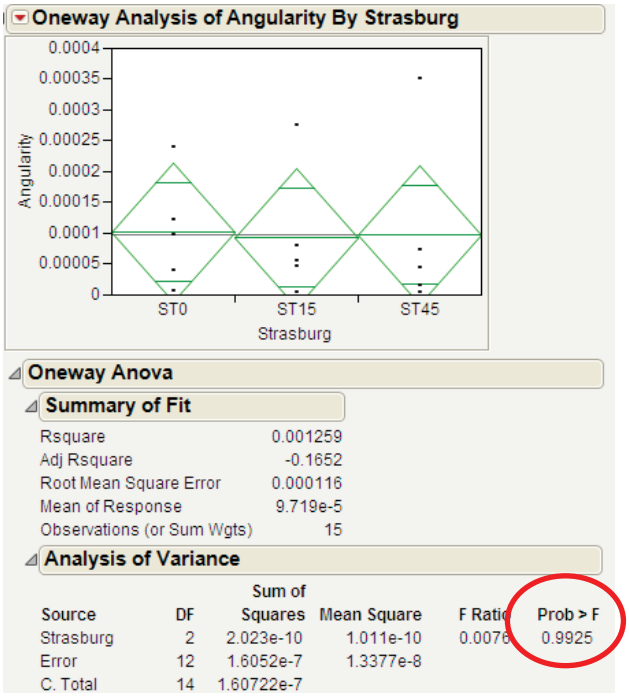

Note: Since p-value = 0.9925 > 0.05, fail to reject H_0. Therefore, there is insufficient sample evidence to suggest that there is significant difference of FTI angularity among the three groups (i.e., we cannot detect that the duration of the Micro-Deval test has an effect on the true mean of FTI angularity of the five Strasburg aggregates).

Figure 5-15. One-way ANOVA of angularity for Strasburg aggregates.

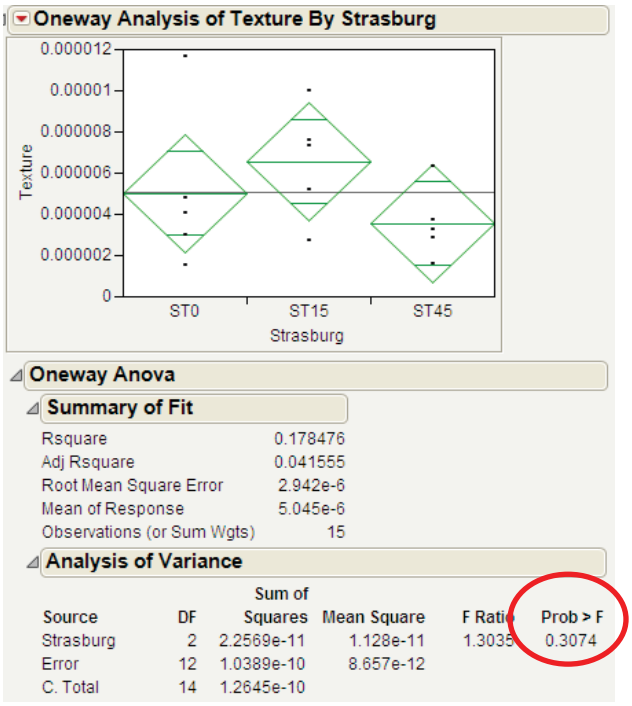

Note: Since p-value = 0.3074 > 0.05, fail to reject H_0. Therefore, there is insufficient sample evidence to suggest that there is significant difference of FTI texture among the three groups (i.e., we cannot detect that the duration of the Micro-Deval test has an effect on the true mean of FTI texture of the five Strasburg aggregates).

Figure 5-16. One-way ANOVA of texture for Strasburg aggregates.

Table 5-4. Unpaired *t*-test results of aggregates in Set 1.

α = 0.02				
3/4" Aggregates	***t*-ratio**	***p*-value**	**Statistical Result**	**Description**
BFS	5.1939	1.0000	Fail to reject H_0	No significant difference between the FTI and manual flatness ratios.
CO	-2.3407	0.0115	Reject H_0	Manual flatness ratio is smaller than the FTI flatness ratio.
DLT	-1.8715	0.0330	Fail to reject H_0	No significant difference between the FTI and manual flatness ratios.
GGC	-1.9938	0.0255	Fail to reject H_0	No significant difference between the FTI and manual flatness ratios.
GGR	0.3893	0.6507	Fail to reject H_0	No significant difference between the FTI and manual flatness ratios.
IO	-1.9983	0.0252	Fail to reject H_0	No significant difference between the FTI and manual flatness ratios.
LST	0.2025	0.5798	Fail to reject H_0	No significant difference between the FTI and manual flatness ratios.

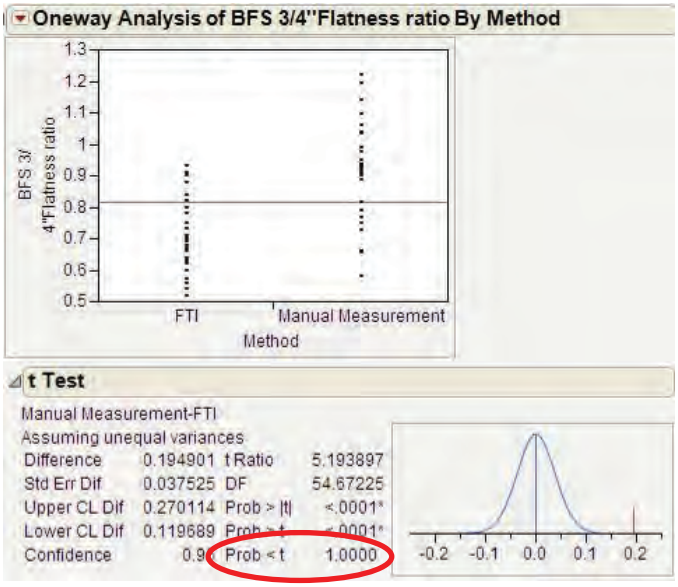

Note: Here *p*-value = 1.0000 > α = 0.02, fail to reject H_0. There is no difference between the FTI flatness ratio and the manually measured flatness ratio for blast furnace slag ¾-in. aggregates.

Figure 5-17. t-test of flatness ratio for blast furnace slag ¾-in. aggregates.

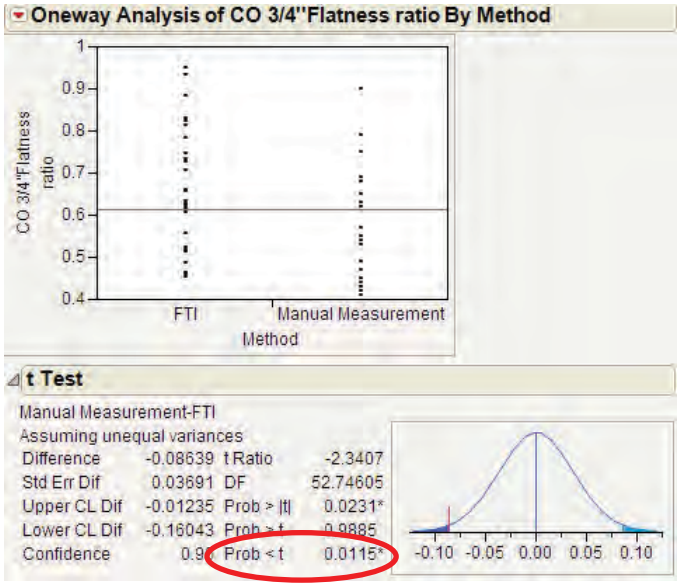

Note: Here *p*-value = 0.0115 < α = 0.02, reject H_0. There is a difference between the FTI flatness ratio and the manually measured flatness ratio for copper ore ¾-in. aggregates. As the *t*-ratio (-2.3407) is negative, the manually measured flatness ratio is smaller compared to the FTI flatness ratio.

Figure 5-18. t-test of flatness ratio for copper ore ¾-in. aggregates.

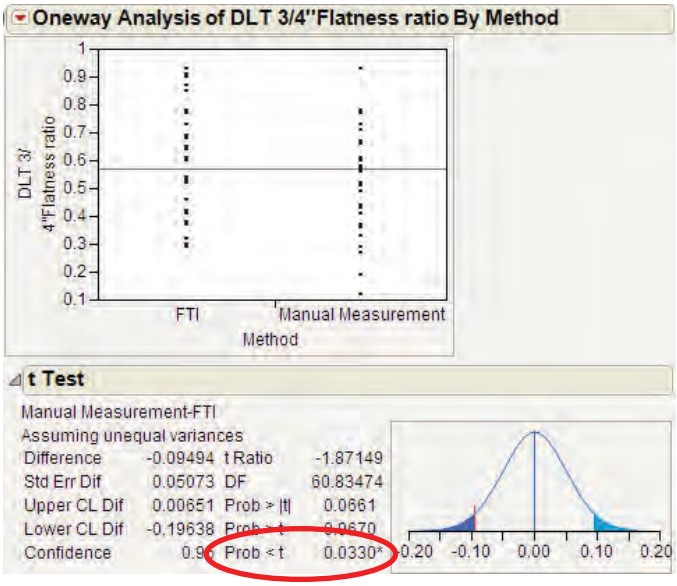

Note: Here *p*-value = 0.0330 > α = 0.02, fail to reject H_0. There is no difference between the FTI flatness ratio and the manually measured flatness ratio for dolomite ¾-in. aggregates.

Figure 5-19. t-test of flatness ratio for dolomite ¾-in. aggregates.

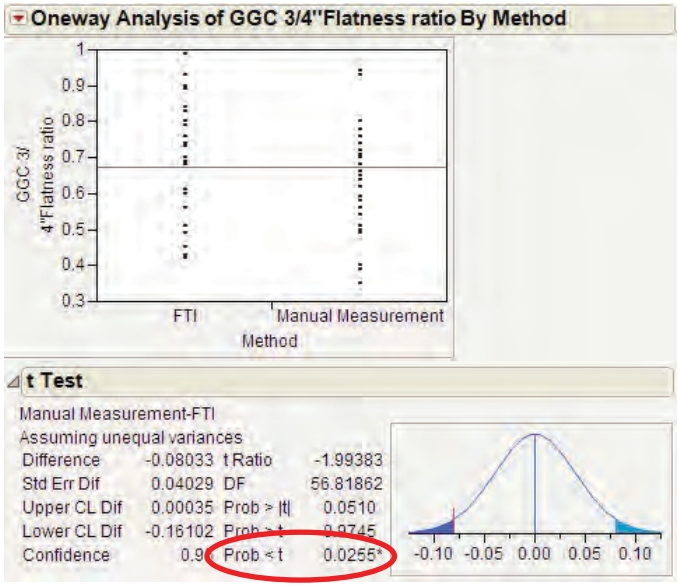

Note: Here *p*-value = 0.0255 > α = 0.02, fail to reject H_0. There is no difference between the FTI flatness ratio and the manually measured flatness ratio for crushed glacial gravel ¾-in. aggregates.

Figure 5-20. t-test of flatness ratio for crushed glacial gravel ¾-in. aggregates.

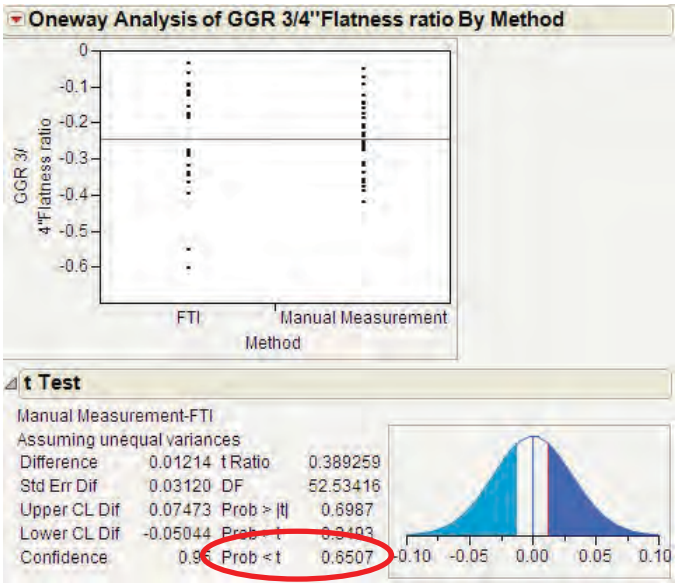

Note: Here p-value = 0.6507 > α = 0.02, fail to reject H_0. There is no difference between the FTI flatness ratio and the manually measured flatness ratio for rounded glacial gravel ¾-in. aggregates.

Figure 5-21. t-test of flatness ratio for rounded glacial gravel ¾-in. aggregates.

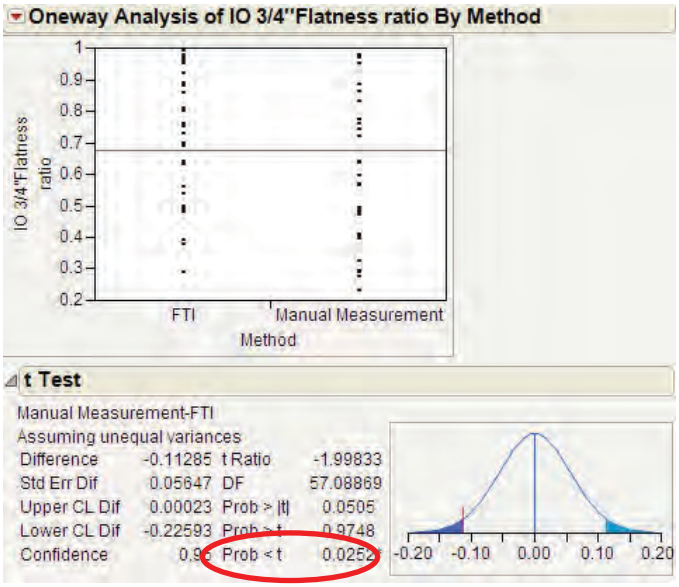

Note: Here p-value = 0.0252 > α = 0.02, fail to reject H_0. There is no difference between the FTI flatness ratio and the manually measured flatness ratio for iron ore ¾-in. aggregates.

Figure 5-22. t-test of flatness ratio for iron ore ¾-in. aggregates.

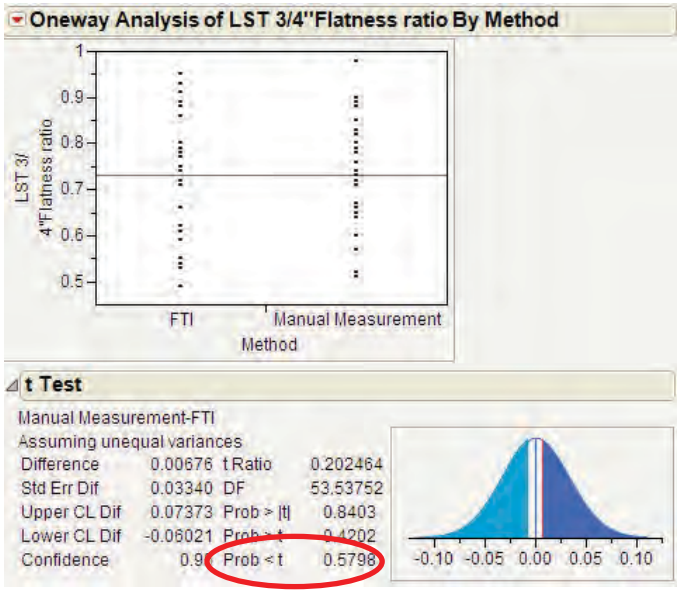

Note: Here p-value = 0.5798 > α = 0.02, fail to reject H_0. There is no difference between the FTI flatness ratio and manually measured flatness ratio for limestone ¾-in. aggregates.

Figure 5-23. t-test of flatness ratio for limestone ¾-in. aggregates.

CHAPTER 6

Discussion

In this chapter, comparisons of the aggregate dimensions using the FTI system and manual measurement will first be discussed for the coarse aggregates in Set 1. The relationship between the FTI calculated dimensions and the manually measured dimensions can be followed with a linear regression, indicating the accuracy of the FTI system. To verify the reliability of the FTI system, all the coarse aggregates in Set 1 are imaged and analyzed using the FTI, AIMS II, and UIAIA systems to compare the angularity and texture results. To evaluate the sensitivity of the FTI system, the abrasion effect of the Micro-Deval test on aggregates is detected by comparing the changes of angularity and texture before and after the Micro-Deval test for coarse aggregates in Set 2. Furthermore, fine aggregates are evaluated using both the FTI system and AIMS II system to discuss the reliability of the FTI system in the analysis of fine aggregates with the comparison of angularity rankings using both the FTI and AIMS II systems. After the validation of the capability of the FTI system to analyze both coarse and fine aggregates, the FTI analysis results of rounded glacial gravel aggregates and crushed glacial gravel aggregates are compared to assess the crushing effects on aggregates. In the end, the FTI system features are compared to those of the other aggregate imaging systems, such as AIMS II and UIAIA.

6.1 Comparison Between the FTI Results and Manual Measurements

Figure 6-1 through Figure 6-4 present the relationship between the sphericity obtained by the FTI system and the sphericity calculated from manually measured dimensions (hereinafter referred to as manually measured sphericity) for ¾-in., ½-in., ⅜-in., and #4 aggregates in Set 1, respectively. The manually measured sphericity is labeled *x,* and the sphericity acquired from the FTI system is labeled *y* for the same aggregate particle. The relationship between *x* and *y* is obtained through linear regressions. Similar linear relationships can also be found between the results by FTI and those via manual measurements for flatness ratio, elongation ratio, and FE ratio. The good agreement between the FTI results and the manually measured results has validated the capability of the FTI system to characterize the shape of aggregates.

6.2 Angularity and Texture Comparison of the FTI Results to AIMS II and UIAIA Results

To further evaluate the soundness of the FTI system, all the ¾-in. aggregate particles of the seven types of aggregate were also assessed using AIMS II and UIAIA. Appendix F presents the photographs of the ¾-in. aggregates. Via visual judgment, one can observe that blast furnace slag has very angular and the roughest surfaces, and that rounded glacial gravel is the least angular and has very smooth surfaces.

Table 6-1 shows the angularity and texture rankings according to the mean values of the FTI, AIMS II, and UIAIA angularity and texture measurements of aggregates in Set 1. In general, blast furnace slag aggregates are the most angular, with rougher surfaces among the seven types of aggregate; rounded glacial gravel aggregates were found to have the smoothest surfaces. Further details can be found in Table 6-2 through Table 6-5.

In terms of FTI results, both blast furnace slag and copper ore have large values for angularity and texture for the ¾-in. aggregates, indicating angular aggregates with very rough surfaces. Conversely, compared with other aggregates, rounded glacial gravel, iron ore, and limestone have smooth surfaces with smaller angularity. Of the ½-in. aggregates, blast furnace slag and crushed glacial gravel aggregates are the most angular, whereas rounded glacial gravel and dolomite are the least angular. In terms of texture, blast furnace slag and copper ore are the roughest aggregates, and rounded glacial gravel aggregates are the smoothest. For ⅜-in. aggregates, iron ore is the most angular aggregate instead of blast furnace slag. Of the #4 aggregates, copper ore is the most angular with

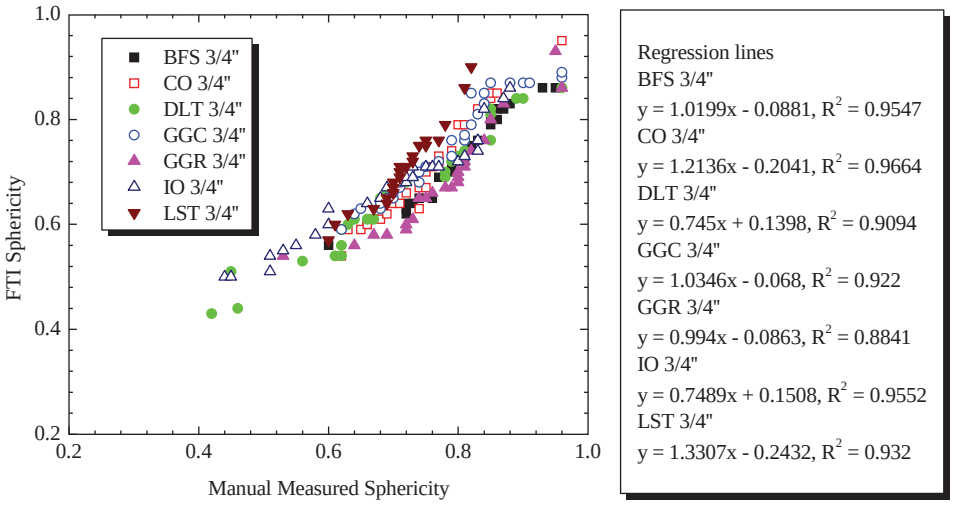

Figure 6-1. FTI sphericity versus manually measured sphericity for ¾-in. aggregates.

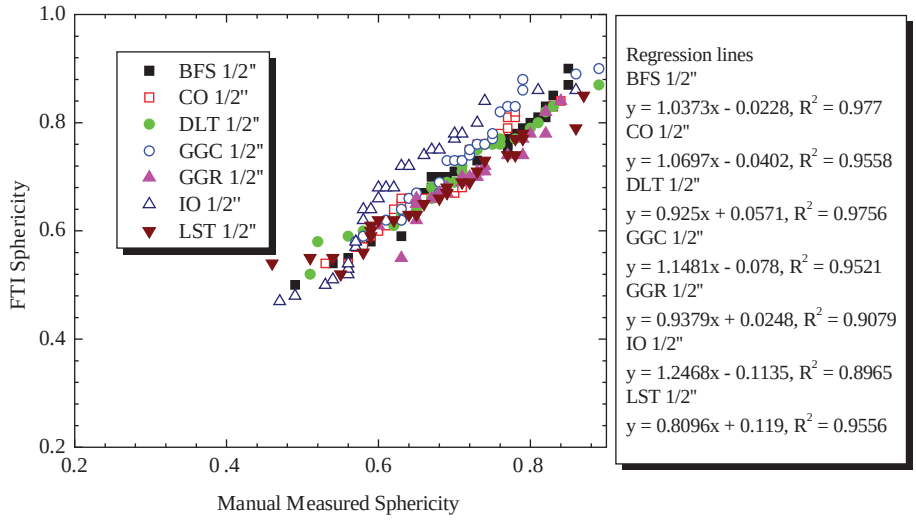

Figure 6-2. FTI sphericity versus manually measured sphericity for ½-in. aggregates.

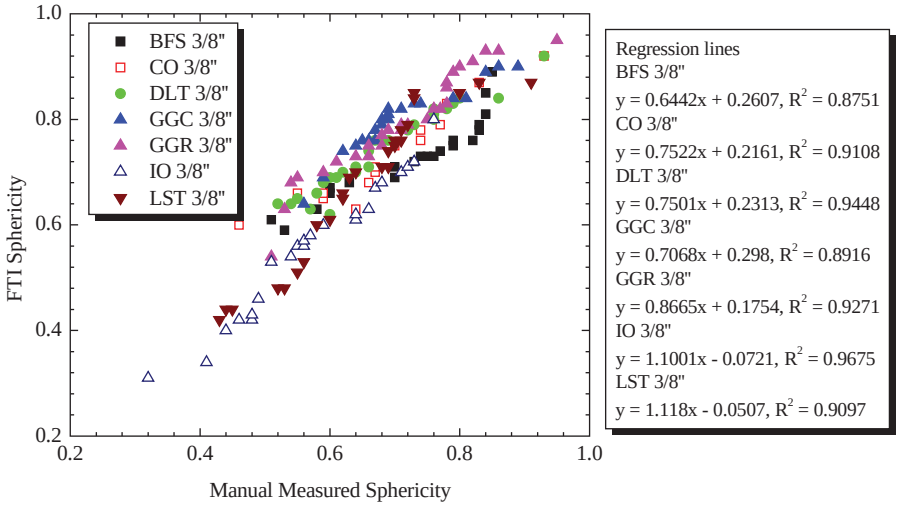

Figure 6-3. FTI sphericity versus manually measured sphericity for ⅜-in. aggregates.

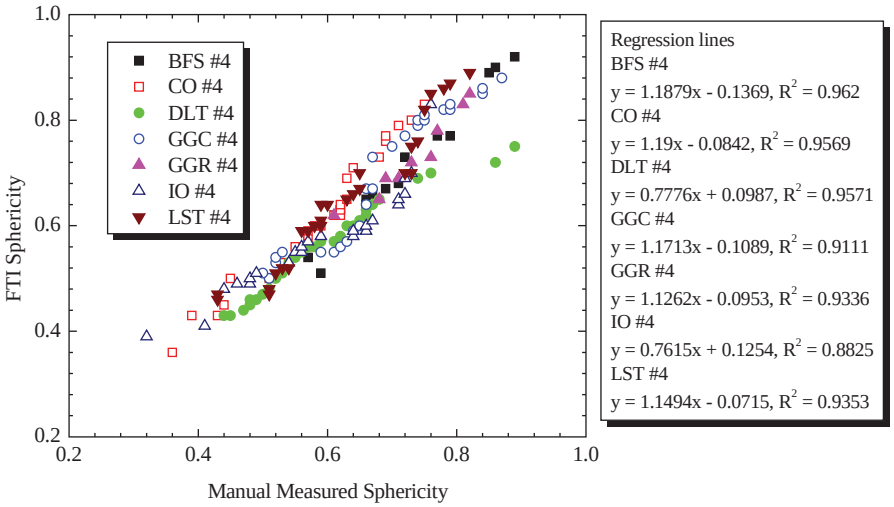

Figure 6-4. FTI sphericity versus manually measured sphericity for #4 aggregates.

Table 6-1. Roughness ranking results in the FTI, AIMS II, and UIAIA systems.

Aggregate Size	3/4"		1/2"		3/8"		#4		Roughness Ranking
Morphological Characteristics	Ang	Tex	Ang	Tex	Ang	Tex	Ang	Tex	
FTI	BFS	BFS	BFS	BFS	IO	IO	CO	CO	Rough
	CO	CO	GGC	CO	LST	LST	IO	LST	
	GGC	DLT	LST	DLT	BFS	BFS	BFS	DLT	
	DLT	GGC	IO	GGC	GGC	GGC	DLT	IO	↓
	IO	LST	CO	IO	CO	GGR	LST	BFS	
	LST	IO	GGR	LST	GGR	CO	GGC	GGR	
	GGR	GGR	DLT	GGR	DLT	DLT	GGR	GGC	Smooth
AIMS II	CO	CO	IO	BFS	CO	BFS	CO	BFS	Rough
	IO	IO	BFS	CO	IO	DLT	IO	CO	
	BFS	DLT	CO	GGC	BFS	LST	LST	LST	
	DLT	BFS	LST	LST	LST	CO	GGC	GGC	↓
	LST	LST	DLT	DLT	DLT	IO	BFS	IO	
	GGC	GGC	GGC	IO	GGC	GGC	DLT	DLT	
	GGR	GGR	GGR	GGR	GGR	GGR	GGR	GGR	Smooth
UIAIA*	GGC	GGC	GGC	GGC	GGC	GGC	BFS	CO	Rough
	BFS	BFS	CO	CO	CO	CO	CO	GGR	
	CO	DLT	LST	BFS	BFS	DLT	GGR	GGC	↓
	LST	GGR	BFS	DLT	LST	LST	LST	DLT	
	DLT	CO	DLT	LST	DLT	GGR	DLT	LST	
	GGR	LST	GGR	GGR	GGR	BFS	GGC	BFS	Smooth

*UIAIA is incapable of analyzing iron ore aggregates because the color of iron ore aggregates is very similar to the background color of the UIAIA conveyor.

Note: Ang = Angularity; Tex = Texture; BFS = Blast furnace slag; CO = Copper ore; DLT = Dolomite; GGC = Glacial gravel – crushed; GGR = Glacial gravel – rounded; IO = Iron ore; LST = Limestone.

Table 6-2. Angularity and texture using FTI, AIMS II, and UIAIA for ¾-in. aggregates.

3/4" Aggregates			Blast Furnace Slag	Copper Ore	Dolomite	Glacial Gravel – Crushed	Glacial Gravel – Rounded	Iron Ore	Limestone
Angularity	FTI	Mean	2.74×10^{-4}	2.69×10^{-4}	1.58×10^{-4}	2.31×10^{-4}	0.84×10^{-4}	1.01×10^{-4}	0.99×10^{-4}
		Standard deviation	6.59×10^{-4}	4.52×10^{-4}	3.07×10^{-4}	4.25×10^{-4}	1.13×10^{-4}	1.12×10^{-4}	1.39×10^{-4}
	AIMS II	Mean	2968.15	3138.48	2689.25	2590.37	1532.39	3160.48	2757.89
		Standard deviation	930.95	625.82	690.57	736.76	660.06	722.55	761.4
	UIAIA	Mean	439.24	373.62	337.34	486.73	254.01	–	348.93
		Standard deviation	115	76.26	62.38	110.12	84.35	–	59.11
Texture	FTI	Mean	6.38×10^{-6}	4.97×10^{-6}	3.90×10^{-6}	3.86×10^{-6}	1.60×10^{-6}	2.13×10^{-6}	2.52×10^{-6}
		Standard deviation	6.28×10^{-6}	4.49×10^{-6}	3.93×10^{-6}	5.54×10^{-6}	1.66×10^{-6}	1.93×10^{-6}	2.74×10^{-6}
	AIMS II	Mean	503.65	334.79	254.41	379.34	161.95	201.34	294.77
		Standard deviation	181.8	118.19	117.84	152.53	97.89	80.18	103.36
	UIAIA	Mean	1.69	0.95	1.09	2.09	0.98	–	0.82
		Standard deviation	1.18	0.28	0.84	0.73	0.55	–	0.25

Table 6-3. Angularity and texture using FTI, AIMS II, and UIAIA for ½-in. aggregates.

1/2" Aggregates			Blast Furnace Slag	Copper Ore	Dolomite	Glacial Gravel – Crushed	Glacial Gravel – Rounded	Iron Ore	Limestone
Angularity	FTI	Mean	2.44×10^{-4}	0.98×10^{-4}	0.60×10^{-4}	1.46×10^{-4}	0.97×10^{-4}	1.00×10^{-4}	1.90×10^{-4}
		Standard deviation	5.18×10^{-4}	1.14×10^{-4}	1.13×10^{-4}	2.51×10^{-4}	1.11×10^{-4}	1.04×10^{-4}	4.54×10^{-4}
	AIMS II	Mean	3040.72	3126.44	2864.42	2650.92	1362.78	2932.80	2859.35
		Standard deviation	833.09	604.35	697.83	612.77	624.87	515.95	631.80
	UIAIA	Mean	367.51	394.23	333.59	458.09	239.89	–	357.07
		Standard deviation	80.71	77	55.15	108.54	83.19	–	51.69
Texture	FTI	Mean	9.57×10^{-6}	4.69×10^{-6}	2.86×10^{-6}	2.70×10^{-6}	3.54×10^{-6}	5.17×10^{-6}	4.60×10^{-6}
		Standard deviation	13.70×10^{-6}	5.68×10^{-6}	5.18×10^{-6}	3.37×10^{-6}	4.32×10^{-6}	6.47×10^{-6}	8.38×10^{-6}
	AIMS II	Mean	574.74	365.75	259.11	322.72	217.55	243.40	270.21
		Standard deviation	155.81	120.04	113.33	188.26	145.06	112.90	122.26
	UIAIA	Mean	1.12	1.19	0.92	2.15	1.00	–	0.91
		Standard deviation	0.39	0.44	0.39	0.98	0.76	–	0.27

Table 6-4. Angularity and texture using FTI, AIMS II, and UIAIA for ⅜-in. aggregates.

3/8" Aggregates			Blast Furnace Slag	Copper Ore	Dolomite	Glacial Gravel – Crushed	Glacial Gravel – Rounded	Iron Ore	Limestone
Angularity	FTI	Mean	2.19×10^{-4}	0.75×10^{-4}	0.87×10^{-4}	1.47×10^{-4}	1.09×10^{-4}	10.9×10^{-4}	3.32×10^{-4}
		Standard deviation	4.48×10^{-4}	1.09×10^{-4}	0.97×10^{-4}	1.98×10^{-4}	1.94×10^{-4}	23.6×10^{-4}	6.33×10^{-4}
	AIMS II	Mean	3005.16	3276.11	2675.33	2621.36	1294.42	1625.2	2745.29
		Standard deviation	551.28	815.64	632.1	756.18	839.81	625.31	559.12
	UIAIA	Mean	339.55	359.97	324.19	447.43	258.84	–	343.73
		Standard deviation	51.31	78.38	59.69	85.5	92.44	–	50.22
Texture	FTI	Mean	9.48×10^{-6}	3.84×10^{-6}	3.59×10^{-6}	6.94×10^{-6}	4.81×10^{-6}	80.3×10^{-6}	15.9×10^{-6}
		Standard deviation	11.8×10^{-6}	6.19×10^{-6}	3.92×10^{-6}	10.0×10^{-6}	15.5×10^{-6}	304.0×10^{-6}	32.6×10^{-6}
	AIMS II	Mean	538.94	339.83	239.18	273.31	169.35	154.43	258.47
		Standard deviation	137.83	113.31	100.19	140.35	82.29	123.2	100.65
	UIAIA	Mean	0.86	1.42	1.14	1.66	0.92	–	0.95
		Standard deviation	0.27	0.67	0.46	0.69	0.53	–	0.39

Table 6-5. Angularity and texture using FTI, AIMS II, and UIAIA for # 4 aggregates.

#4 Aggregates			Blast Furnace Slag	Copper Ore	Dolomite	Glacial Gravel – Crushed	Glacial Gavel – Rounded	Iron Ore	Limestone
Angularity	FTI	Mean	14.7×10^{-4}	42.5×10^{-4}	15.7×10^{-4}	2.48×10^{-4}	2.48×10^{-4}	21.6×10^{-4}	12.5×10^{-4}
		Standard deviation	49.9×10^{-4}	74.4×10^{-4}	20.5×10^{-4}	2.66×10^{-4}	2.04×10^{-4}	29.6×10^{-4}	20.6×10^{-4}
	AIMS II	Mean	3336.79	3450.46	2920.58	3023.80	1563.85	3183.12	2999.47
		Standard deviation	897.00	809.55	710.91	661.65	1134.25	627.50	525.94
	UIAIA	Mean	400.65	407.43	325.72	483.91	359.51	–	335.80
		Standard deviation	82.65	76.82	56.16	93.24	110.88	–	60.30
Texture	FTI	Mean	60×10^{-6}	190×10^{-6}	82.3×10^{-6}	9.33×10^{-6}	14.4×10^{-6}	74.2×10^{-6}	91.8×10^{-6}
		Standard deviation	149×10^{-6}	512×10^{-6}	224×10^{-6}	16.4×10^{-6}	15.4×10^{-6}	86.3×10^{-6}	203×10^{-6}
	AIMS II	Mean	491.31	331.60	159.75	240.34	132.07	208.52	290.37
		Standard deviation	130.03	77.46	66.15	135.65	109.45	75.86	116.40
	UIAIA	Mean	0.97	1.66	1.22	2.24	1.35	–	1.16
		Standard deviation	0.33	0.81	0.77	1.07	0.95	–	0.67

the roughest surfaces, whereas crushed glacial gravel and rounded glacial gravel are less angular aggregates with the smoothest surfaces.

In terms of the AIMS II results, rounded glacial gravel aggregates have the smallest angularity index, corresponding to the smoothest surfaces with least angularity, of all the aggregates. For the ¾-in. aggregates, copper ore is the most angular with the roughest surfaces, followed by iron ore; rounded glacial gravel is the least angular with the smoothest surfaces, followed by crushed glacial gravel and limestone. For ½-in. aggregates, iron ore aggregates are the most angular, followed by blast furnace slag and copper ore, whereas iron ore has very smooth surfaces in terms of texture. For ⅜-in. aggregates, copper ore is the most angular with intermediate surface texture, and blast furnace slag is the third most angular with the roughest surfaces. Among #4 aggregates, copper ore has the greatest value of angularity with the second roughest surfaces, and blast furnace slag is much less angular with the roughest surfaces.

The UIAIA is incapable of imaging iron ore aggregates because the color of iron ore aggregates is very similar to the background color of the UIAIA conveyor. Therefore, there is no result for iron ore by UIAIA. By UIAIA, among all the ¾-in., ½-in., and ⅜-in. aggregates, crushed glacial gravel is the most angular with the roughest surfaces, followed by either blast furnace slag or copper ore; rounded glacial gravel is the least angular aggregate. For #4 aggregates, blast furnace slag is the most angular with the smoothest surfaces. Copper ore is the second most angular, with the roughest surfaces.

Table 6-2 shows the mean values and the standard deviations for the seven aggregates using the FTI, AIMS II, and UIAIA systems. Regardless of the different definitions of morphological descriptors, the results from the three aggregate imaging systems indicate that blast furnace slag has very angular and rough surfaces and that rounded glacial gravel has the least angular and smooth surfaces. For ¾-in. aggregates, the average FTI angularity indices of blast furnace slag and copper ore are 2.74×10^{-4} and 2.69×10^{-4}, respectively; the average FTI texture index is 6.38×10^{-6} for blast furnace slag and 4.97×10^{-6} for copper ore. Both blast furnace slag and copper ore have large values of angularity and texture, indicating angular and rough surfaces, followed by crushed glacial gravel and dolomite. Conversely, rounded glacial gravel, iron ore, and limestone have smooth surfaces with less angularity compared to the other aggregates.

From the AIMS II results for ¾-in. aggregates, rounded glacial gravel has the smallest values of angularity (1532.29) and texture (161.95), indicating the smoothest surfaces with the least angularity. Copper ore has the most angular and roughest surface, followed by iron ore; rounded glacial gravel has the least angular and the smoothest surface, followed by crushed glacial gravel and limestone.

Iron ore aggregates cannot be imaged in UIAIA because the color of iron ore aggregates is very similar to the color of the UIAIA conveyor. Of the ¾-in. aggregates assessed, crushed glacial gravel is the most angular and has the roughest surfaces, followed by blast furnace slag, which is inconsistent with the rankings based on the results by FTI and AIMS II.

Since it is impossible to compare results of different methods due to their different definitions, relative rankings may provide a convenient comparison. Figure 6-5 plots the angularity and texture rankings for the ¾-in. aggregates. All the data in this figure are generated from Table 6-2 by dividing the mean value of each category (aggregate type and method, total of $4 \times 7 - 1 = 27$ combinations; iron ore cannot be imaged by UIAIA system) by the smallest mean of either angularity or texture in that category. For example, the FTI angularity ranking for BFS ¾-in. aggregates is 3.262, dividing the mean value of the BFS FTI angularity 2.74×10^{-4} by the minimum mean value of the FTI angularity among seven types of ¾-in. aggregates, which is 0.84×10^{-4}. As shown in Figure 6-5, the FTI, AIMS II, and UIAIA roughness rankings are consistent in that the rounded glacial gravel aggregates are the least angular and smooth, and the BFS aggregates are very angular and rough. The roughness rankings by these methods are typically consistent with visual judgments from the photographs in Appendix E.

Table 6-3 shows the mean values and standard deviations for seven types of ½-in. aggregates. Using the same angularity and texture ranking method, the angularity and texture rankings for ½-in. aggregates are plotted in Figure 6-6 based on the mean values in Table 6-3. According to the FTI ranking, blast furnace slag aggregates are the most angular, with

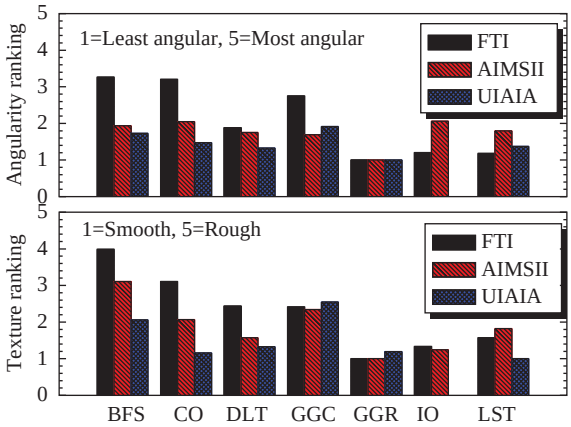

Note: BFS=Blast furnace slag; CO=Copper ore; DLT=Dolomite; GGC=Glacial gravel crushed; GGR=Glacial gravel rounded; IO=Iron ore; LST=limestone.

Figure 6-5. Roughness ranking of ¾-in. aggregates using the FTI, AIMS II, and UIAIA systems.

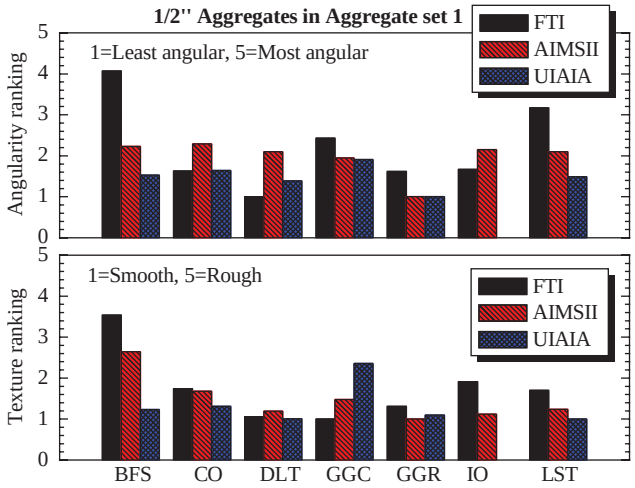

Note: BFS=Blast furnace slag; CO=Copper ore; DLT=Dolomite; GGC=Glacial gravel crushed; GGR=Glacial gravel rounded; IO=Iron ore; LST=Limestone.

Figure 6-6. Roughness ranking of ½-in. aggregates using the FTI, AIMS II, and UIAIA systems.

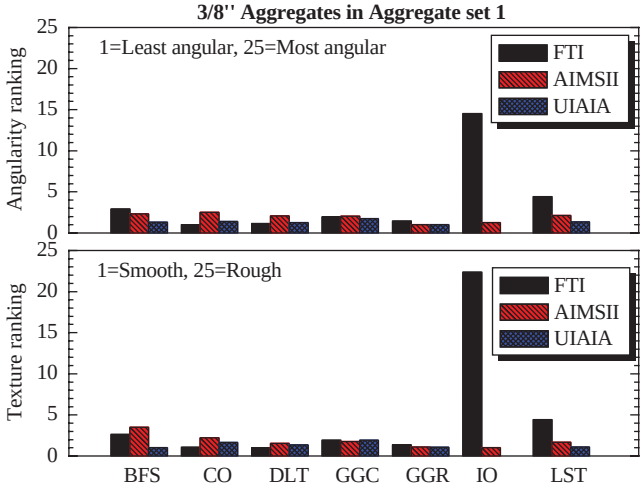

Note: BFS=Blast furnace slag; CO=Copper ore; DLT=Dolomite; GGC=Glacial gravel crushed; GGR=Glacial gravel rounded; IO=Iron ore; LST=Limestone.

Figure 6-7. Roughness ranking of ⅜-in. aggregates using the FTI, AIMS II, and UIAIA systems.

the roughest surfaces, followed by crushed glacial gravel as the second most angular and the fourth roughest surfaces. Rounded glacial gravel is the second least angular aggregate with the smoothest surfaces. According to the AIMS II ranking, copper ore is the most angular with the second roughest surfaces, followed by blast furnace slag as the second most angular with the roughest surfaces. Rounded glacial gravel is the least angular with the smoothest surfaces. In the UIAIA ranking, rounded glacial gravel aggregates are the second most angular with the smoothest surfaces, and crushed glacial gravel is the most angular with the roughest surfaces.

Table 6-4 and Table 6-5 show the mean values and standard deviations for the seven ⅜-in. and #4 aggregates. Figure 6-7 and Figure 6-8 plot the roughness rankings of these aggregates using the results of the FTI, AIMS II, and UIAIA systems.

The three aggregate imaging techniques are in agreement that blast furnace slag, crushed glacial gravel, and copper ore are very angular aggregates with very rough surfaces, and rounded glacial gravel aggregates are the least angular with the smoothest surfaces. Obviously the three image analysis techniques could not give the same rankings of angularity and texture. Possible reasons include: (1) different definitions of angularity and texture by the three techniques, and (2) different image resolutions in the three aggregate imaging systems. An advantage of using the FTI system is that it reconstructs the real 3-D coordinates of aggregate surfaces and performs morphological characterization based on the real 3-D coordinates, which makes it possible to assess the real 3-D morphological characteristics of the aggregates.

6.3 Assessments of Sensitivity of Angularity and Texture Change

The FTI system was used to measure the angularity and texture of 20 coarse aggregates in Set 2 before and after the Micro-Deval test to assess the sensitivity of the FTI system to detect changes in the morphological characteristics of the aggregates due to abrasion. The changes of FTI angularity and texture are shown in Figure 6-9. In this figure, the percentage change denotes the difference in either angularity

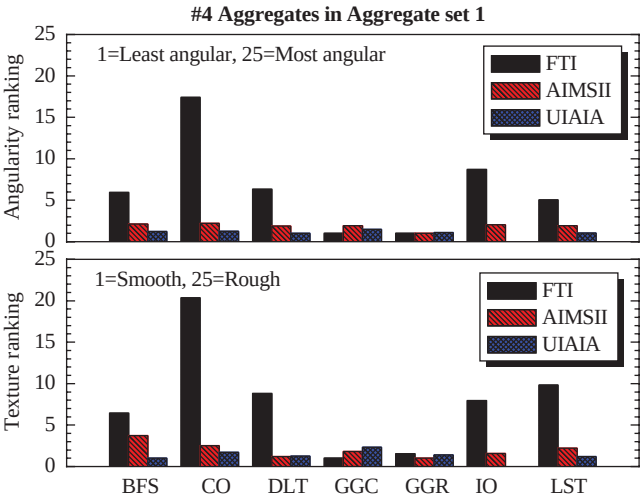

Note: BFS=Blast furnace slag; CO=Copper ore; DLT=Dolomite; GGC=Glacial gravel crushed; GGR=Glacial gravel rounded; IO=Iron ore; LST=Limestone.

Figure 6-8. Roughness ranking of #4 aggregates using the FTI, AIMS II, and UIAIA systems.

or texture of an aggregate before and after the Micro-Deval test, divided by the angularity and texture of the aggregates before testing.

Figure 6-9(a) shows the change of both angularity and texture after the Micro-Deval test for 15 min. A negative change in angularity indicates that an aggregate became less angular after the Micro-Deval test. A positive change in texture means that the aggregates became rougher. Strasburg experiences the greatest change compared to the other three types of aggregate. The general trend shown in this figure is that most of the aggregates become less angular, as expected. However, there is an increase in angularity for Broadway aggregates. Possible reasons could be that the Micro-Deval test causes some breakage in this type of aggregate, resulting in larger angularity. The increase in texture could be due to the increase of textured surfaces when aggregates were crushed.

Figure 6-9(b) shows the change in both angularity and texture after the Micro-Deval test for 45 min. Different from results after Micro-Deval testing for 15 min., three of the four types of aggregate become more angular, denoted by a positive change in angularity. Both Maymead and Salem aggregates experienced more than a 60% increase in angularity, indicating that aggregate particles experienced breakage. Conversely, the Strasburg aggregate exhibits about a 5% decrease in angularity, which is most likely attributed to the abrasion of the sharp corners of the surfaces. The decrease in angularity may be interpreted as that the loss of angular elements is larger than the angular elements produced by breakage due to abrasion. In terms of texture, there are dramatic increases for Broadway, Maymead, and Salem aggregates. However, Strasburg aggregates experienced a 28% decrease in texture due to abrasion in the Micro-Deval test for 45 min. The results show the inconsistency in change of angularity and texture as indicated by other tests.

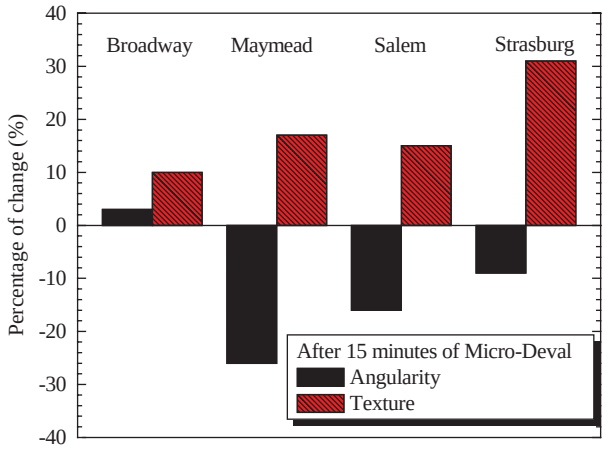

(a) After the Micro-Deval test for 15 min.

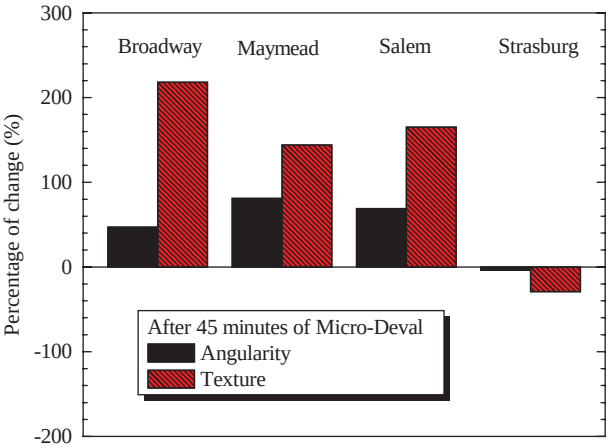

(b) After the Micro-Deval test for 45 min.

Figure 6-9. FTI results change.

The changes of FTI angularity and texture mean values during the Micro-Deval test process indicate that the Micro-Deval test might change the angularity and texture properties of aggregates. However, it is suggested to analyze more aggregates to reach a persuasive conclusion, since the ANOVA test suggests that the sample population of coarse aggregates in Set 2 is not large enough to indicate that the duration of the Micro-Deval test has an effect on the FTI angularity and texture (Section 5.1.2).

6.4 Comparison of Angularity for Fine Aggregates Between the FTI and AIMS II Results

To evaluate the capability of the FTI system to analyze fine aggregates, two types of fine aggregates are imaged and compared to the AIMS II angularity results: fine aggregates passing on a #4 sieve and retaining on a #8 sieve (hereinafter referred to as #8 aggregates), and fine aggregates passing on a #8 sieve and retaining on a #16 sieve (hereinafter referred to as #16 aggregates). There are six types of #8 aggregate and five types of #16 aggregate. All the fine aggregates have the same origins and physical properties as the corresponding types of coarse aggregate in Set 1 (Table 4-4). More than 100 fine aggregates are analyzed for each aggregate size.

It is worth noting that the morphological properties to describe morphological characteristics of fine aggregates in the FTI system include sphericity, flatness ratio, elongation ratio, and angularity. The value of sphericity ranges from 0 to 1; a sphericity value of 1 indicates a particle with equal dimensions. Conversely, the morphological properties used in AIMS II are Form 2-D and angularity. The index of Form 2-D is defined by Eq. 6-1. Form 2-D ranges from 0 to 20,

Table 6-6. Mean values of the FTI angularity and AIMS II angularity.

#8	FTI	AIMS II	#16	FTI	AIMS II
BFS	0.0350	4020.38	BFS	0.0560	4160.08
CO	0.0210	3801.85	CO	0.0499	3592.75
DLT	0.0148	3530.48	DLT	0.0423	3678.60
GGC	0.0241	3565.02	GGC	0.0554	3425.95
GGR	0.0222	2261.61	GGR	0.0421	2555.49
LST	0.0280	2874.60			

with a Form 2-D value of 0 for a perfect circle. Therefore, only angularity is compared between the FTI results and AIMS II results. Table 6-6 shows the angularity rankings according to the mean values of the FTI and AIMS II angularity results for fine aggregates.

$$Form2D = \sum_{\theta=0}^{360-\Delta\theta}\left[\frac{R_{\theta+\Delta\theta} - R_{\theta}}{R_{\theta}}\right] \qquad \text{Eq. 6-1}$$

where R_θ is the radius of the particle at angle θ, and Δθ is the incremental difference in the angle.

Figure 6-10 plots the angularity rankings of the FTI results and AIMS II results for #8 aggregates. The ranking values in this figure are calculated from Table 6-6 by dividing the mean value of each aggregate type by the minimum mean value for all types of #8 aggregates. For example, the FTI angularity ranking value of blast furnace slag #8 aggregates is obtained by dividing its mean FTI angularity of 0.350 by the minimum mean FTI angularity of 0.0148 for all #8 aggregates. For the six types of #8 aggregate, the FTI and AIMS II systems agree that blast furnace slag is the most angular; dolomite and rounded glacial gravel aggregates are the least angular.

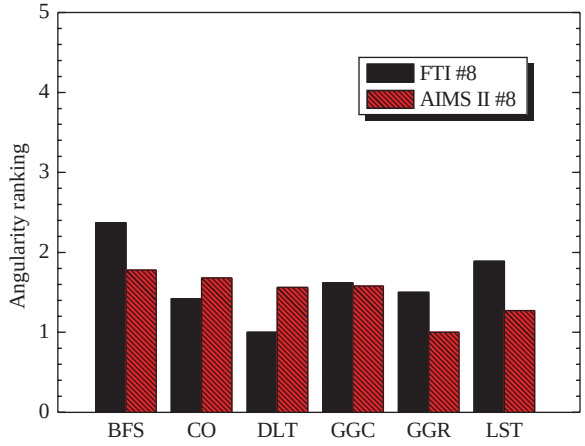

Note: BFS=Blast furnace slag; CO=Copper ore; DLT=Dolomite; GGC=Glacial gravel crushed; GGR=Glacial gravel rounded; LST=Limestone.

Figure 6-10. Angularity ranking of the FTI and AIMS II results for #8 aggregates.

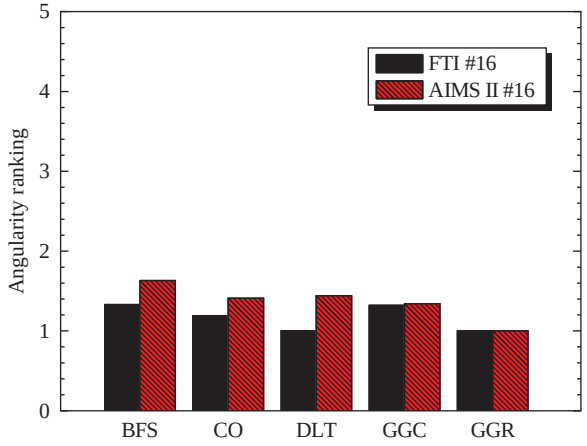

Note: BFS=Blast furnace slag; CO=Copper ore; DLT=Dolomite; GGC=Glacial gravel crushed; GGR=Glacial gravel rounded.

Figure 6-11. Angularity ranking of the FTI and AIMS II results for #16 aggregates.

Figure 6-11 plots the angularity ranking of the FTI results and AIMS II results for #16 aggregates. The ranking values in this figure are the result of dividing the mean value of each aggregate type by the minimum mean value for all types of #16 aggregate. The FTI system and AIMS II agree that blast furnace slag has the most angular aggregates, and rounded glacial gravel has the smoothest aggregates of the five types of aggregates. Copper ore and crushed glacial gravel have very close angularity values using both the FTI system and AIMS II.

6.5 Crushing Effect on Aggregate Morphological Characteristics Using the FTI system

There are two types of glacial gravel aggregate of the same origin: rounded glacial gravel as natural aggregates and crushed glacial gravel as crushed aggregates. To study the effect of crushing, the FTI results of both fine and coarse glacial gravel aggregates are presented in Table 6-7. They include the average values and standard deviations of sphericity, flatness ratio, elongation ratio, angularity, and texture for GGR and GGC aggregates. The sizes of GGR and GGC aggregates vary from ¾ in. to #16. To study the crushing effect on the morphological properties of aggregates, the distributions of morphological properties of both coarse and fine GGR and GGC aggregates are presented in Figure 6-12 through Figure 6-20.

Table 6-7. FTI angularity and texture results of GGR and GGC aggregates.

Aggregate Size			3/4"	1/2"	3/8"	#4	#8	#16
Sphericity	GGR	Average	0.68	0.70	0.79	0.73	0.53	0.39
		Standard deviation	0.09	0.06	0.12	0.11	0.12	0.14
	GGC	Average	0.74	0.74	0.79	0.69	0.58	0.30
		Standard deviation	0.10	0.09	0.06	0.13	0.16	0.10
Flatness ratio	GGR	Average	0.59	0.71	0.78	0.77	0.58	0.63
		Standard deviation	0.17	0.16	0.17	0.25	0.21	0.22
	GGC	Average	0.71	0.77	0.80	0.71	0.70	0.60
		Standard deviation	0.17	0.15	0.13	0.16	0.21	0.16
Elongation ratio	GGR	Average	0.75	0.71	0.80	0.73	0.54	0.32
		Standard deviation	0.11	0.11	0.14	0.18	0.21	0.14
	GGC	Average	0.77	0.74	0.80	0.69	0.55	0.22
		Standard deviation	0.12	0.12	0.11	0.16	0.22	0.11
Angularity	GGR	Average	8.44×10^{-5}	9.71×10^{-5}	1.09×10^{-5}	2.48×10^{-5}	2.22×10^{-2}	4.21×10^{-2}
		Standard deviation	1.13×10^{-4}	1.11×10^{-4}	1.94×10^{-4}	2.04×10^{-4}	1.48×10^{-2}	2.49×10^{-2}
	GGC	Average	2.31×10^{-4}	1.46×10^{-4}	1.47×10^{-4}	2.48×10^{-4}	2.41×10^{-2}	5.54×10^{-2}
		Standard deviation	4.25×10^{-4}	2.51×10^{-4}	1.98×10^{-4}	2.66×10^{-4}	1.49×10^{-2}	1.87×10^{-2}
Texture	GGR	Average	1.60×10^{-6}	3.54×10^{-6}	4.81×10^{-6}	1.44×10^{-5}	–	–
		Standard deviation	1.66×10^{-6}	4.32×10^{-6}	1.54×10^{-5}	1.54×10^{-5}	–	–
	GGC	Average	3.86×10^{-6}	2.69×10^{-6}	6.94×10^{-6}	9.33×10^{-6}	–	–
		Standard deviation	5.54×10^{-6}	3.37×10^{-6}	1.00×10^{-5}	1.64×10^{-5}	–	–

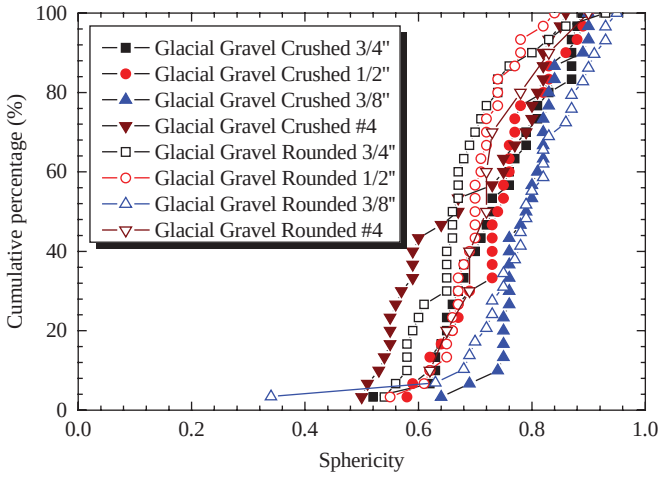

Figure 6-12. Effect of crushing on the FTI sphericity results of coarse aggregates.

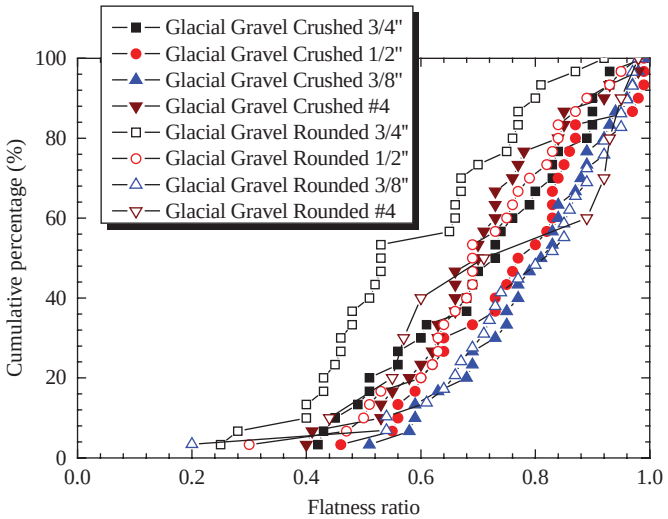

Figure 6-13. Effect of crushing on the FTI flatness ratio results of coarse aggregates.

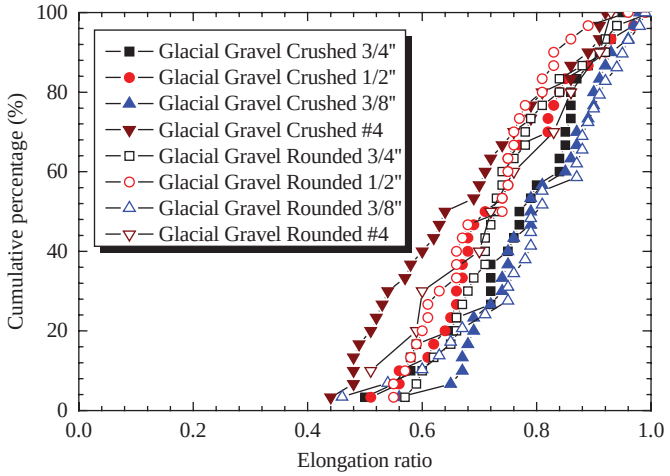

Figure 6-14. Effect of crushing on the FTI elongation ratio results of coarse aggregates.

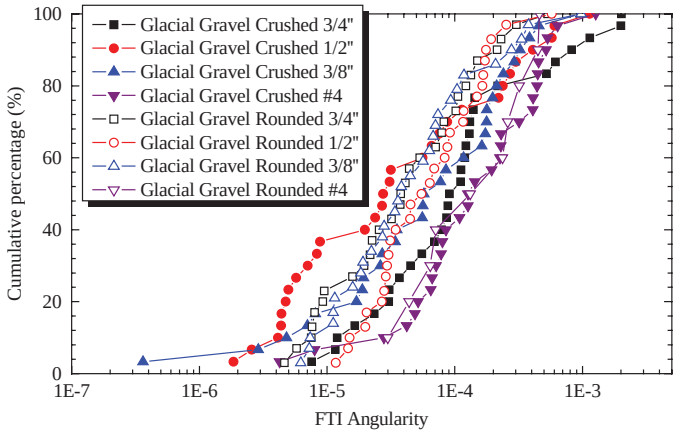

Figure 6-15. Effect of crushing on the FTI angularity results of coarse aggregates.

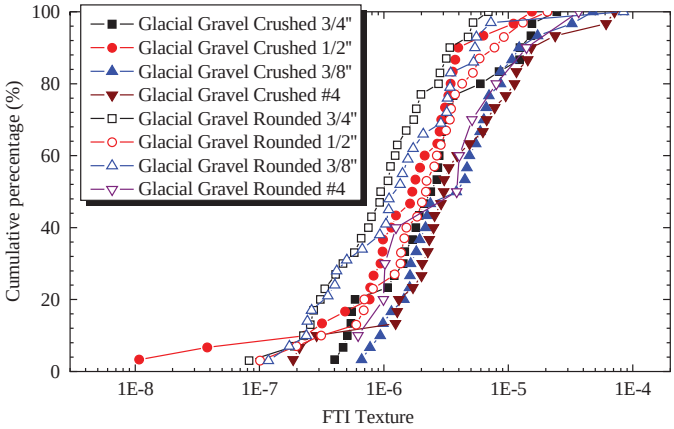

Figure 6-16. Effect of crushing on the FTI texture results of coarse aggregates.

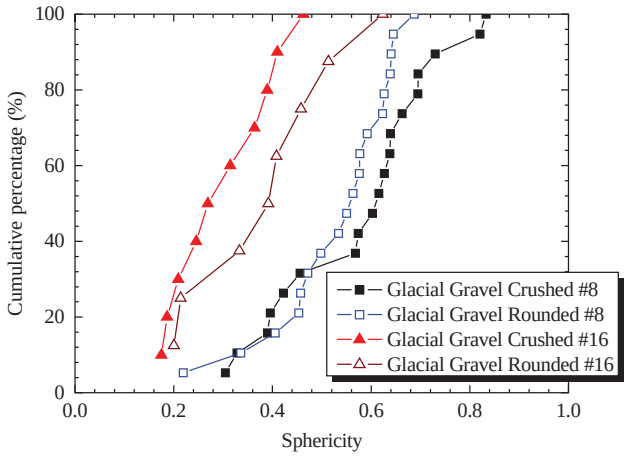

Figure 6-17. The FTI sphericity results of fine aggregates.

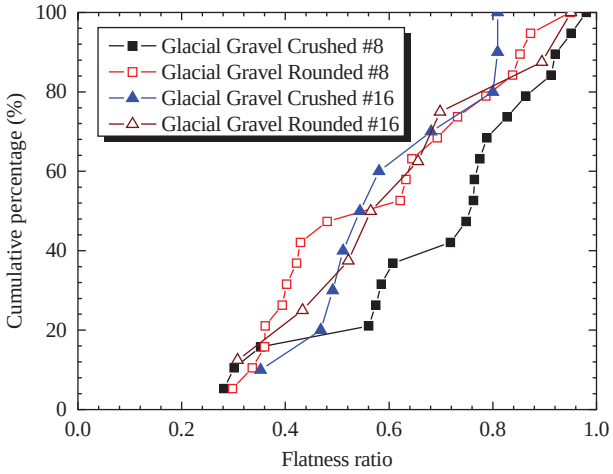

Figure 6-18. The FTI flatness ratio results of fine aggregates.

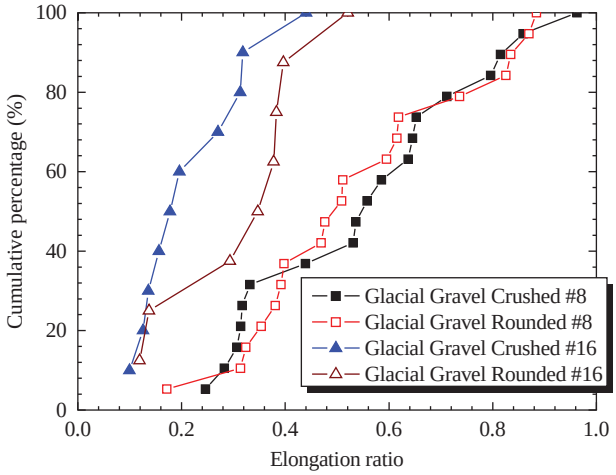

Figure 6-19. The FTI elongation ratio results of fine aggregates.

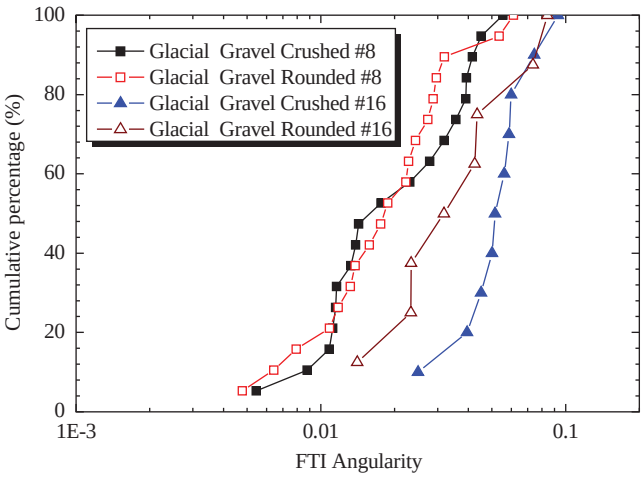

Figure 6-20. The FTI angularity results of fine aggregates.

Both GGR and GGC fine aggregates are from Kent, MI, as shown in Table 4-4. The data presented in Table 6-7 indicate that the sphericities of GGR and GGC fine aggregates do not have a significant difference. The flatness ratio and elongation ratio of all the GGC fine aggregates are generally smaller than those of the GGR fine aggregates, except for the #4 and #16 aggregates. The greater values of the flatness ratio and the elongation ratio for GGC aggregates indicate that crushed aggregates (i.e., GGC) generally tend to be less flat and less elongated than natural aggregates (i.e., GGR). Also, an increase in the angularity and texture values from GGR to GGC aggregates is observed across all sizes. The increase of angularity and texture values from GGR to GGC suggests that both coarse and fine GGC aggregates are more angular with rougher surface texture than GGR aggregates. A possible reason that crushed aggregates have greater values of angularity and texture for fine aggregates is that fine aggregates may have more fractured surfaces.

6.6 Feature Comparisons of the FTI System to the Other Aggregate Imaging Systems

Information collected from the literature review (in Appendix A) is presented in Table 6-8 to compare the features of nine available aggregate imaging techniques. There are two types of aggregate imaging technique (i.e., the dynamic digital image method and the statistic digital image method). Apparently, the FTI system is much less expensive than the other aggregate imaging systems.

Table 6-8(a). Features of aggregate imaging systems.

Test Method	Aggregate Imaging System	Estimated Equipment Cost ($)	Analysis Speed	Accuracy	Ease of Use	Repeatability
Dynamic Digital Image Method	VDG-40 videograder	45,000	H	M	M	L
	Computerized particle analyzer	25,000	H	M	M	M
	Micrometrics Optisizer particle size distribution analyzer (PSDA)	50,000	L	M	H	L
	Video image system (VIS)	60,000	H	M	M	L
	Camsizer	45,000	M	M	M	L
	Winshape	35,000	H	M	M	M
	UIAIA	35,000	M	H	M	H
Statistic Digital Image Method	AIMS II	35,000	H	H	H	H
	FTI	20,000	M	H	M	H

Note: H = high; M = medium; L = low. (Based on Masad et al., 2007).

Table 6-8(b). Features of aggregate imaging systems.

	Aggregate Imaging System	Aggregate Size Range	No. of Cameras	Dimension(s) of Image	Measured Aggregate Characteristics
Dynamic Digital Image Method	VDG-40 videograder	#16–1.5”	1	2	Shape
	Computerized particle analyzer	#140–1.5”	1	2	Shape
	Micrometrics Optisizer PSDA	#200–1.5”	1	2	Shape
	VIS	#16–1.5”	1	2	Shape
	Camsizer	#50–3/4”	2	2	Shape angularity
	Winshape	#4–1”	2	3	Shape angularity
	UIAIA	#8–1”	3	2	Shape angularity texture
Statistic Digital Image Method	AIMS II	#200–1”	1	3	Shape angularity texture
	FTI	#50–3/4”	1	3	Shape angularity texture

CHAPTER 7

Conclusions

7.1 General Conclusions

The objectives of this project have on the whole been achieved with the development and evaluation of the FTI system. Both the hardware and software systems of FTI are functional. The system can characterize aggregate shape, angularity, texture, surface area, and volume of a large range of aggregate sizes with high accuracy. The FTI system consists of a CCD camera, a fringe source, a particle tray, and a MATLAB software package. Aggregates are placed on the adjustable-height particle tray under an angled mirror, and the CCD camera captures digital images of aggregates reflected from the angled mirror. Three images need to be captured for further analysis and reconstructing of 3-D surfaces: a visual image and two images taken with lasers of wavelengths of 675 nm and 805 nm. The three images are analyzed using the MATLAB software that implements the Fourier transform method to generate a matrix of the 3-D coordinates of aggregate surfaces. The 3-D coordinate matrix is further analyzed using 2-D Fourier transform to quantify the angularity and texture of aggregates. The shape properties are directly derived from the measured three dimensions calculated from the FTI system. Based on the operations and evaluations of the FTI system, the following conclusions can be drawn:

(1) The FTI system is able to characterize aggregates with a wide range of sieve sizes, from ¾ in. to #50 for individual particles. Image processing using the Fourier transform is able to generate accurate 3-D coordinates with a resolution of up to 35.4 μm/pixel in the *x, y* directions and 22 μm in the *z* direction. The FFT2 method can be applied to the 3-D coordinate matrix to extract angularity properties of both coarse and fine aggregates as well as texture properties of coarse aggregates. The FTI analysis results also show that the angularity and texture values show different magnitudes between coarse aggregates and fine aggregates, but the relative angularity and texture rankings remain rational. That is to say that the angularity and texture values are aggregate size dependent.

(2) The statistical analysis indicates that there is no significant difference between the FTI results and manual measurements of the dimensions in general. The dimension measurements are the basis for all the derived parameters of shape, angularity, texture, surface area, and volume. This comparison actually validates the FTI methods. Both ANOVA and *t*-test of the coarse aggregates in Set 1 demonstrate that the shape characteristics obtained through the FTI system are in good agreement with those calculated from manual measurements. The results also demonstrate the reliability of the FTI system to quantitatively evaluate coarse aggregates.

(3) Comparison of FTI results with those from the AIMS II and UIAIA systems shows that the three aggregate imaging systems can analyze aggregates in Set 1 with reasonable roughness rankings, even though there are some differences. Both blast furnace slag and crushed glacial gravel are shown to have higher angularity than other aggregates, followed by iron ore and copper ore. Also, rounded glacial gravel is shown by all methods to have the smoothest surface texture. In other words, when angularity and texture are significantly different, these systems may be sensitive enough to differentiate them; when angularity and texture are not significantly different, these systems may rank them differently.

(4) Since the Micro-Deval test may break particles, exposing new fractured surfaces, the FTI results of coarse aggregates in Set 2 presented in this report are not conclusive. This may be attributed to the small sample population of particles studied. A larger sample population of aggregate particles may need to be analyzed to ensure that the statistical nature of such properties is well captured.

(5) Crushing has a great influence on the angularity and texture for glacial gravel aggregates. Crushed glacial gravel aggregates have greater angularity and rougher surface texture than rounded glacial gravel aggregates. The FTI system has successfully captured such effects.

(6) While the FTI system can be further enhanced through the use of different cameras and lasers, it is not realistic to use one set of hardware to reach a resolution of 1 micrometer for all aggregate sizes. It is also not realistic to image and analyze individual particles of very small sizes.
(7) While it is possible to stitch several surfaces into the entire surface of a particle and calculate the volume of the particle and the volumetric gradations, it is very time consuming and not advantageous compared to other methods such as X-ray computed tomography. The capability has been developed, but no further efforts have made to calculate the surface area and the volume of individual particles for all size ranges.
(8) Further evaluations of the FTI system should also be conducted via characterizing more aggregates from various sources for the robustness of the FTI system. It is essential to further test the validity and repeatability of the FFT2 analysis method.

7.2 Recommendations

The original goal was to develop a system that was able to image aggregates ranging from 2 in. to #4, #4 to #200, and passing #200. While in theory the FTI approach should be able to achieve this, the commercially available components with one set of design cannot achieve it. The current FTI system is capable of imaging aggregates with the sizes passing a 1-in. sieve and retaining on a #50 sieve due to the limited view field of the CCD camera. Future research could be conducted to replace the CCD camera with one that has a larger view field to image aggregates retaining on a 1-in. sieve. Higher resolutions can be also achieved through appropriate selections of the components.

Further evaluation of the FTI system could be conducted on more aggregates from various sources for the robustness of the FTI system and corresponding analysis method. It is essential to further test the validity and repeatability of the imaging and analysis methods.

Currently the FTI system is not automatic during all operations. It needs the user's judgment to select a threshold value to identify an aggregate profile and choose reference rows to reconstruct 3-D surfaces. Further research could focus on the improvement of automatic operation.

The different imaging and analysis methods for direct measurements of shape, angularity, and texture use different definitions. This prevents the development of a commonly accepted set of parameters for shape, angularity, and texture. A national joint effort to develop a consensus on defining the shape, angularity, and texture would be worthwhile.

Once such consensus on a set of parameters has been developed, a national database on aggregate morphological characteristics could be built using the FTI system for all typical aggregates used in paving engineering. This database could provide engineers and researchers with easy access to the engineering properties of aggregates for mix design and performance assessments.

Even though a lot of research has been conducted on morphological characteristics of aggregates, the quantitative relationship between aggregate morphological characteristics and the performance of HMA and PCC is still not well understood. Therefore, further research could focus on developing quantitative relationships between aggregate shape, angularity, and texture and the performance of aggregate assembly and mixtures.

In addition, the FTI system could be extended to imaging the surface of pavements for calculating rutting depth, surface roughness, and cracking densities, and the monitoring of pavement deformation.

While it is possible to calculate the surface areas and volumes of individual particles, it is very time consuming. In addition, other more convenient approaches such as the XCT method are available. The team doesn't recommend work on further development of surface area and volume calculation methods for implementation at this time. Academic research along this direction may still be encouraged.

7.3 Implementation Plan and Cost Assessment

7.3.1 Implementation Plan

This project developed an effective aggregate imaging technique to accurately quantify aggregate morphological characteristics such as shape, angularity, and texture. The corresponding analysis methods are easy to interpret and implement. The FTI system could be implemented for better quality control of aggregates in asphalt concrete and cement concrete mix design. The FTI system could be used for academic research or QC/QA by contractors and highway agencies. If the automation of the FTI system operation were improved, the upgraded FTI system could be installed on the side of a conveyor along a production line of aggregates. In this way, the upgraded FTI system could automatically detect whether the morphological characteristics of aggregates in the conveyor are of good quality during the production process.

(1) The FTI system could be used to enhance the efficiency of other imaging techniques that are labor-intensive and time consuming, and sometimes subjective. Unlike other laboratory tests, the FTI system is able to objectively quantify the morphological properties of either an individual aggregate or a number of aggregates at the same time.
(2) The FTI system could be used to analyze the change of morphological characteristics of aggregates due to

polishing, and image the pavement surfaces for roughness and distress quantification. By upgrading the FTI system with more powerful CCD cameras and installing the upgraded FTI system in a vehicle, it is possible to extend its application to detect pavement roughness and cracks.

These potential applications indicate the possible direction of future implementation. The following implementation steps are proposed: (1) refining the system for better automation; (2) extending NCHRP Project 4-34 into another NCHRP study or a pooled-fund study to mainly evaluate the aggregate characteristics of a larger number of aggregates; (3) establishing criteria for aggregate acceptance, mix blending, and quality control and assurance for industry; (4) developing a formal AASHTO standard; and (5) extending its application to pavement performance evaluations.

7.3.2 Cost Assessment

Key products of this project include an FTI image system and the MATLAB software package. Implementation costs are estimated at a total of $24,000, made up of the following:

(1) A complete setup of the FTI image system is estimated at a total cost of $20,000.
(2) Training of personnel to acquire and analyze images using the MATLAB software and programs can be completed in a 4-hour workshop for 10 to 20 individuals for about $4,000.

References

Al-Rousan, T., Masad, E., Tutumluer, E., and Pan, T. (2006). Evaluation of Image Analysis Techniques for Quantifying Aggregate Shape Characteristics. *Construction and Building Materials,* 21, 978–990.

Brandon, D. and Kaplan, W. D. (1999). *Microstructural Characterization of Materials.* Wiley, New York.

Fletcher, T., Chandan, C., Masad, E., and Sivakumar, K. (2003). Aggregate Imaging System (AIMS II) for Characterizing the Shape of Fine and Coarse Aggregates. *Transportation Research Record: Journal of the Transportation Research Board, No. 1832.* Transportation Research Board of the National Academies, Washington, D.C., 67–77.

Lally, E. M. (2010). Fourier Transform Interferometry for 3-D Mapping of Rough and Discontinuous Surfaces. PhD dissertation.

Masad, E., Al-Rousan, T., Button, J., Little, D., and Tutumluer, E. (2007). *NCHRP Report 555: Testing Methods for Characterizing Aggregate Shape, Texture, and Angularity.* Transportation Research Board of the National Academies, Washington, D.C.

MathWorks (2010). Help manual in MATLAB R2010b.

Rao, C. and Tutumluer, E. (2000). A new image analysis approach for determination of volume of aggregates. *Transportation Research Record 1721.* TRB, National Research Council, Washington, D.C., 73–80.

Smith, S. W. (1999). The Scientist and Engineer's Guide to Digital Signal Processing (2nd edition), Chapter 11, California Technical Publishing.

Wang, L., Wang, X., Mohammad, L., and Abadie, C. (2005). Unified Method to Quantify Aggregates Shape Angularity and Texture Using Fourier Analysis. *Journal of Material in Civil Engineering.* Vol. 17, No. 5, pp. 498–504.

Wang, R. (2007). Two-Dimensional Fourier Transform. http://fourier.eng.hmc.edu/e101/lectures/Image_Processing/node6.html.

APPENDIX A

Literature Review

Appendix A is not published herein but is available at http://apps.trb.org/cmsfeed/TRBNetProjectDisplay.asp?ProjectID=867.

APPENDIX B

The FTI System Components

The FTI system consists of the image collection system and MATLAB software package. Figure B-1 illustrates the FTI system setup with components.

1. Image Collection System

- Fringe source—provides two types of laser, with wavelengths of 675 nm and 805 nm
  - 675-nm SLD, 805-nm LD, and a fiber switch
  - Double pinhole mask
- Camera setup—capture visual image and two other images under the laser in the mirror
  - CCD camera, bellows, macro lens assembly
- Aggregate position system—place aggregate(s) on the height-adjustable platform
  - Particle tray and a 45°-angled mirror

2. MATLAB Software Package

- Main program—process images acquired using FTI system to output 3-D coordinates
- Error correction program—window out error areas in the 3-D coordinates from the main program
- Morphology analysis program—quantify morphological characteristic of images aggregates

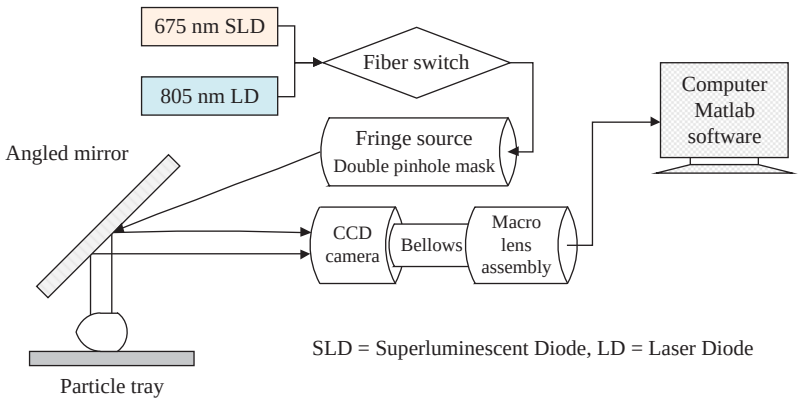

Figure B-1. Illustration of FTI image system setup.

3. Fourier Transform Interferometric Imaging System Equipment List

Item (Category and Detail)	Vendor	Price	Purchase Date	Install Date
Camera and Lens System		**$5,876.95**		
CCD Camera	Astrovid	$2,985.00	10/18/2006	12/20/2006
Track Mount System	Thorlabs	$291.00	10/30/2006	12/20/2006
Macro Lens & Filter	Schneider Optics	$1,367.00	10/18/2006	2/28/2007
Bellows & Adapters	B&H Photo	$733.95	10/30/2006	2/28/2007
Add'l Misc Camera Items	Thorlabs	$500.00	–	–
Image Acquisition System		**$3,800.00**		
Computer	Dell	$2,800.00	3/5/2007	3/20/2007
Software	GeoMagic	$1,000.00	–	–
Fringe Generator System		**$6,867.17**		
1st Gen. Coupling Lens Assy.	Newport	$502.00	10/18/2006	12/20/2006
Test Coupler & Laser Diodes	Thorlabs	$367.60	10/30/2006	12/20/2006
Mounting Hardware	Thorlabs	$312.57	10/30/2006	12/20/2006
Custom Dual-Wavelength Coupler	Gould Fiber Optics	$424.00	1/17/2007	in progress
HeNe Laser	Edmund Optics	$1,370.00	–	–
2nd Gen. Coupling Lens Assy.	Newport	$1,423.00	–	–
Temp. Shifted Polishing Jig	Thorlabs	$200.00	–	–
Whitelight Interferometer	Thorlabs	$200.00	–	–
Fiber Optic Switch	Thorlabs	$1,068.00	–	–
Add'l Laser Diodes & Misc Hardware	Thorlabs	$1,000.00	–	–
Particle Positioning System		**$3,039.56**		
1st Generation Mount	Thorlabs	$164.16	10/30/2006	12/20/2006
Particle Gluing Station	Thorlabs	$131.13	10/30/2006	12/20/2006
System Enclosure	Misc	$193.71	2/6/2007	2/28/2007
2nd Generation Mount	Thorlabs	$248.56	2/21/2007	4/30/2006
System Base – Optical Breadboard	Thorlabs	$938.00	–	–
Angled-Mirror System	Edmund Optics	$364.00	–	–
Additional Hardware	Misc	$1,000.00	–	–
Total Price:	"	**$19,583.68**	"	"

APPENDIX C

Initial Efforts for the Particle Mounting System

1. Overview of the Initial Image System

Before developing the assembly of the 45°-angled mirror and aggregate image particle tray, efforts were made for aggregate mounting systems to glue an aggregate at the very end of a needle. The aggregate mounting system is used for holding particles ranging from 1 mm to 50 mm in size. A preliminary fringe generator was set up to facilitate the system alignment and testing process. The fringes were uniformly spaced and fit the predictions based on the calculations in the design.

Figure C-1 and Figure C-2 show the preliminary system in its entirety. They illustrate the camera track and carrier, to which the bellows is mounted. The fringe generator and coupler are shown along with the particle mounting and gluing systems. The laser and coupler are inside the wooden enclosure.

2. Particle Mounting System

Figure C-3 shows the preliminary mount system. However, it is difficult to adjust this system accurately, and it has low stability during adjustment. The lack of a fine-tuning mechanism is especially apparent at high magnification, where the particle must be centered within a 3.5×4.5 mm area.

Figure C-4 illustrates an improved particle mount design with both coarse and fine adjustments in the vertical and horizontal directions. Figure C-4(a) shows the improved design of the particle mounting system, and Figure C-4(b) presents the horizontal arm of the improved particle system. Coarse linear adjustments in the horizontal direction are made using a standard ½-in. post and post holder assembly. Fine horizontal adjustments can be made by turning the screw of the translating post, which provides up to 6 mm of travel, with 1 mm per turn resolution.

The diameter of the vertical post has been increased from 0.5 in. to 1.5 in. for stability improvement. Positioning the large post clamp on the mounting post sets the coarse vertical position of the mount. Fine tuning of the particle height is performed by turning the base of the adjustable height collar, which has a range of 33 mm and resolution of 0.64 mm per turn. Adjustments along the camera imaging axis are made by rotating the boom, a motion that has shown experimentally to be both stable and accurate. Additionally, the post collar fixes the assembly height during boom rotation, allowing for independent *x, y,* and *z* axis positioning.

Figures C-5, C-6, and C-7 illustrate the particle mounting system used to glue particles to the various sizes of needles. Large rocks, between 10 mm and 50mm in size, are held in the adjustable vise, while particles as small as 1 mm are immobilized on an adhesive pad during the gluing process. Mounting needles are held in place by a series of pin vises, and a movable, rotating arm allows the user to position the needle for mounting. A miniaturized version of this mounting system, involving precision positioning stages and a microscope-objective lens, is planned for mounting particles smaller than 1 mm in diameter.

Figure C-8 and Figure C-9 show the particle mount and the system of targets used to align the object for imaging. The mounting arm and pin vise can be positioned and rotated to achieve virtually any viewing angle. Two targets are used to aid in alignment: one for the *x-y* position and one for the *x-z* position of the particle.

Figure C-10 and Figure C-11 show the interference pattern produced by the fiber-based pinhole interferometer. The fringe period (i.e., the distance between two neighboring straight lines shown in Figure C-10) is approximately 2 mm, and the lines are straight and well aligned. Figure C-11 illustrates the pattern on a medium-sized particle.

3. Limitations of Particle Mounting System and the Proposed Angled Mirror System

After the development of the particle mounting system, the NCHRP project panel raised concerns about the practical usability of the imaging system, especially in the practice of

Figure C-1. Front system view.

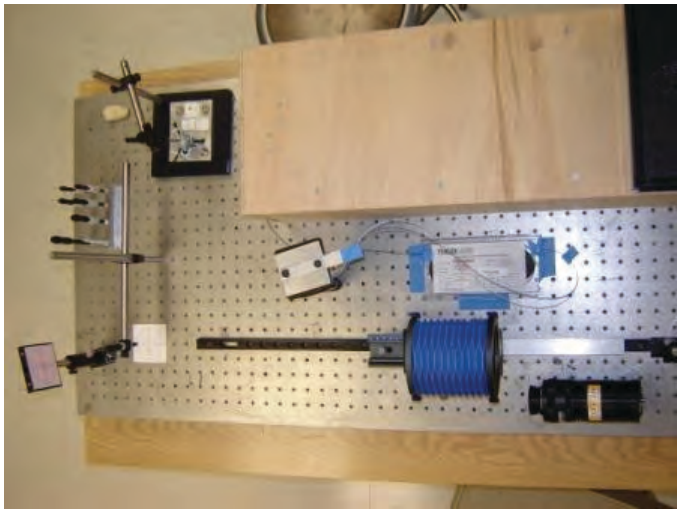

Figure C-2. Top system view.

pavement engineering. In particular, they indicated a strong need for the system to be able to quickly image multiple particles at once. During the visit of the project panel, the angled-mirror design was proposed. A high-quality mirror, tilted at a 45° angle, is placed directly above the object. This mirror redirects the illumination rays emanating from the fringe generator. It also redirects the imaging rays, which are received by

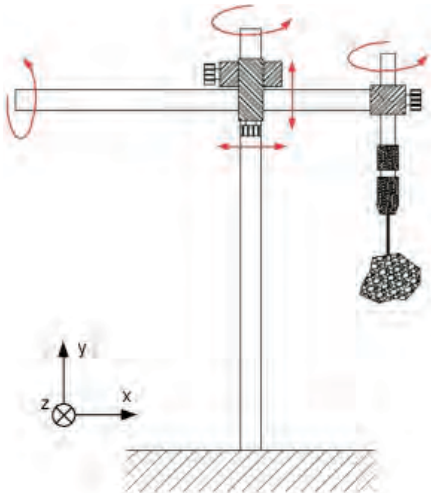

Figure C-3. Preliminary particle mount.

the CCD camera. The object, no longer glued to an articulated mount, is placed on a flat plate for imaging.

The orientation depicted in Figure C-12 has several advantages over the previous system design. It eliminates the need for the gluing of particles to needles, which saves time and makes the system easier to use. The angled-mirror design also allows multiple particles to be imaged at the same time. The user simply places several aggregate particles on the plate, and the FTI software can easily separate the data into those for individual particles.

These advantages come at a price: the viewing angle of the image is limited. With the needle mount, the user is able to rotate the particle in any direction, providing the possibility of full 360∞ images. Using the plate-mounted system detailed here, particles can only be viewed directly from above. It is important to note that the system still generates a 3-D surface profile. Also, the user does have the ability to flip the aggregates over, generating images of the bottom side as well. This configuration is similar to the one used on the commercial line-scan system.

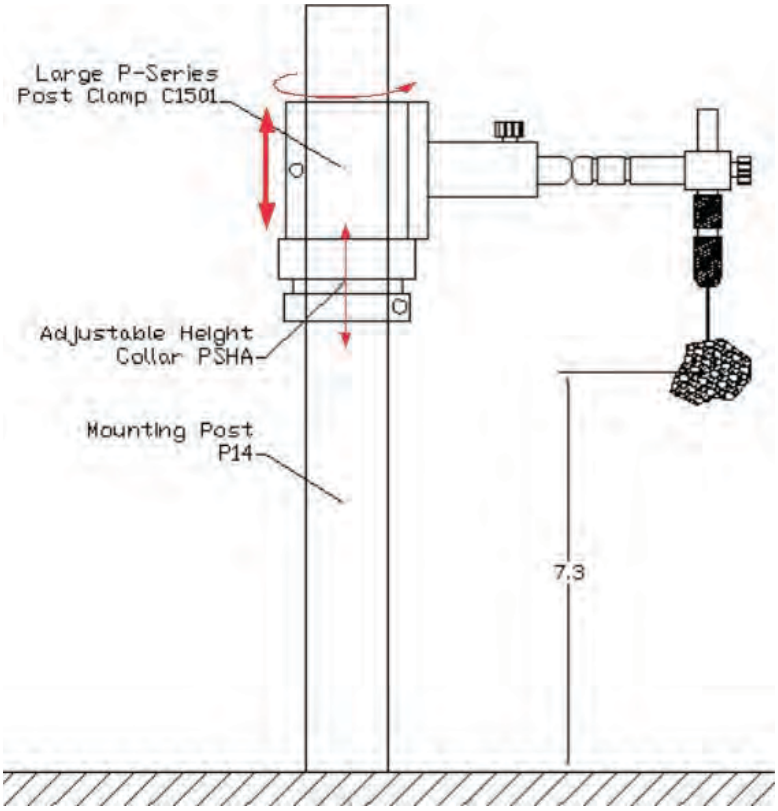

(a) Overall system

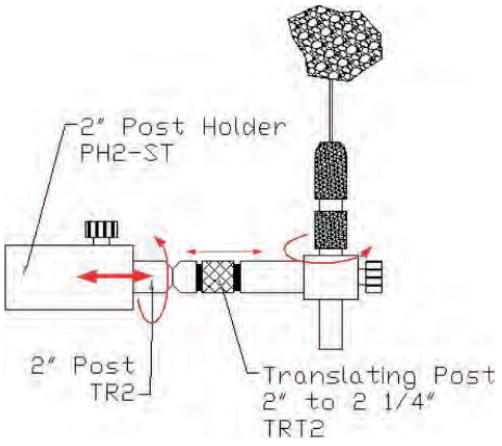

(b) Horizontal arm

Figure C-4. Improved particle mount.

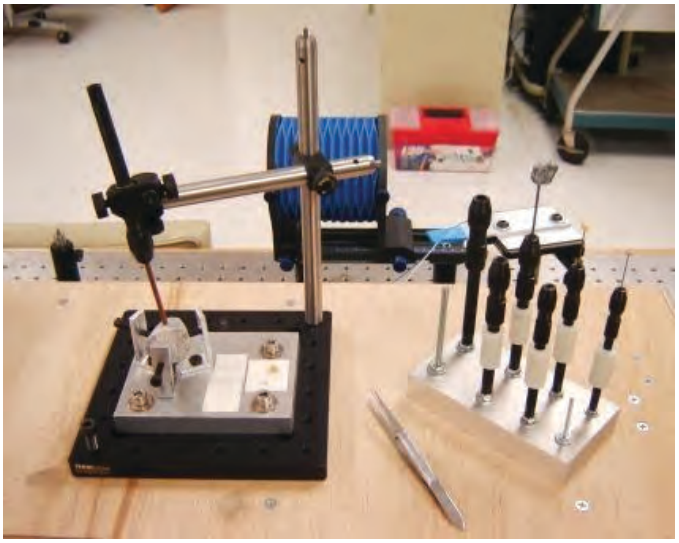

Figure C-5. Particle gluing station.

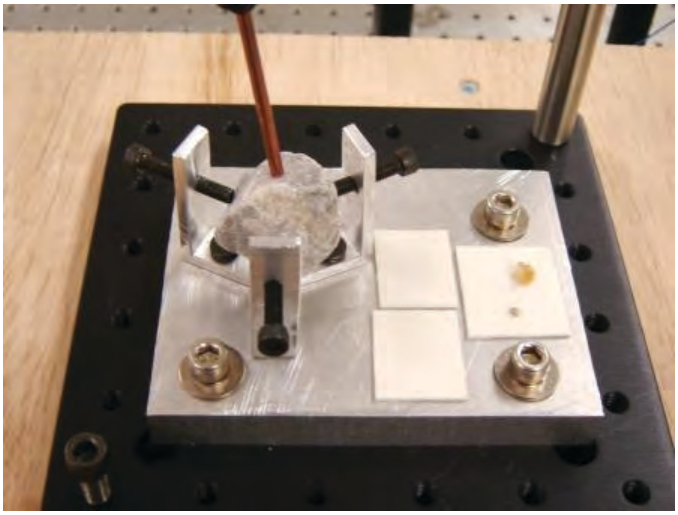

Figure C-6. Large/medium particle holders, detail.

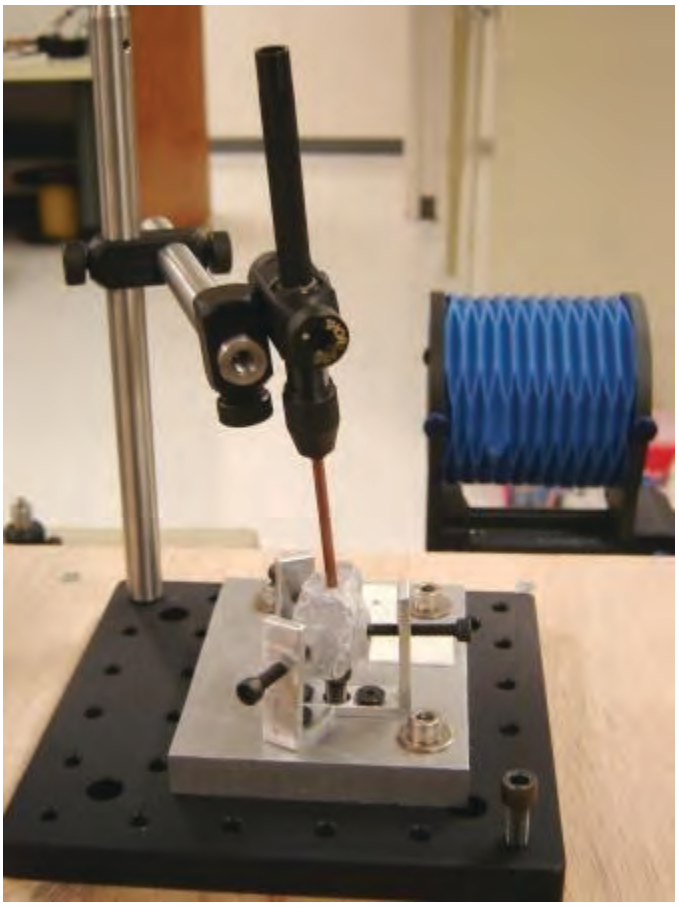

Figure C-7. Mounting a large particle.

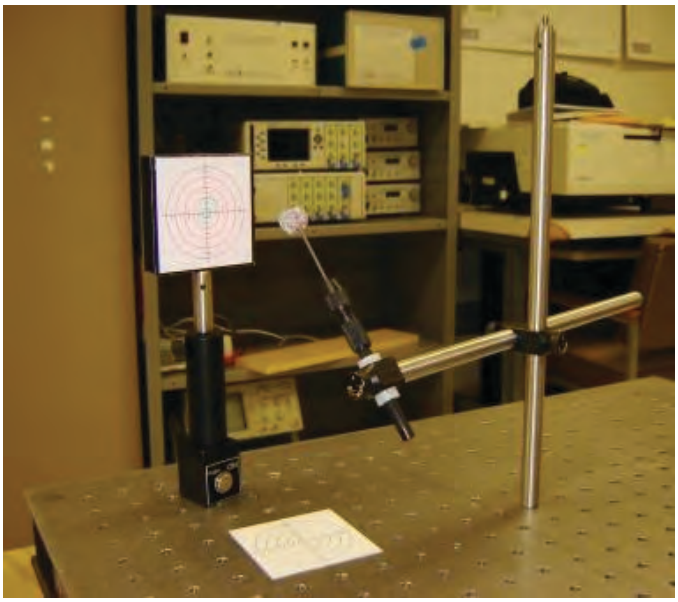

Figure C-8. Particle mount.

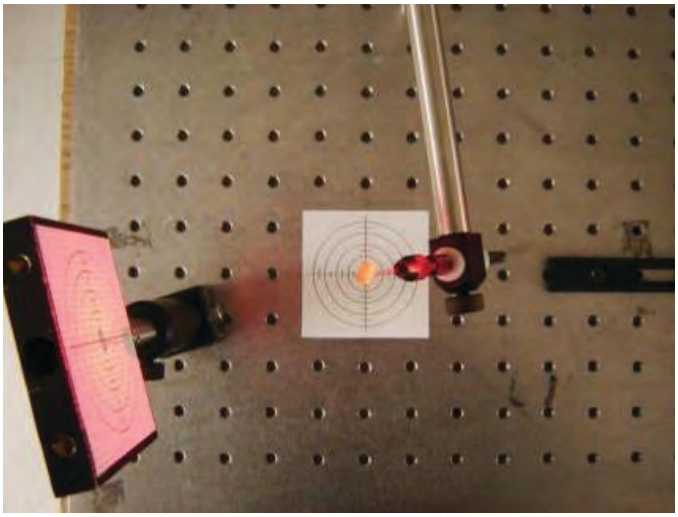

Figure C-9. Aligning the particle mount.

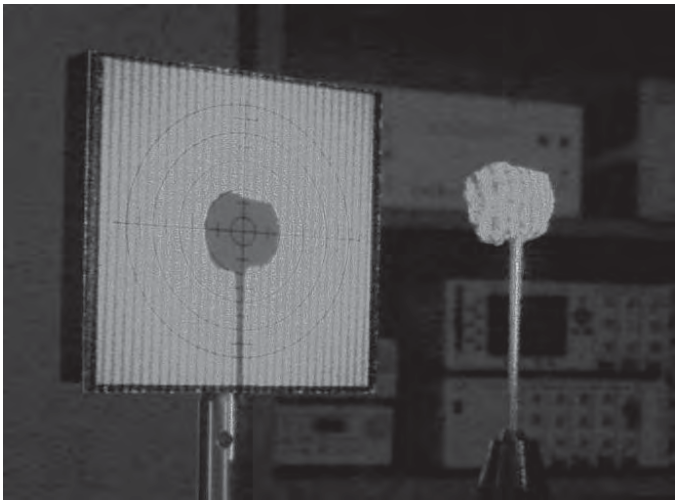

Figure C-11. Particle illuminated by fringe pattern.

Figure C-10. Test fringes.

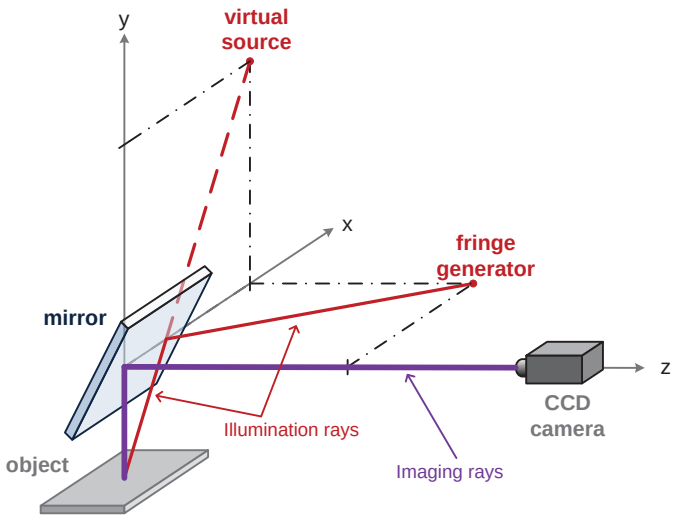

Figure C-12. Angled mirror system.

APPENDIX D

Test Protocol in AASHTO Format

1. Scope

1.1 This standard covers the determination of aggregate characteristics using gradation and shape, angularity, and texture analysis determined by means of image analysis.

1.2 The value stated in SI units (SI units and units specifically approved in Practice E 380 for use with SI units) is regarded as the standard. The values in parentheses are provided for information purposes only.

1.3 *Use of this standard may involve use of hazardous material, operations, and equipment. This standard does not purport to address all of the safety issues during its use. It is the responsibility of users of this standard to establish appropriate safety and health practices and determine the applicability of regulatory limitations prior to use.*

2. Referenced Documents

2.1 AASHTO Standards

M 92 Standard Specification for Wire-Clot Sieves for Testing Purposes

T 2 Sampling of Aggregates

T 27 Sieve Analysis of Fine and Coarse Aggregates

T 84 Standard Method of Test for Specific Gravity and Absorption of Fine Aggregate

T 85 Standard Method of Test for Specific Gravity and Absorption of Coarse Aggregate

T 248 Reducing Samples of Aggregate to Testing Size

2.2 ASTM Standards

C 125 Terminology Relating to Concrete and Concrete Aggregates

C 136 Test Method for Sieve Analysis of Fine and Coarse Aggregates

C 702 Practice for Reducing Samples of Aggregate to Testing Size

D 8 Terminology Relating to Materials for Roads and Pavements

D 75 Practice for Sampling Aggregates

D 4791 Test Method for Sieve Analysis of Fine and Coarse Aggregates

E 11 Specification for Wire-Cloth Sieves for Testing Purposes

E 380 Practice for Use of the International System of Units (SI) (the Modernized Metric System)

3. Terminology

3.1 Definition

3.1.1 *Shape*—describes the maximum and minimum dimensions of coarse aggregate particles.

3.1.2 *Coarse Aggregates*—Aggregates that are retained on a 4.75-mm (#4) sieve.

Sieve sizes: 19.0 mm (¾ in.), 12.5 mm (½ in.), 9.5 mm (⅜ in.), 4.75 mm (#4).

3.1.3 *Fine Aggregates*—Aggregate materials passing a 4.75-mm (#4) sieve.

Sieve sizes: 2.36 (#8), 1.18 mm (#16), 0.60 mm (#30), 0.30 mm (#50).

3.2 Morphology characteristics for both coarse and fine aggregates

3.2.1 *Sphericity (S)*—Applied to coarse aggregate sizes only and describes the overall three-dimensional shape of a particle. Sphericity has a relative scale of 0 to 1. A sphericity value of 1 indicates a particle has equal dimensions (cubical or spherical ball).

$$S = \sqrt[3]{\frac{D_s D_m}{D_l^2}} \quad (1)$$

where D_s = shortest particle dimension,
D_m = intermediate particle dimension, and
D_l = longest particle dimension.

3.2.2 *Flat and Elongated*—those particles having a ratio of longest dimension to shortest dimension greater than a specified value.

$$\text{Flatness Ratio} = D_s / D_m \quad (2)$$

$$\text{Elongation Ratio} = D_m / D_l \quad (3)$$

3.2.3 *Angularity*—is related to the number and sharpness of the corners of aggregate particles. Angularity is analyzed using the two-dimensional Fourier transform (FFT2) method. This method quantifies the changes of gradient on the aggregate top surface using two-dimensional Fourier transform coefficients of the three-dimensional coordinate matrix. This method starts by calculating angularities using various matrix sizes of two-dimensional Fourier transform coefficients within a small frequency range, defined as *angularity frequencies.* While plotting the relationship between angularity factor and corresponding matrix area (matrix area as *x*-axis; correspondingly, angularity as *y*-axis), the slope is defined as angularity.

3.2.4 *Texture*—describes the relative smoothness or roughness of aggregate surfaces. The FFT2 method calculates textures using various matrix sizes of two-dimensional Fourier transform coefficients within a high-frequency range, defined as *texture frequencies.* While plotting the relationship between texture factor and corresponding matrix area (matrix area as *x*-axis; correspondingly, texture factor as *y*-axis), the slope is defined as texture.

4. Significance and Use

4.1 This test method is primarily used to determine the morphological characteristics of aggregates used in infrastructure construction materials, such as asphalt and cement concrete, unbounded aggregate layers, and so forth. This method provides direct measurement of aggregate shape, angularity, and texture using three-dimensional coordinates of aggregate surfaces, consequently providing more consistent and reliable results by using the Fourier Transform Interferometry (FTI) system to predict performance of fundamental infrastructure such as highway pavements, cement concrete structures, and so forth. It allows the separate measurements of shape, angularity, and texture, which may correlate to different mixture properties. The method may be extended to the measurement or mapping of the surface properties of other materials or structures.

5. Apparatus

5.1 The FTI system is an integrated system composed of fringe sources, a charged-coupled device (CCD) camera, adjustable-height particle tray, angled mirror, and the associated MATLAB software.

6. Preparation of Test Samples

6.1 Obtain aggregate specimen in accordance with ASTM D75, and reduce the specimen to an adequate sample size in accordance with ASTM C702.

6.2 Wash and oven dry the reduced sample at 230 ± 9°F to constant mass. The coarse aggregate sample should contain at least 30 particles. The fine aggregate should be about 20 g.

6.3 If the aggregate sample has a size passing #50, for instance, #100, #200, and so forth, the aggregates should be put into a sample holder of a diameter of 2.60 mm to be further imaged.

7. Procedure

7.1 Aggregate Imaging

7.1.1 The system is started with both the hardware and software initialized. To begin with, the CCD camera cord is plugged into the Starlight Xpress power supply, and the camera lens cap is removed. The LD/TEC controller is turned on to make toggle states with both THERMISTOR SET and THERMISTOR REAL set as 10.0 Kohm, and IOPERATION REAL as 200 mA. To initialize the software, both OSW-Control and SXV_H9_USB should be opened. In OSW-Control, COM3 should be selected. In SXV_H9_USB, go to "view" to select "fit to window."

7.1.2 Turn on the fluorescent light in the enclosure box, and place OSW switch on Port 2. Place a coarse aggregate particle on the adjustable-height particle tray, making sure to minimize shadowing by laser input from the right side. Then use the Vernier micrometer to adjust the height of the tray to make sure the entire top surface of the aggregate particle is below "Max Height" line. Adjust the tray height to keep the aggregate top surface within the best range, as shown in Figure D-1. After that, record the tray height for particle thickness measurement later on.

7.1.3 Open SXV_H9 control interface to enable "Continuous Mode" and press "Take Photo." Press CTRL-Z to get to the control interface of SXV_H9_USB to adjust exposure time in the window of "EXPOSURE RANGE" for the best views in image, and move the particle to the center of image. After that, three images are taken for the three-dimensional surface reconstruction,

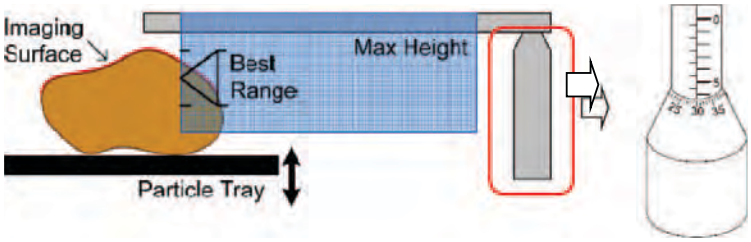

Figure D-1. Best height range of the adjustable-height particle tray (left), and Vernier micrometer (right).

including a visual image taken under fluorescent light, an image taken under the infrared laser with a wavelength of 805 nm while keeping OSW switch at Port 2, and an image under the red laser with a wavelength of 675 nm while keeping OSW switch at Port 1.

7.1.4 In the interface of SXV, select "Histogram" to check for correct exposure level. Histogram should fall off toward zero at higher intensity levels, as shown in Figure D-2. A small vertical line on the right of the image indicates a reasonable number of "filled" pixels. Increasing the exposure time will result in a bright image, and decreasing the exposure time will result in a dark image. All three images should be saved in the same folder to work properly with the image processing software, with the first portion of the filename being the same and extensions as follows, respectively: _v.fit, _8.fit, _6.fit.

7.2 Aggregate Image Processing

7.2.1 The FTI software compiled in MATLAB is used to analyze the three images acquired in the FTI system. In the graphical user interface (GUI) of the FTI software (shown in Figure D-3), load any one of the three images by pressing the "Load Data File" button, as long as the three images have the same file prefix. After that, a color map of the red laser image data will appear automatically in the main display axis.

7.2.2 The "Surface Boundary Identification" panel contains a variety of parameters to adjust for further improvement of the contrast, including Gamma, TopHat, Threshold, ConnTH, and SE Radius. "Gamma" means a nonlinear scaling parameter for intensity values within the scale of 0.25 to 1, and a Gamma smaller than 1 provides more contrast at lower intensities. "TopHat" represents the size of features for the system to ignore

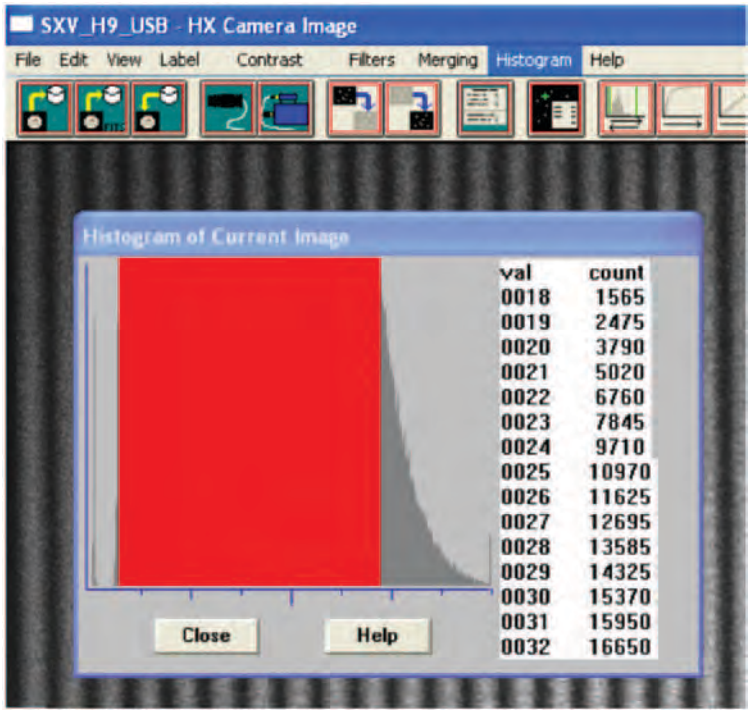

Figure D-2. Interface of histogram in SXV.

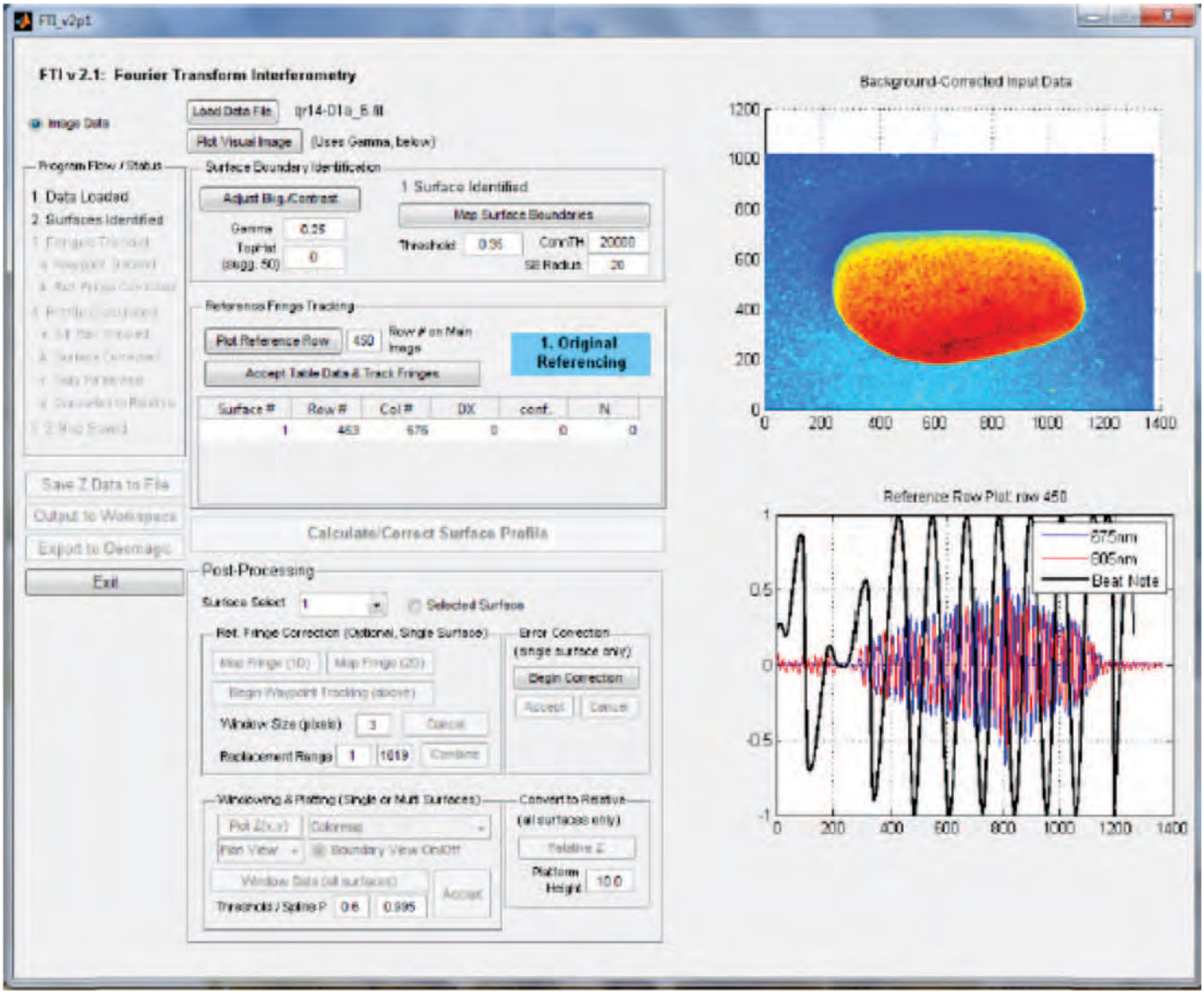

Figure D-3. The GUI of the FTI software.

and is used to remove small variations in background. Entering a value of 50 will force the program to ignore background variations smaller than 50 pixels in diameter. Lager values of TopHat take longer to process. "Threshold" is the fraction of maximum intensity value to draw the boundary, with a default value of 0.35. "ConnTH" is the minimum area of each surface to be identified, in units of pixels. "SE Radius" is the filtering/offset parameter. With appropriate values in the "Surface Boundary Identification" panel, the exact aggregate boundary can be identified in the image based on the contrast between the image surface and the black background by pressing the "Map Surface Boundaries" button.

7.2.3 In the "Reference Fringe Tracking" pane, select a single reference fringe for each surface identified in a table. The row number and column number listed in the table are initialized to the approximate center of each surface. Choose a row near the vertical center of the surface and enter it into the box labeled "Row #" on Main Image and then press the "Plot Reference Row" button. Choose a fringe peak that extends to the upper and lower extents of the image. As shown in Figure D-4, zoom in on the 675-nm curve in the lower axis to show the fringe pattern across the selected row in the main image. Be sure to include the closest neighboring 805-nm peak in the zoomed viewing area.

7.2.4 Press the "Acceptable Table" button and Track Fringes to calculate the exact x_0 and DX values for each surface/fringe. After that, check the values of DX,

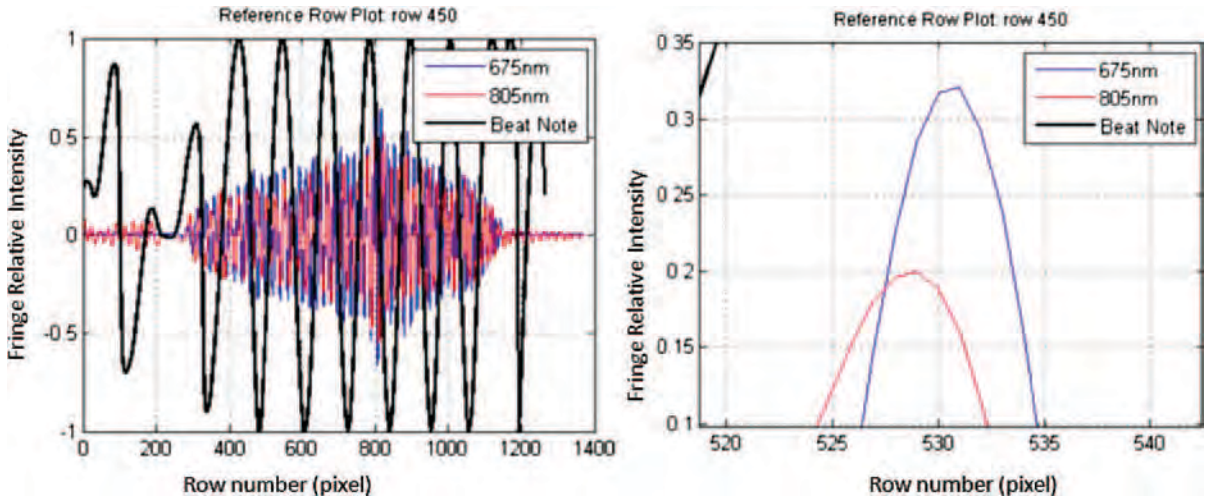

Figure D-4. Dual wave method for locating the zero-order reference fringe.

conf., and N calculated in the table representation in Figure D-5. If the program selected the wrong value of N, replace it with the correct one shown in Figure D-5.

7.2.5 Press the "Calculate/Correct Surface Profile" button.

7.2.6 Select the surface containing error areas by using the "Surface Select" drop-down menu to correct surface errors. Press the "Begin Correction" button in the "Error Correction" pane, then select an alternative reference fringe in the "Reference Fringe Tracking" panel, and repeat steps 7.2.3 and 7.2.4 for image correction. If the alternative reference does not look good, a new reference row can be chosen by repeating steps 7.2.3 and 7.2.4. If the correct profile is good, press the "Accept" button in the "Error Correction" pane to permanently replace/save the new profile data. Press the Cancel button in the "Ref. Fringe Correction" pane at any time if canceling the reference correction is desired. The program will revert to original fringe tracking.

7.2.7 Press the "Window Data (all surfaces)" button in the "Windowing & Plotting" pane using the default parameters for Threshold and Spline P. Increasing the value of Threshold to close to 1 will allow more error and result in a less restrictive boundary; increasing the value of Spline P to close to 1 will cause a curvy boundary over some point errors extending to the interior of the surface.

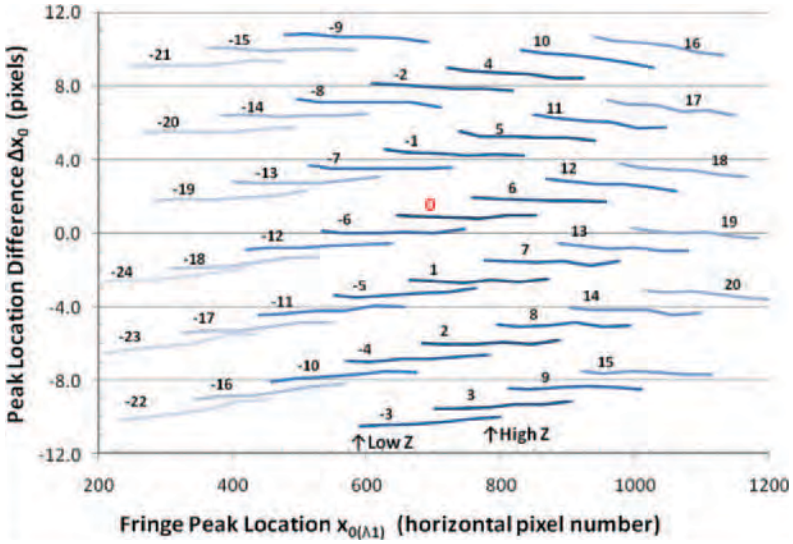

Figure D-5. Graphical representation of the fringe order (N) lookup table.

7.2.8 Enter the tray height as measured by micrometer in step 7.1.2. Press the "Relative Z" button to convert to relative surface height.

7.2.9 Use the "Surface Select" pull-down menu and "Selected Surface/All Surface" check box to control which surfaces are plotted. Prior to plotting, change the "Surface Map Type" (pull-down menu) and "Boundary on/off" (check box), then choose the desired combination of views and press the "Plot Z(x, y)" button. After plotting, use the "Plan View/Iso View" pull-down menu to switch between overhead and isometric views.

7.2.10 Press "Save Z Data to File" to save all the data in a .mat file for the analyzed aggregates.

Press "Output to Workspace" to output several surface mapping variables to MATLAB command space for further manipulation.

Press "Export to Geomagic" to save the surface profile as an ASCII text file for use with Geomagic software.

7.3 Morphological Analysis

7.3.1 Load .mat file saved in step 7.2.10 in MATLAB, and run the morphological analysis program.

7.3.2 Go to the sheet named "Result." The result table tabulates sphericity, flatness ratio, elongation ratio, angularity, and texture for coarse aggregate samples, and tabulate sphericity, flatness ratio, elongation ratio, and angularity for fine aggregate samples.

8. Calculation

8.1 Calculate the sphericity mean and standard deviation for each coarse aggregate fraction.

8.2 Calculate the gradient angularity mean and standard deviation for each aggregate fraction.

8.3 Calculate the gradient texture mean and standard deviation for each aggregate fraction.

8.4 Calculate the percentage distribution of flat and elongated at the following ratios:

≥1:1, >2:1, >3:1, >4:1

Percentage ($D_l/D_s \geq 1{:}1$) = Percentage of particles with $D_l/D_s \geq 1{:}1$

Percentage ($D_l/D_s \geq 2{:}1$) = Percentage of particles with $D_l/D_s \geq 2{:}1$

Percentage ($D_l/D_s \geq 3{:}1$) = Percentage of particles with $D_l/D_s \geq 3{:}1$

Percentage ($D_l/D_s \geq 4{:}1$) = Percentage of particles with $D_l/D_s \geq 4{:}1$

8.5 Calculate the percentage distribution of flat or elongated at the following ratios:

≥1:1, >2:1, >3:1, >4:1

Percentage (≥1:1) = Percentage of particles with D_l/D_s or $D_{lm}/D_s \geq 1{:}1$

Percentage ($D_l/D_s \geq 2{:}1$) = Percentage of particles with D_l/D_s or $D_{lm}/D_s \geq 2{:}1$

Percentage ($D_l/D_s \geq 3{:}1$) = Percentage of particles with D_l/D_s or $D_{lm}/D_s \geq 3{:}1$

Percentage ($D_l/D_s \geq 4{:}1$) = Percentage of particles with D_l/D_s or $D_{lm}/D_s \geq 4{:}1$

9. Report

9.1 Report the following information:

9.1.1 Project name

9.1.2 Data of the analysis

9.1.3 Material sample identification: type, source, size, gradation

9.1.4 Number of particles for each size

9.1.5 Mean and standard deviation of morphological characteristics of all the analyzed aggregates within one size range

10. Precision and Bias

10.1 *Precision*—This practice uses data generated from other testing methods to develop cumulative information; therefore, the precision of the values generated in this practice is established by the precision of the standards used to collect the raw data.

10.2 *Bias*—Since there is no accepted reference device suitable for determining the bias in this method, no statement of bias is made.

11. Keywords

11.1 Aggregate, shape, angularity, texture, Fourier Transform Interferometry system.

APPENDICES E–J

Appendices E through J are not published herein but are available at http://apps.trb.org/cmsfeed/TRBNetProjectDisplay.asp?ProjectID=867. The appendices titles are:

Appendix E: Photographs of Coarse Aggregates in Set 1
Appendix F: FTI Analysis Results
Appendix G: Histogram and Normal Quantile Plot of Aggregates in Set 1
Appendix H: Manual Measurements of Aggregates in Set 1
Appendix I: AIMS II Analysis Results
Appendix J: UIAIA Analysis Results

Abbreviations and acronyms used without definitions in TRB publications:

AAAE	American Association of Airport Executives
AASHO	American Association of State Highway Officials
AASHTO	American Association of State Highway and Transportation Officials
ACI–NA	Airports Council International–North America
ACRP	Airport Cooperative Research Program
ADA	Americans with Disabilities Act
APTA	American Public Transportation Association
ASCE	American Society of Civil Engineers
ASME	American Society of Mechanical Engineers
ASTM	American Society for Testing and Materials
ATA	American Trucking Associations
CTAA	Community Transportation Association of America
CTBSSP	Commercial Truck and Bus Safety Synthesis Program
DHS	Department of Homeland Security
DOE	Department of Energy
EPA	Environmental Protection Agency
FAA	Federal Aviation Administration
FHWA	Federal Highway Administration
FMCSA	Federal Motor Carrier Safety Administration
FRA	Federal Railroad Administration
FTA	Federal Transit Administration
HMCRP	Hazardous Materials Cooperative Research Program
IEEE	Institute of Electrical and Electronics Engineers
ISTEA	Intermodal Surface Transportation Efficiency Act of 1991
ITE	Institute of Transportation Engineers
NASA	National Aeronautics and Space Administration
NASAO	National Association of State Aviation Officials
NCFRP	National Cooperative Freight Research Program
NCHRP	National Cooperative Highway Research Program
NHTSA	National Highway Traffic Safety Administration
NTSB	National Transportation Safety Board
PHMSA	Pipeline and Hazardous Materials Safety Administration
RITA	Research and Innovative Technology Administration
SAE	Society of Automotive Engineers
SAFETEA-LU	Safe, Accountable, Flexible, Efficient Transportation Equity Act: A Legacy for Users (2005)
TCRP	Transit Cooperative Research Program
TEA-21	Transportation Equity Act for the 21st Century (1998)
TRB	Transportation Research Board
TSA	Transportation Security Administration
U.S.DOT	United States Department of Transportation